WP3 interim +final report: Electrochemical performance evaluation

Table of contents

1.1 Experimental Methodology for Electrochemical Characterization 3
1.2 Electrocatalytic Performance of Ni Coatings Electrodeposited from a DES-Based Electrolyte 5
1.2.1 Deposition temperature 40 ºC.....5
1.2.2 Deposition temperature 50 ºC.....13
1.2.3 Deposition temperature 60 ºC.....20
1.2.4 Deposition temperature 30 ºC.....28
1.2.5 Influence of Ni Electrodeposition Temperature on HER Kinetics.....35
1.2.6 Comparison of HER Performance with Literature Data and Benefits of DES-Assisted Ni Electrodeposition.....41
Comparison with conventional and aqueous-electrodeposited Ni 43
Evidence from DES-electrodeposited nanostructured Ni 44
Significance and advantages of DES-assisted Ni electrodeposition 46
Overall assessment and prospects of DES-derived Ni catalysts 47
1.3 Electrocatalytic HER Performance of Ni/MoS_2 Composite Coatings Electrodeposited from a DES-Based Electrolyte.....49
1.3.1 Series 1, deposition temperature 40 ºC.....50
1.3.2 Series 2, deposition temperature 40 ºC.....54
1.3.3 Series 3, deposition temperature 40 ºC.....59
1.3.4 Comparative Analysis of HER Performance of Ni/MoS_2 Composite Coatings 65
1.3.5 Effect of MoS_2 incorporation on HER performance 68
1.4 Electrochemical characterization of C-MoFeNiP materials synthesized at different pyrolysis temperatures 70
1.5 HER Electrocatalytic Performance of Ni/MXene Composite Coatings.....77
1.5.1 Electrodeposition temperature 40ºC.....79
1.5.2 Electrodeposition temperature 50ºC.....85

1.5.3 Electrodeposition temperature 60°C 91
1.5.4 Electrodeposition temperature 30°C 96
1.5.5 Influence of Electrodeposition Conditions on the HER Performance of Ni/MXene Composite Coatings 102
1.6 Electrochemical evaluation of $Ni_{1-x}Co_xS$ catalysts for HER 103
1.7 Comparative HER Performance of Bare and Modified Ni Foam Electrodes with Ni and Ni/MoS_2 Coatings 108

1.1 Experimental Methodology for Electrochemical Characterization

WP3 aimed to obtain comprehensive information on catalyst activity in alkaline media. For this purpose, a series of electrochemical measurements and subsequent calculations were performed. For each developed catalyst, open-circuit potential (OCP) measurements were conducted, followed by the recording of 7–8 linear sweep voltammetry (LSV) curves. The Tafel regions of the obtained polarization curves were analyzed, and the relevant parameters characterizing the electrocatalytic activity of each catalyst were calculated.

All electrochemical measurements were performed using specialized Gamry Potentiostats/Galvanostats Reference 3000 and 3020. Measurements were carried out in thermostated three-electrode electrochemical cells from Gamry. The developed catalysts were used as working electrodes, a saturated Ag/AgCl electrode served as the reference electrode, and a graphite rod with a high surface area was employed as the counter electrode. A 1 M NaOH solution was used as the electrolyte, providing a standard alkaline medium for evaluating the electrocatalytic performance of the developed materials.

The temperature was maintained at 25 °C using a thermostat throughout the measurements. Before each experiment, the electrolyte was deaerated by purging with an inert gas to remove dissolved oxygen. Automatic iR compensation was applied during the electrochemical measurements to minimize the influence of uncompensated resistance on the recorded electrochemical response.

The experimental setup and appearance of the electrochemical cell used for the measurements are shown in Fig. 1.

The materials subjected to electrochemical testing included Cu foils coated with Ni electrodeposited from a deep eutectic solvent (DES)-based electrolyte, as well as Ni/MoS_2 composite coatings deposited from DES-based electrolytes using both

commercially available MoS_2 powder and MoS_2 powder synthesized directly in DES. In addition, Ni/MXene composite coatings were investigated. To evaluate the influence of the substrate morphology and surface area on electrocatalytic performance, Ni foam samples modified with the same types of coatings were also tested.

Detailed information on the preparation and synthesis procedures of all investigated samples is provided in the WP1 report, while comprehensive morphological, structural, and chemical characterization of the developed catalysts is presented in the WP2 report.



Figure 1. Experimental three-electrode electrochemical cell setup used for the evaluation of electrocatalytic activity in 1 M NaOH.

1.2 Electrocatalytic Performance of Ni Coatings Electrodeposited from a DES-Based Electrolyte

1.2.1 Deposition temperature 40 ºC

The electrocatalytic behavior of Ni-coated Samples 2, 3, 4, and 5 (Table 1) was evaluated using the seventh-cycle polarization curves recorded in 1 M NaOH at 25 °C with a scan rate of 2 mV s^{-1} (Figures 2-5). Current densities were normalized to the geometric working-electrode area of 4 cm^2, while the measured potentials were converted from the saturated Ag/AgCl reference scale to the reversible hydrogen electrode (RHE) scale. Tafel analysis was performed by fitting the cathodic polarization data according to the relationship $\eta=a+b\cdot\log_{10}|j|$, where a is the Tafel intercept, b is the Tafel slope, and j is expressed in A cm^{-2}. To ensure a consistent comparison among all investigated electrodes, linear regressions were restricted to the common current-density interval of 1–5 mA cm^{-2}. Excellent linearity was obtained for all samples, with R^2 values between 0.99771 and 0.99799, confirming that the selected current-density interval is well described by a linear Tafel relationship.

Table 1. Electrodeposition conditions for Ni coatings prepared from the DES-based electrolyte.

Sample	Temperature during coating deposition, t / ºC	Deposition current density, j / mA/cm^2
2	40	5
3		10
4		15
5		20

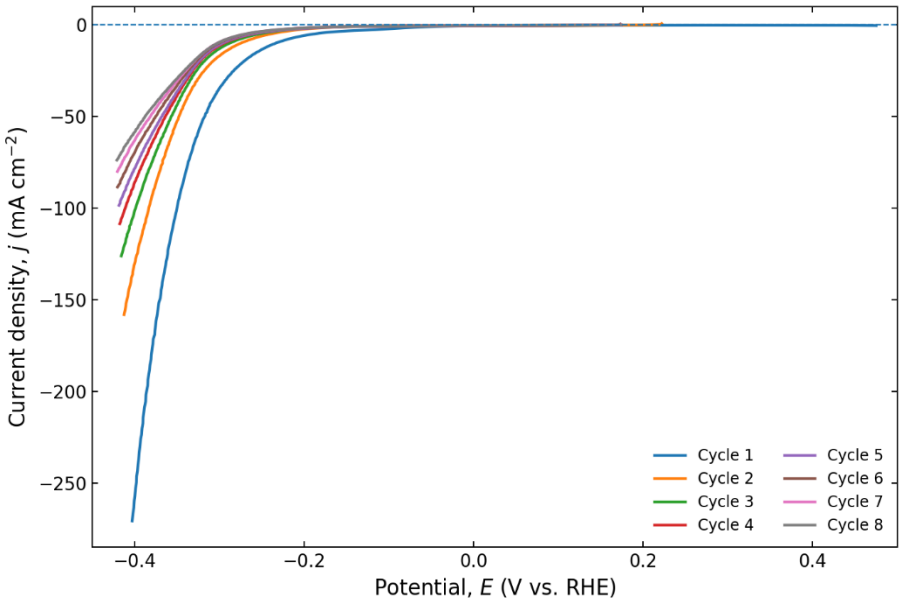


Figure 2. Linear sweep voltammograms of Sample 2 recorded during seven consecutive cycles in 1 M NaOH at 25 °C with a scan rate of 2 mV s^{-1}. Potentials are presented on the RHE scale, and currents are normalized to the geometric electrode area.

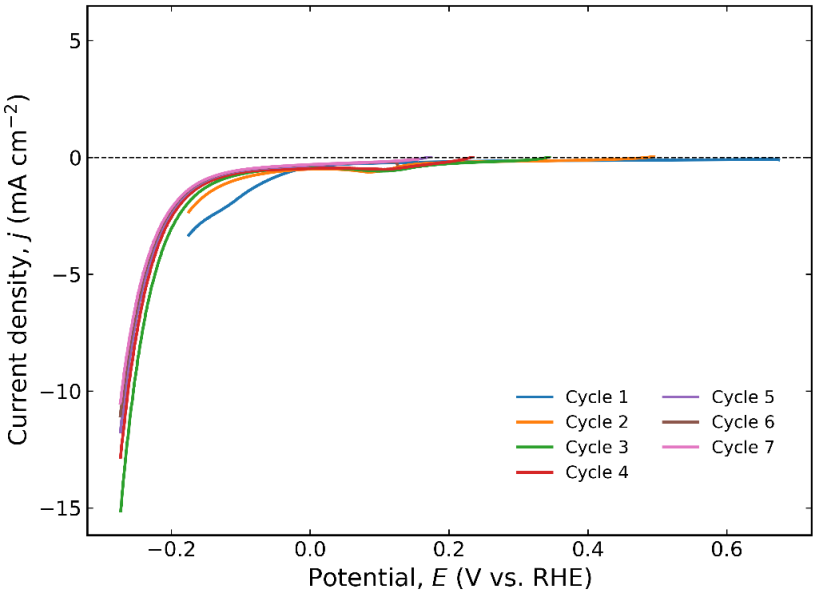


Figure 3. Linear sweep voltammograms of Sample 3 recorded during seven consecutive cycles in 1 M NaOH at 25 °C with a scan rate of 2 mV s^{-1}. Potentials are presented on the RHE scale, and currents are normalized to the geometric electrode area.

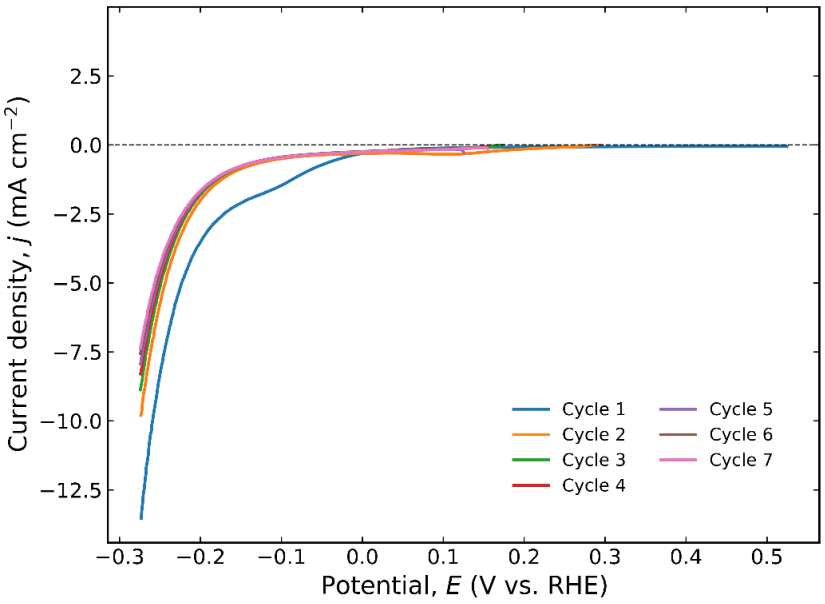


Figure 4. Linear sweep voltammograms of Sample 4 recorded during seven consecutive cycles in 1 M NaOH at 25 °C with a scan rate of 2 mV s^{-1}. Potentials are presented on the RHE scale, and currents are normalized to the geometric electrode area.

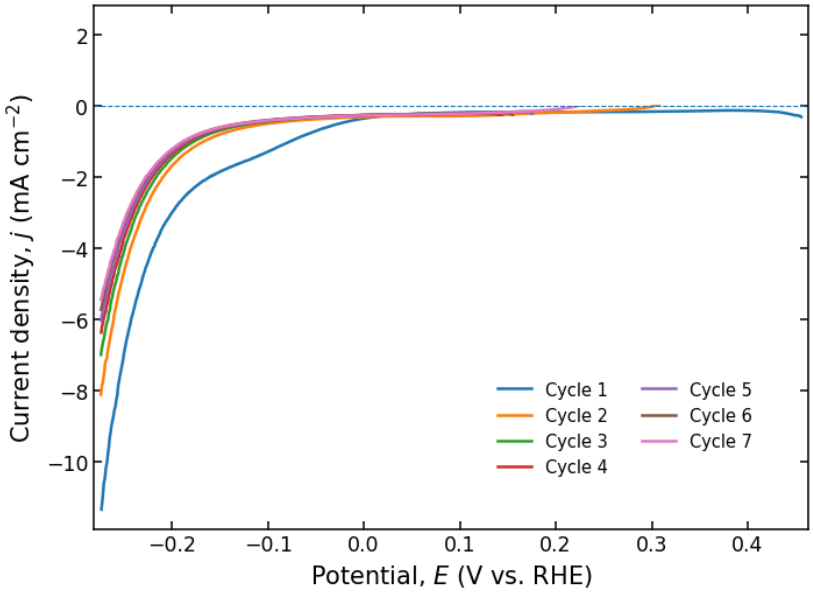


Figure 5. Linear sweep voltammograms of Ni-coated Sample 5 recorded during seven consecutive cycles in 1 M NaOH at 25 °C and a scan rate of 2 mV s^{-1}. Potentials were converted to the RHE scale, and currents were normalized to the geometric electrode area.

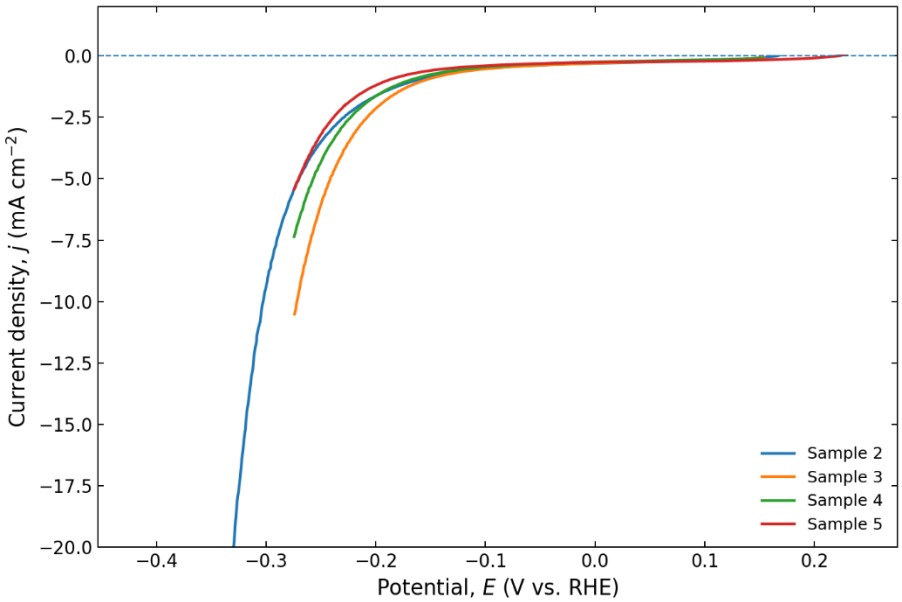


Figure 6. Linear sweep voltammograms corresponding to Cycle 7 for Ni-coated Samples 2, 3, 4, and 5 recorded in 1 M NaOH at 25 °C with a scan rate of 2 mV s^{-1}. Potentials are reported versus the reversible hydrogen electrode (RHE), and current densities are normalized to the geometric electrode area.

The resulting Tafel slopes show significant differences in the kinetic response of the Ni-coated electrodes (Figure 7, Table 2). Sample 5 exhibited the lowest absolute Tafel slope of 115.4 mV dec^{-1}, followed by Sample 3 at 121.6 mV dec^{-1}, Sample 4 at 124.7 mV dec^{-1}, and Sample 2 at 153.7 mV dec^{-1}. A smaller Tafel slope indicates that a smaller increase in overpotential is required to produce a tenfold increase in current density within the fitted region. On this basis, Sample 5 shows the most favorable current-density response to increasing polarization, whereas Sample 2 displays the least favorable slope. However, the Tafel slope alone should not be used to rank the overall catalytic activity because it describes the rate at which current changes with polarization rather than the absolute overpotential required to achieve a particular current density. This distinction is particularly important for Sample 5, which has the smallest Tafel slope but does not exhibit the lowest operating overpotentials.

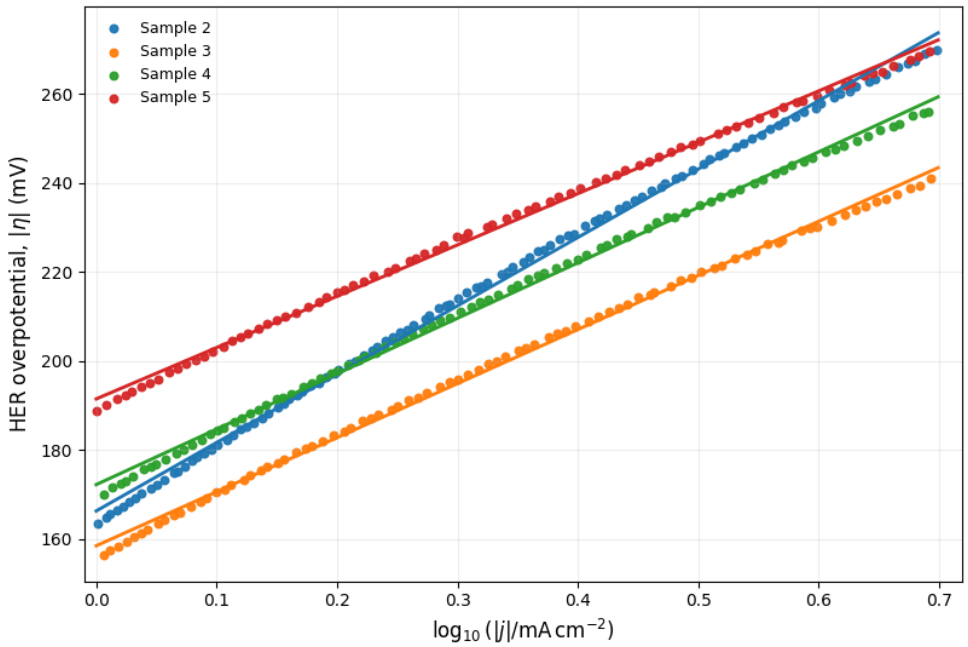


Figure 7. Tafel plots derived from the seventh-cycle polarization curves of Ni-coated Samples 2, 3, 4, and 5 recorded in 1 M NaOH at 25 °C. Current densities were normalized to the geometric electrode area of 4 cm², and potentials were converted from saturated Ag/AgCl to the RHE scale. Solid lines represent linear regressions.

Table 2. HER kinetic parameters determined from Cycle 7 polarization curves in 1 M NaOH at 25 °C.

Sample	Tafel intercept, a (V)	|b| (mV dec⁻¹)	R^2	Apparent j_0 (A cm⁻²)	95% CI for j_0 (mA cm⁻²)	η_1 (mV)	η_5 (mV)	η_{10} (mV)	η_{10} determination
2	0.1663	153.7	0.99771	8.387×10^{-5}	0.0814–0.0864	162.3	269.1	302.0	Interpolated from measured polarization curve
3	0.1585	121.6	0.99799	5.051×10^{-5}	0.0487–0.0524	154.7	240.6	271.1	Interpolated from measured polarization curve
4	0.1722	124.7	0.99791	4.219×10^{-5}	0.0406–0.0439	168.4	256.2	296.1	Tafel extrapolation from 1–5 mA cm⁻² fit
5	0.1915	115.4	0.99789	2.228×10^{-5}	0.0213–0.0233	188.0	269.5	306.1	Tafel extrapolation from 1–5 mA cm⁻² fit

The experimentally determined overpotentials provide a more direct comparison of the practical catalytic performance. At a current density of 1 mA cm^{-2}, Sample 3 required the lowest overpotential, 154.7 mV, followed by Sample 2 at 162.3 mV, Sample 4 at 168.4 mV, and Sample 5 at 188.0 mV. Sample 3 therefore shows the most favorable low-current catalytic behavior. The difference becomes more pronounced at 5 mA cm^{-2}, where Sample 3 requires only 240.6 mV, compared with 256.2 mV for Sample 4, 269.1 mV for Sample 2, and 269.5 mV for Sample 5. Thus, at 5 mA cm^{-2}, Sample 3 reduces the required overpotential by 15.6 mV relative to Sample 4, 28.5 mV relative to Sample 2, and 28.9 mV relative to Sample 5. Because 1–5 mA cm^{-2} represents the common experimental interval used for the Tafel analysis, these differences provide strong evidence for the superior catalytic performance of Sample 3 within the directly comparable current-density range.

The behavior at 10 mA cm^{-2} further differentiates the samples. Samples 2 and 3 experimentally reached this current density, giving η_{10} values of 302.0 and 271.1 mV, respectively. Sample 3 therefore requires approximately 30.9 mV less overpotential than Sample 2 to achieve 10 mA cm^{-2}. In contrast, Samples 4 and 5 did not experimentally reach 10 mA cm^{-2} within their recorded polarization curves. Their η_{10} values of 296.1 and 306.1 mV, respectively, were consequently estimated by extrapolating the Tafel regressions obtained over 1–5 mA cm^{-2}. These extrapolated values are useful for comparative purposes but should be interpreted with greater caution than the experimentally supported η_{10} values of Samples 2 and 3. In particular, the apparently favorable η_{10} predicted for Sample 4 should not be considered equivalent to an experimentally demonstrated current density of 10 mA cm^{-2}.

The apparent exchange current densities calculated from the Tafel regressions were $8.387 \cdot 10^{-5}$, $5.051 \cdot 10^{-5}$, $4.219 \cdot 10^{-5}$, and $2.228 \cdot 10^{-5}$ A cm^{-2} for Samples 2, 3, 4, and 5, respectively. Sample 2 therefore exhibits the largest apparent j_0, followed by

Samples 3, 4, and 5. The corresponding 95% confidence intervals were 0.0814–0.0864, 0.0487–0.0524, 0.0406–0.0439, and 0.0213–0.0233 mA cm^{-2}, respectively. The relatively narrow and non-overlapping confidence intervals indicate that the regression-derived differences in apparent j_0 are well resolved. Nevertheless, these quantities should specifically be described as apparent exchange current densities because they are obtained by extrapolating Tafel relationships fitted at 1–5 mA cm^{-2} toward zero overpotential. Consequently, they depend strongly on both the fitted slope and intercept and should not be considered more representative of practical catalytic performance than directly measured overpotentials. This consideration explains why Sample 2 exhibits the largest apparent j_0 despite Sample 3 showing substantially lower overpotentials at higher experimentally relevant current densities.

Sample 2 demonstrates relatively favorable activity at low current density, with η_1 = 162.3 mV, and possesses the largest apparent exchange current density. However, its Tafel slope of 153.7 mV dec^{-1} is substantially larger than those of the other electrodes. Consequently, the overpotential required by Sample 2 increases relatively rapidly as the current density rises. The difference between Samples 2 and 3 is only 7.6 mV at 1 mA cm^{-2} but increases to 28.5 mV at 5 mA cm^{-2} and 30.9 mV at 10 mA cm^{-2}. This behavior indicates that Sample 2 is competitive at relatively low current density but becomes less favorable as the hydrogen-evolution rate increases.

Sample 4 exhibits intermediate performance, combining a relatively low Tafel slope of 124.7 mV dec^{-1} with η_1 and η_5 values of 168.4 and 256.2 mV, respectively. Its kinetic response is therefore close to that of Sample 3 in terms of Tafel slope, although Sample 3 maintains consistently lower overpotentials. At 5 mA cm^{-2}, Sample 4 requires 15.6 mV more overpotential than Sample 3. The inability of Sample 4 to experimentally reach 10 mA cm^{-2} under the investigated polarization

conditions further distinguishes it from Sample 3, despite the relatively favorable extrapolated η_{10} value.

Sample 5 presents an interesting contrast between Tafel slope and absolute catalytic performance. Although it exhibits the lowest Tafel slope of 115.4 mV dec^{-1}, it requires the highest overpotential at 1 mA cm^{-2}, 188.0 mV, and an overpotential of 269.5 mV at 5 mA cm^{-2}. It also possesses the lowest apparent exchange current density. Therefore, its small Tafel slope should be interpreted as a favorable increase in current with additional polarization rather than evidence that it is the most active electrode overall. The polarization curve remains shifted toward larger overpotentials compared with Sample 3 throughout the common experimental range.

Considering the complete electrochemical dataset, Sample 3 exhibits the most favorable overall catalytic performance among the investigated Ni-coated electrodes. It combines the lowest experimentally measured overpotential at both 1 mA cm^{-2} (154.7 mV) and 5 mA cm^{-2} (240.6 mV), an experimentally established η_{10} of only 271.1 mV, a relatively low Tafel slope of 121.6 mV dec^{-1}, and the highest regression coefficient (R^2 = 0.99799). Particularly significant is its ability to maintain its advantage as current density increases. Sample 3 requires approximately 28–29 mV less overpotential than Samples 2 and 5 at 5 mA cm^{-2} and approximately 31 mV less than Sample 2 at 10 mA cm^{-2}. These differences indicate that its favorable activity is maintained rather than being restricted to the low-current region.

Overall, based primarily on the directly measured overpotentials within the common experimental current-density range, the catalytic activity can be described approximately as Sample 3 > Sample 4 > Sample 2 ≈ Sample 5, although the relative positions of Samples 2, 4, and 5 depend on the specific kinetic descriptor considered. Sample 2 is favored when apparent j_0 is considered, Sample 5 exhibits the lowest Tafel slope, and Sample 4 provides relatively favorable intermediate-current performance. In contrast, Sample 3 provides the most balanced combination of low

operating overpotential, favorable Tafel kinetics, high regression quality, and experimentally demonstrated achievement of 10 mA cm^{-2}. It can therefore be identified as the best-performing HER catalyst among the investigated Ni-coated samples under the applied experimental conditions. Further evaluation through long-term stability measurements, electrochemical impedance spectroscopy, and normalization to electrochemically active surface area would be valuable for determining whether its superior geometric-current activity arises predominantly from enhanced intrinsic catalytic kinetics, a greater accessible active surface area, or a combination of these effects.

1.2.2 Deposition temperature 50 ºC

The influence of the electrodeposition current density on the electrocatalytic behavior of the Ni coatings was investigated for samples prepared at a constant deposition temperature of 50 °C. The electrodeposition conditions are summarized in Table 3.

Table 3. Electrodeposition conditions for Ni coatings prepared from the DES-based electrolyte.

Sample	Temperature during coating deposition, t / ºC	Deposition current density, j / mA/cm^2
9_2	50	10
10_2		15
11_2		20

The electrocatalytic behavior of the resulting Ni-coated electrodes toward the hydrogen evolution reaction (HER) was evaluated by linear sweep voltammetry (LSV) in 1 M NaOH at 25 °C. Seven consecutive polarization cycles were recorded for each sample at a scan rate of 2 mV s^{-1}. The corresponding polarization curves

are presented in Figures 8–10. Potentials were converted from the saturated Ag/AgCl reference-electrode scale to the reversible hydrogen electrode (RHE) scale, while measured currents were normalized to the geometric electrode area of 4 cm^2.

A distinct difference between the first polarization cycle and the subsequent cycles was observed for the investigated electrodes. The evolution of the polarization response during repeated cycling indicates that the initially air-exposed Ni coating undergoes electrochemical conditioning upon immersion and polarization in the alkaline electrolyte. The particularly pronounced change during the first cycle may be associated with reduction and/or restructuring of the native surface oxide/hydroxide layer, removal of weakly bound surface species, improved wetting of the coating, and establishment of a more stable electrochemically active surface. The comparatively smaller changes during the subsequent cycles indicate progressive stabilization of the electrode/electrolyte interface. Because the present electrochemical measurements do not independently identify the surface species responsible for this behavior, attribution of the first-cycle change exclusively to oxide reduction should be treated as a plausible interpretation rather than a definitive mechanism.

To provide a quantitative comparison of the HER performance after electrochemical conditioning, the seventh polarization cycle was selected for further analysis. Tafel plots derived from these curves are shown in Figure 11, and the resulting kinetic parameters are summarized in Table 4.

The electrochemical results reveal a systematic effect of the electrodeposition current density on the HER response of the Ni coatings. Among the three electrodes, Sample 9_2, deposited at the lowest current density of 10 mA cm^{-2}, exhibited the lowest overpotentials at the investigated geometric current densities.

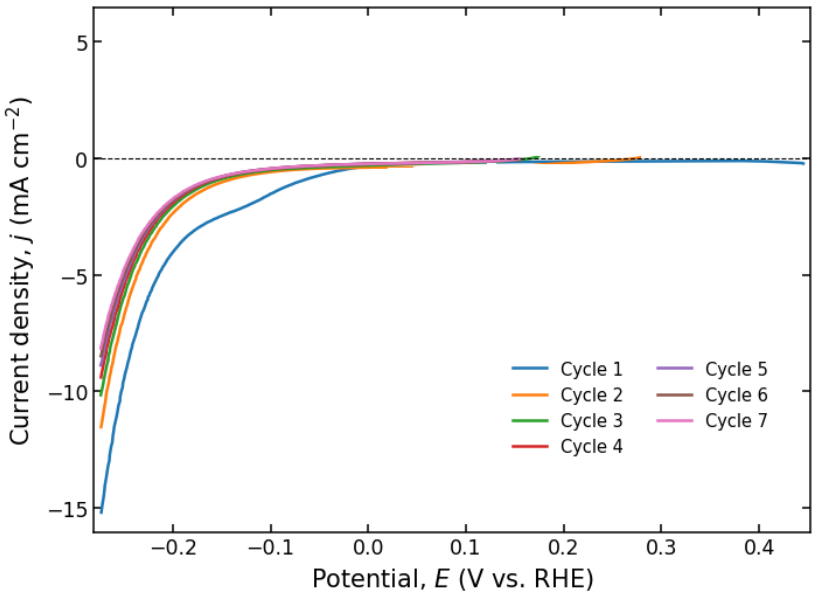


Figure 8. Linear sweep voltammograms of Ni-coated Sample 9_2 recorded during seven consecutive cycles in 1 M NaOH at 25 °C and a scan rate of 2 mV s^{-1}. Potentials were converted to the RHE scale, and currents were normalized to the geometric electrode area.

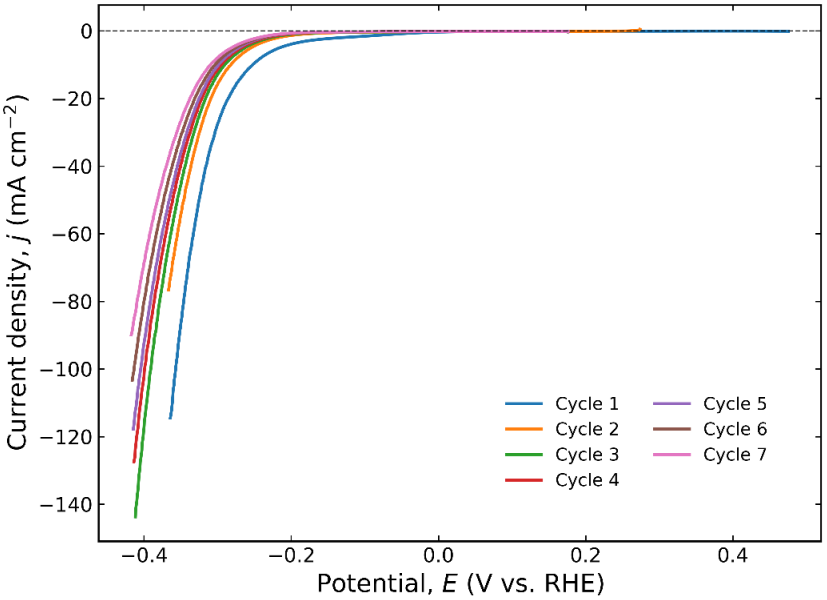


Figure 9. Linear sweep voltammograms of Sample 10_2 recorded during seven consecutive cycles in 1 M NaOH at 25 °C with a scan rate of 2 mV s^{-1}. Potentials are reported versus the reversible hydrogen electrode (RHE), and current densities are normalized to the geometric electrode area.

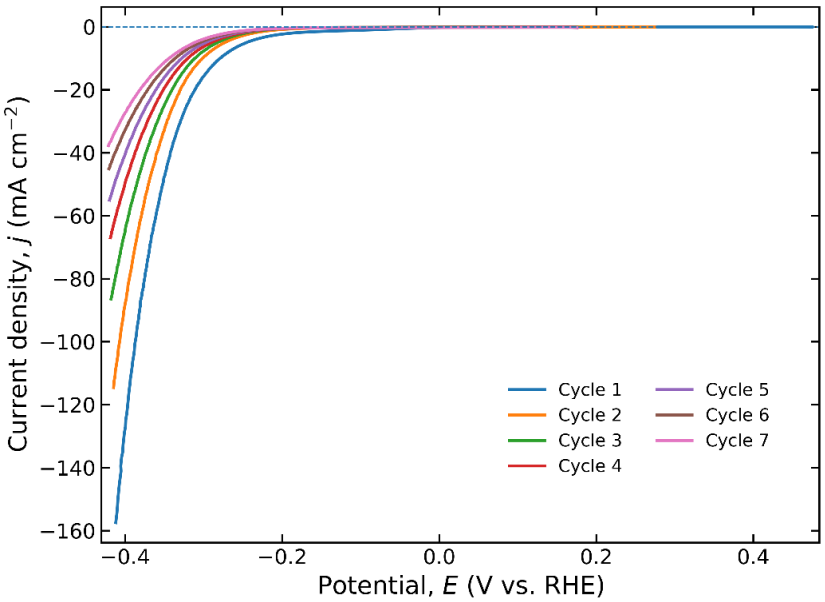


Figure 10. Linear sweep voltammograms of Ni-coated Sample 11_2 recorded during seven consecutive cycles in 1 M NaOH at 25 °C and a scan rate of 2 mV s^{-1}. Potentials are reported versus RHE, and currents are normalized to the geometric electrode area.

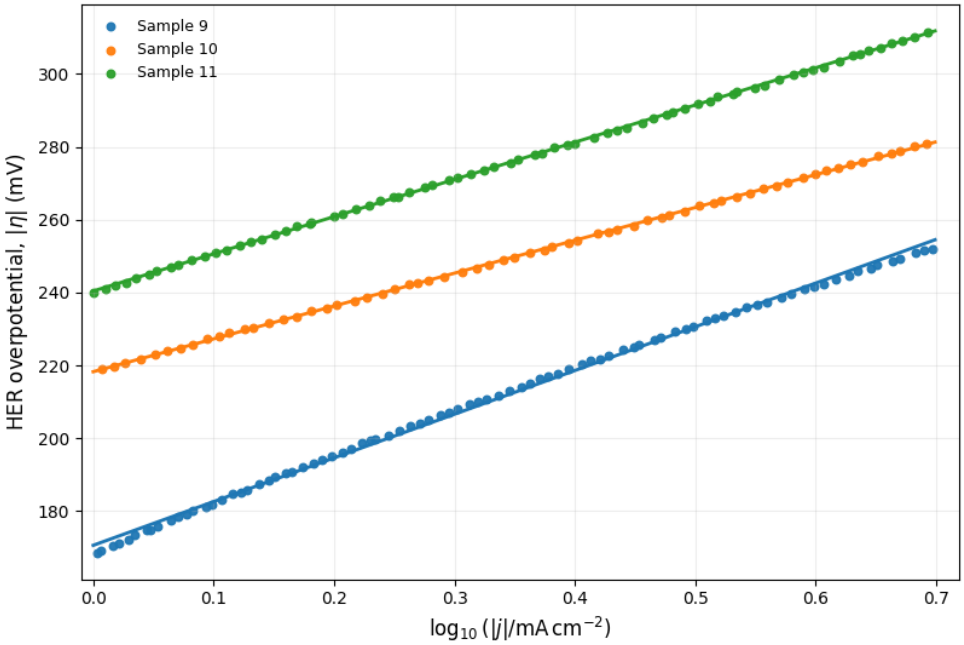


Figure 11. Tafel plots derived from the seventh-cycle polarization curves of Ni-coated Samples 9, 10, and 11 recorded in 1 M NaOH at 25 °C. Current densities were normalized to the geometric electrode area of 4 cm^2, and potentials were converted from saturated Ag/AgCl to the RHE scale. Solid lines represent linear regressions.

Table 4. HER kinetic parameters determined from Cycle 7 polarization curves in 1 M NaOH at 25 °C.

Sample	Tafel intercept, a (V)	Tafel slope, |b| (mV dec^{-1})	R^2	Apparent j_0 (A cm^{-2})	95% CI for j_0 (mA cm^{-2})	η_1 (mV)	η_5 (mV)	η_{10} (mV)	η_{10} determination
9_2	0.1706	123.94	0.99402	4.54×10^{-5}	0.0432–0.0477	166.4	253.0	290.4	Tafel extrapolation
10_2	0.2183	92.25	0.99988	4.46×10^{-6}	0.00441–0.00452	216.8	281.3	309.1	Tafel interpolation
11_2	0.2404	104.66	0.99968	5.26×10^{-6}	0.00516–0.00536	238.6	311.7	343.2	Tafel interpolation

The overpotential required to reach 1 mA cm^{-2} was 166.4 mV for Sample 9_2, compared with 216.8 mV for Sample 10_2 and 238.6 mV for Sample 11_2. Thus, increasing the deposition current density from 10 to 15 and 20 mA cm^{-2} increased η_1 by approximately 50 and 72 mV, respectively.

The same ordering was maintained at 5 mA cm^{-2}. Sample 9_2 required an overpotential of 253.0 mV, whereas Samples 10_2 and 11_2 required 281.3 and 311.7 mV, respectively. Consequently, Sample 9_2 required approximately 28 mV less overpotential than Sample 10_2 and approximately 59 mV less than Sample 11_2 to sustain the same geometric current density of 5 mA cm^{-2}. These results demonstrate that, within the investigated deposition conditions, the coating produced at 10 mA cm^{-2} provided the most favorable HER polarization response.

At 10 mA cm^{-2}, the same performance sequence was obtained: **9_2 > 10_2 > 11_2** in terms of HER activity, where higher activity corresponds to a lower required overpotential. The η_{10} values were 290.4, 309.1, and 343.2 mV for Samples 9_2, 10_2, and 11_2, respectively. Sample 9_2 therefore showed an approximately 19 mV lower η_{10} than Sample 10_2 and an approximately 53 mV lower value than Sample 11_2. It should be noted, however, that η_{10} for Sample 9_2 was obtained by extrapolation of its Tafel regression because the experimentally recorded seventh-cycle polarization curve did not extend to a geometric current density of 10 mA cm^{-2}. In contrast, the η_{10} values of Samples 10_2 and 11_2 could be obtained by

interpolation within their measured polarization data. The η_{10} value for Sample 9_2 therefore carries greater model dependence and should be interpreted with greater caution when comparing the three electrodes at 10 mA cm^{-2}.

The Tafel slopes provide additional information concerning the HER kinetics. Sample 10_2 exhibited the smallest absolute Tafel slope, 92.25 mV dec^{-1}, followed by Sample 11_2 at 104.66 mV dec^{-1} and Sample 9_2 at 123.94 mV dec^{-1}. A smaller Tafel slope indicates that a smaller additional overpotential is required to produce a tenfold increase in current density within the fitted region. Therefore, although Sample 9_2 displayed the lowest absolute overpotentials over the experimentally relevant current-density range, Sample 10_2 exhibited the smallest Tafel slope. This distinction is important: the lowest Tafel slope does not necessarily correspond to the electrode having the lowest overpotential at a specified current density because the position of the Tafel line, represented by its intercept, also influences the measured polarization performance.

The quality of the linear regressions was high, particularly for Samples 10_2 and 11_2, with R^2 values of 0.99988 and 0.99968, respectively. Sample 9_2 gave a slightly lower R^2 of 0.99402, although this value still indicates a strong linear relationship within the selected Tafel region. The very high coefficients of determination for Samples 10_2 and 11_2 indicate that their seventh-cycle polarization data closely followed the assumed logarithmic Tafel relationship over the regression interval.

The apparent exchange current density showed a different trend from the Tafel slope. Sample 9_2 exhibited the highest apparent j_0 – $4.54 \cdot 10^{-5}$ A cm^{-2}, approximately one order of magnitude higher than the values determined for Samples 10_2 ($4.46 \cdot 10^{-6}$ A cm^{-2}) and 11_2 ($5.26 \cdot 10^{-6}$ A cm^{-2}). The corresponding 95% confidence intervals were 0.0432–0.0477 mA cm^{-2} for Sample 9_2, 0.00441–0.00452 mA cm^{-2} for Sample 10_2, and 0.00516–0.00536 mA cm^{-2} for Sample

11_2. The confidence intervals do not overlap, indicating that the differences in the fitted apparent j_0 values are substantially larger than their regression-derived statistical uncertainties. Nevertheless, because j_0 is obtained by extrapolation of the Tafel regression and the currents are normalized to geometric rather than electrochemically active surface area, these values should primarily be used for comparative evaluation of the present electrodes under identical experimental and fitting conditions.

Taken together, the polarization and Tafel analyses demonstrate that changing the electrodeposition current density at a constant bath temperature of 50 °C substantially affected the subsequent HER behavior of the Ni coatings. The coating deposited at 10 mA cm^{-2} (Sample 9_2) showed the lowest η_1 and η_5 values and the highest apparent exchange current density, whereas increasing the deposition current density to 15 and particularly 20 mA cm^{-2} resulted in progressively higher HER overpotentials. Sample 10_2 nevertheless exhibited the smallest Tafel slope, suggesting a more favorable increase in current with increasing overpotential within the fitted Tafel region.

The electrochemical data therefore indicate that, among the three deposition conditions investigated at 50 °C, **10 mA cm^{-2} produced the Ni coating with the most favorable overall HER polarization performance**, while deposition at 20 mA cm^{-2} produced the least favorable response. The origin of this dependence cannot be established from the polarization measurements alone. Variations in deposition current density can modify coating morphology, roughness, porosity, grain structure, thickness, surface composition, and consequently the electrochemically active surface area. Correlation with complementary surface and structural characterization would therefore be required to determine which coating characteristics are responsible for the observed differences in HER performance.

1.2.3 Deposition temperature 60 ºC

The influence of electrodeposition current density on the electrocatalytic performance of Ni coatings deposited at 60 °C was investigated using Samples 12_2, 13_2, 14_2, and 15_2 (Table 5). The coatings were prepared at deposition current densities of 5, 10, 15, and 20 mA cm^{-2}, respectively. This series therefore enables the effect of deposition current density to be evaluated while maintaining a constant deposition temperature of 60 °C

Table 5. Electrodeposition conditions for Ni coatings prepared from the DES-based electrolyte.

Sample	Temperature during coating deposition, t / ºC	Deposition current density, j / mA/cm^2
12_2	50	5
13_2		10
14_2		15
15_2		20

The electrocatalytic behavior of the resulting Ni-coated electrodes toward the hydrogen evolution reaction (HER) was evaluated by linear sweep voltammetry in 1 M NaOH at 25 °C. Eight consecutive polarization cycles were recorded for each electrode at a scan rate of 2 mV s^{-1}. The corresponding LSV curves are presented in Figures 12–15. Potentials are reported relative to the reversible hydrogen electrode (RHE), and measured currents were normalized to the geometric working-electrode area of 4 cm^2.

As observed for the Ni coatings deposited at lower temperatures, changes in the polarization response occurred during consecutive cycling. Such evolution of the

LSV curves is consistent with electrochemical conditioning of the Ni surface during repeated cathodic polarization. Possible contributions include reduction and restructuring of the initially formed surface oxide/hydroxide species, removal of weakly adsorbed surface contaminants, changes in electrode wetting, and progressive establishment of a stable electrode/electrolyte interface. These processes may alter the number and accessibility of HER-active sites during the initial polarization cycles. Because the LSV measurements alone do not provide direct information on surface composition, however, the specific physicochemical origin of the observed conditioning cannot be conclusively identified from these measurements.

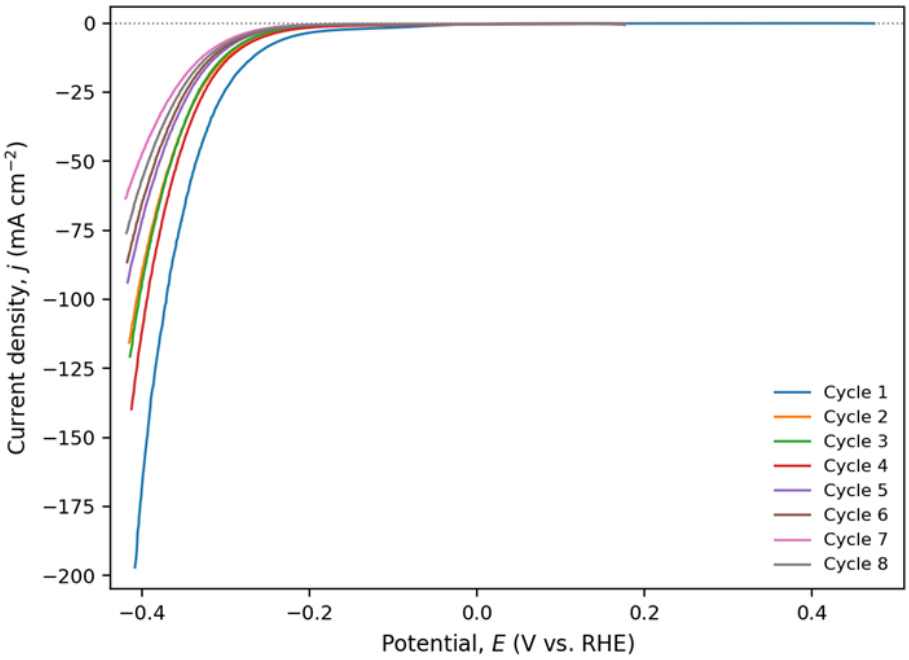


Figure 12. Linear sweep voltammograms of Ni-coated Sample 12_2 recorded during eight consecutive cycles in 1 M NaOH at 25 °C with a scan rate of 2 mV s^{-1}. Potentials are reported versus RHE, and currents are normalized to the geometric electrode area.

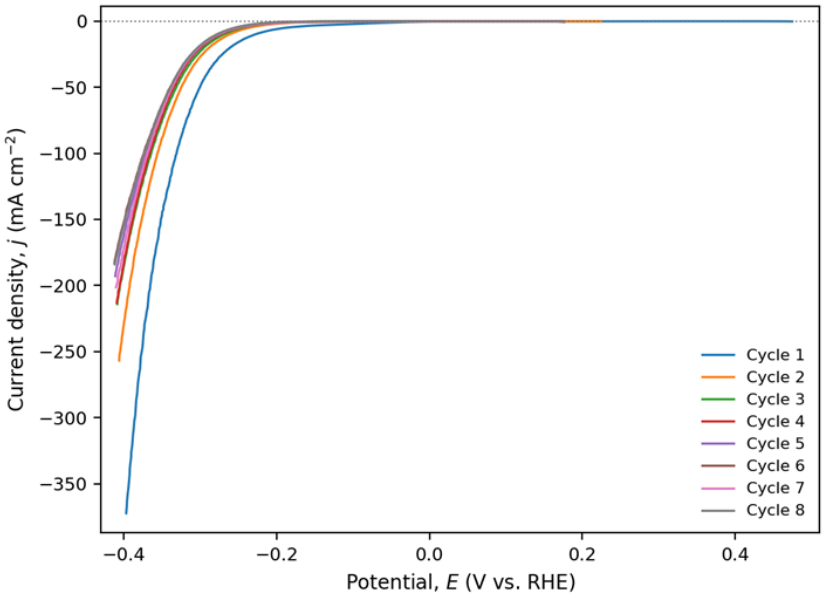


Figure 13. Linear sweep voltammograms of Ni-coated Sample 13_2 recorded during eight consecutive cycles in 1 M NaOH at 25 °C with a scan rate of 2 mV s^{-1}. Potentials are reported versus RHE, and currents are normalized to the geometric electrode area.

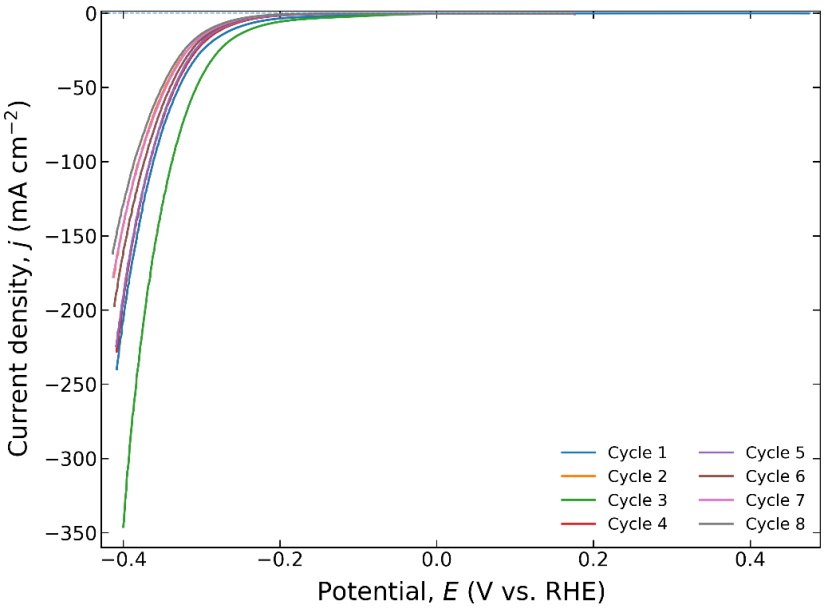


Figure 14. Linear sweep voltammograms of Ni-coated Sample 14_2 recorded during eight consecutive cycles in 1 M NaOH at 25 °C with a scan rate of 2 mV s^{-1}. Potentials are reported versus RHE, and currents are normalized to the geometric electrode area.

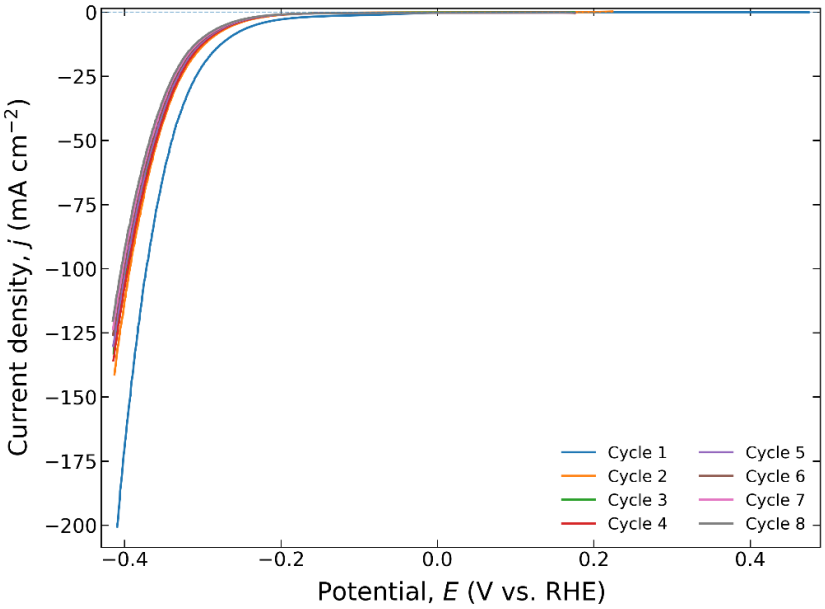


Figure 15. Linear sweep voltammograms of Ni-coated Sample 15_2 recorded during eight consecutive cycles in 1 M NaOH at 25 °C with a scan rate of 2 mV s^{-1}. The geometric working-electrode area was 4 cm^2. Potentials are reported versus RHE, and currents are normalized to the geometric electrode area.

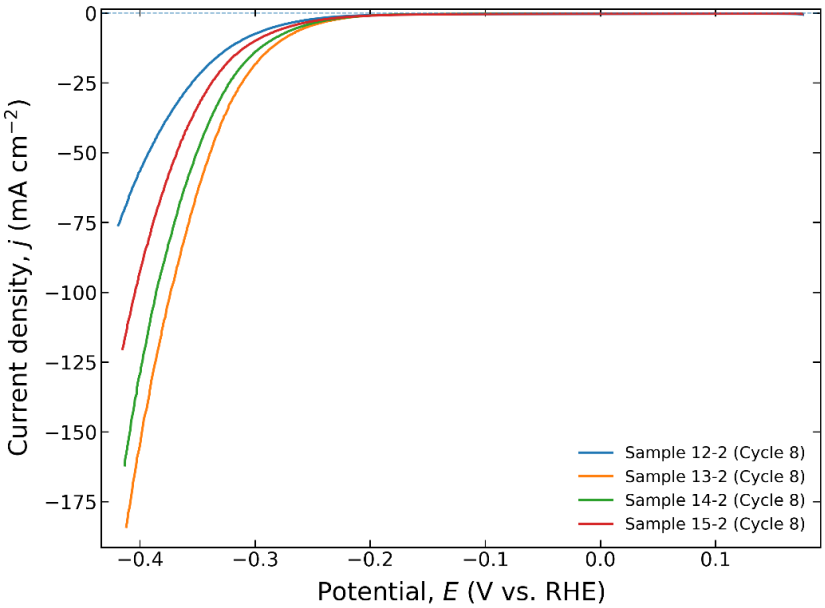


Figure 16. Linear sweep voltammograms corresponding to Cycle 8 for Ni-coated Samples 12_2, 13_2, 14_2 and 15_2 recorded in 1 M NaOH at 25 °C with a scan rate of 2 mV s^{-1}. Potentials are reported versus the reversible hydrogen electrode (RHE), and current densities are normalized to the geometric electrode area. Temperature of electrodeposition of Ni is 60ºC).

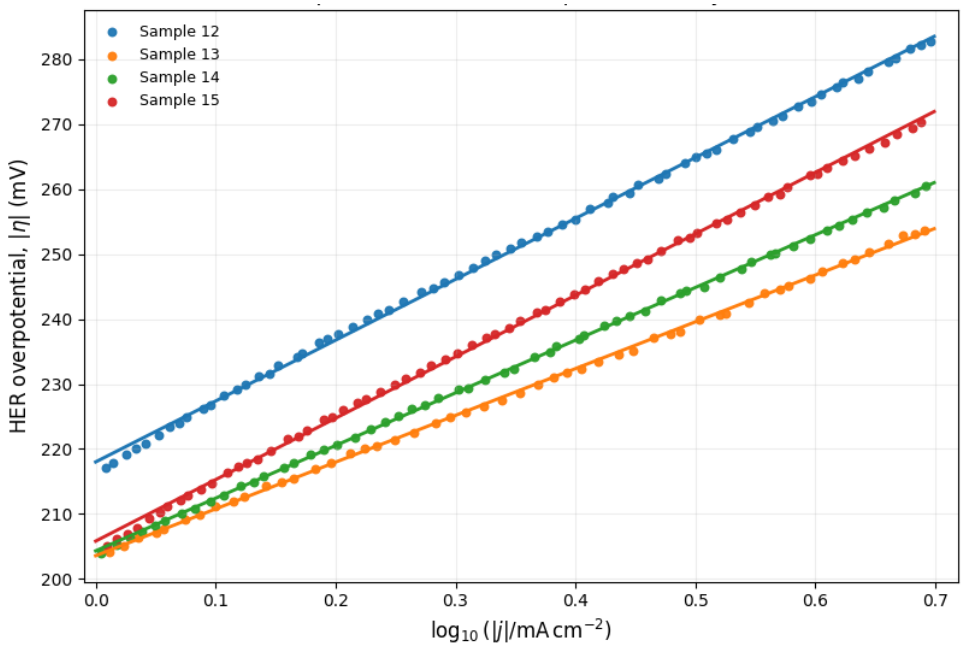


Figure 17. Tafel plots derived from the eighth-cycle polarization curves of Ni-coated Samples 12_2, 13_2, 14_2, and 15_2 recorded in 1 M NaOH at 25 °C. Current densities were normalized to the geometric electrode area of 4 cm², and potentials were converted from saturated Ag/AgCl to the RHE scale. Solid lines represent linear regressions over the current-density interval of 1–5 mA cm^{-2}.

Table 6. HER kinetic and performance parameters determined from the eighth-cycle polarization curves of Ni coatings electrodeposited at 60 °C.

Sample	Tafel intercept, a (V)	Tafel slope, $\|b\|$ (mV dec^{-1})	R^2	Apparent j_0 (A cm^{-2})	95% CI for j_0 (mA cm^{-2})	η_1 (mV)	η_5 (mV)	η_{10} (mV)	η_{10} determination
12_2	0.2180	93.8	0.9992	4.73×10^{-6}	0.00453–0.00494	216	283	**312**	Direct interpolation
13_2	0.2036	72.0	0.9996	1.49×10^{-6}	0.00143–0.00156	203	254	**278**	Direct interpolation
14_2	0.2043	81.1	0.9998	3.03×10^{-6}	0.00296–0.00311	204	261	**287**	Direct interpolation
15_2	0.2058	94.6	0.9993	6.69×10^{-6}	0.00644–0.00695	204	271	**300**	Direct interpolation

The eighth-cycle polarization data demonstrate that the electrodeposition current density affected the subsequent HER performance of the Ni coatings (Figure 16). At a geometric current density of 1 mA cm^{-2}, Sample 13_2 required an overpotential of 203 mV. Samples 14_2 and 15_2 showed essentially comparable low-current

performance, each requiring approximately 204 mV, whereas Sample 12_2 exhibited the highest η_1 value of 216 mV. The differences among Samples 13_2–15_2 are therefore very small at this relatively low HER current density, while the coating deposited at 5 mA cm^{-2} is clearly less favorable.

More pronounced differences emerge as the HER current density increases. At 5 mA cm^{-2}, Sample 13_2 exhibited the lowest overpotential of 254 mV, followed by Sample 14_2 at 261 mV, Sample 15_2 at 271 mV, and Sample 12_2 at 283 mV. Sample 13_2 therefore required 7 mV less overpotential than Sample 14_2, 17 mV less than Sample 15_2, and 29 mV less than Sample 12_2. The increasing separation of the polarization responses with increasing current density indicates that the advantages of Sample 13_2 become more apparent as the HER rate increases.

The same activity sequence is evident at 10 mA cm^{-2}. Sample 13_2 required the lowest η_{10} of 278 mV, while values of 287, 300, and 312 mV were obtained for Samples 14_2, 15_2, and 12_2, respectively. Consequently, Sample 13_2 reduced the overpotential required to reach 10 mA cm^{-2} by approximately 9 mV relative to Sample 14_2, 22 mV relative to Sample 15_2, and 34 mV relative to Sample 12_2. Importantly, all four η_{10} values were obtained by direct interpolation within the experimentally measured polarization range. The comparison at 10 mA cm^{-2} is therefore experimentally supported for every electrode and does not rely on extrapolation of the fitted Tafel relationship.

The Tafel analysis provides further evidence for the favorable behavior of Sample 13_2. Its Tafel slope of 72.0 mV dec^{-1} was the smallest among the investigated samples. Sample 14_2 exhibited the second-lowest slope of 81.1 mV dec^{-1}, whereas considerably larger values of 93.8 and 94.6 mV dec^{-1} were obtained for Samples 12_2 and 15_2, respectively. A smaller Tafel slope means that a smaller additional increase in overpotential is required to produce a tenfold increase in current density within the fitted Tafel region. The low slope of Sample 13_2 is

therefore consistent with its increasingly favorable polarization response as the HER current density increases.

The Tafel slope increased from 72.0 mV dec^{-1} for Sample 13_2 to 81.1 mV dec^{-1} for Sample 14_2 and 94.6 mV dec^{-1} for Sample 15_2 as the deposition current density was increased from 10 to 20 mA cm^{-2}. This trend is reflected directly in the operating overpotentials. Although Samples 13_2, 14_2, and 15_2 differ by only approximately 1 mV at 1 mA cm^{-2}, their η_{10} values differ by as much as 22 mV. Thus, the advantage of the coating deposited at 10 mA cm^{-2} becomes progressively more significant at higher HER current densities.

Excellent linearity of the Tafel regressions was obtained for all four electrodes. The R^2 values ranged from 0.9992 to 0.9998, with Sample 14_2 exhibiting the highest value of 0.9998. These coefficients indicate that the polarization response over the selected 1–5 mA cm^{-2} interval is very well described by the linear Tafel relationship and support the use of the fitted slopes for comparative kinetic analysis.

The apparent exchange current densities show a trend that differs from the ranking based on operating overpotential and Tafel slope. The highest apparent j_0 was obtained for Sample 15_2, at 6.69 $\cdot 10^{-6}$ A cm^{-2}, followed by Sample 12_2 at 4.73 $\cdot 10^{-6}$ A cm^{-2} and Sample 14_2 at 3.03 $\cdot 10^{-6}$ A cm^{-2}. Sample 13_2, despite exhibiting the lowest operating overpotentials and smallest Tafel slope, had the lowest apparent j_0, 1.49 $\cdot 10^{-6}$ A cm^{-2}. The corresponding 95% confidence intervals were narrow: 0.00453–0.00494, 0.00143–0.00156, 0.00296–0.00311, and 0.00644–0.00695 mA cm^{-2} for Samples 12_2, 13_2, 14_2, and 15_2, respectively.

This apparent discrepancy illustrates why extrapolated j_0 values should not be considered in isolation when ranking the practical HER performance of these coatings. The apparent exchange current density is calculated by extrapolating the fitted Tafel relationship toward zero overpotential and is therefore strongly dependent on both the slope and intercept of the regression. In contrast, η_1, η_5, and

η_{10} describe the experimentally observed polarization required to achieve defined current densities. In the present dataset, these directly supported operating overpotentials consistently identify Sample 13_2 as the best-performing electrode at intermediate and higher HER current densities despite its lower apparent j_0.

Sample 12_2, deposited at the lowest current density of 5 mA cm^{-2}, showed the least favorable overall polarization behavior. It exhibited the highest overpotentials at all three investigated current-density benchmarks: η_1 = 216 mV, η_5 = 283 mV, and η_{10} = 312 mV. Its Tafel slope of 93.8 mV dec^{-1} was also substantially larger than those of Samples 13_2 and 14_2. These results indicate that a deposition current density of 5 mA cm^{-2} was insufficient to produce the most favorable Ni coating for HER under the investigated deposition conditions.

Increasing the deposition current density from 5 to 10 mA cm^{-2} resulted in a substantial improvement in HER performance. Sample 13_2 showed decreases of approximately 13, 29, and 34 mV in η_1, η_5, and η_{10}, respectively, compared with Sample 12_2. Simultaneously, the Tafel slope decreased from 93.8 to 72.0 mV dec^{-1}. These changes demonstrate that increasing the deposition current density from 5 to 10 mA cm^{-2} produced a coating with a more favorable polarization response and a stronger increase in HER current with increasing cathodic polarization.

Further increasing the deposition current density above 10 mA cm^{-2} did not provide an additional improvement. Sample 14_2, deposited at 15 mA cm^{-2}, retained relatively favorable performance but required 7 mV more overpotential at 5 mA cm^{-2} and 9 mV more at 10 mA cm^{-2} than Sample 13_2. At the highest deposition current density of 20 mA cm^{-2}, Sample 15_2 exhibited a further deterioration in the polarization response, with η_5 and η_{10} increasing to 271 and 300 mV, respectively. Its Tafel slope also increased to 94.6 mV dec^{-1}.

Taken together, these results reveal a non-monotonic dependence of HER performance on the Ni electrodeposition current density at 60 °C. Increasing the

deposition current density from 5 to 10 mA cm^{-2} markedly improved the catalytic response, whereas further increases to 15 and 20 mA cm^{-2} progressively reduced the advantage. Based primarily on the experimentally determined operating overpotentials, the overall HER activity can be ranked approximately as:

Sample 13_2 > Sample 14_2 > Sample 15_2 > Sample 12_2.

Thus, among the four deposition conditions investigated at 60 °C, a deposition current density of **10 mA cm^{-2} (Sample 13_2)** produced the most favorable Ni coating for alkaline HER. This electrode combines the lowest η_5 and η_{10} values with the smallest Tafel slope and excellent linearity of the Tafel regression. Sample 14_2 provides the second-best overall performance and is particularly close to Sample 13_2 at low current density, whereas Samples 15_2 and 12_2 require progressively greater polarization at higher HER current densities.

The electrochemical results therefore suggest the existence of an optimum deposition-current-density range for Ni coatings prepared at 60 °C rather than a simple improvement with increasing deposition current density. The origin of this optimum cannot be established from the electrochemical measurements alone. Changes in electrodeposition current density may influence nucleation and growth of the Ni deposit and consequently modify coating morphology, roughness, porosity, grain structure, thickness, surface composition, and electrochemically accessible surface area. Correlation of the present HER results with the morphological and structural characterization reported for these coatings would therefore be valuable for identifying the physical origin of the superior performance of Sample 13_2.

1.2.4 Deposition temperature 30 ºC

To investigate the influence of the electrodeposition temperature of the catalytically active Ni layer from a DES-based electrolyte on HER kinetics in

1 M NaOH, electrodeposition was also carried out at 30 °C. A detailed description of the electrodeposition conditions used for each sample is provided in Table 7.

For each sample, a series of LSV measurements was performed. The resulting data are presented in Figures 18–21.

Table 7. Electrodeposition conditions for Ni coatings prepared from the DES-based electrolyte.

Sample	**Temperature during coating deposition, t / ºC**	**Deposition current density, j / mA/cm^2**
16_2	30	5
17_2		10
18_2		15
19_2		20

A similar trend was observed for the obtained curves, as noted previously. For each sample, the first LSV curve differed slightly from the subsequent curves, which may be attributed to more pronounced surface modification during the initial contact with the NaOH electrolyte.

Admit that Figure 22 compares the seventh LSV curves recorded for the investigated samples electrodeposited at 30 °C using current densities of 5, 10, 15, and 20 mA cm^{-2}.

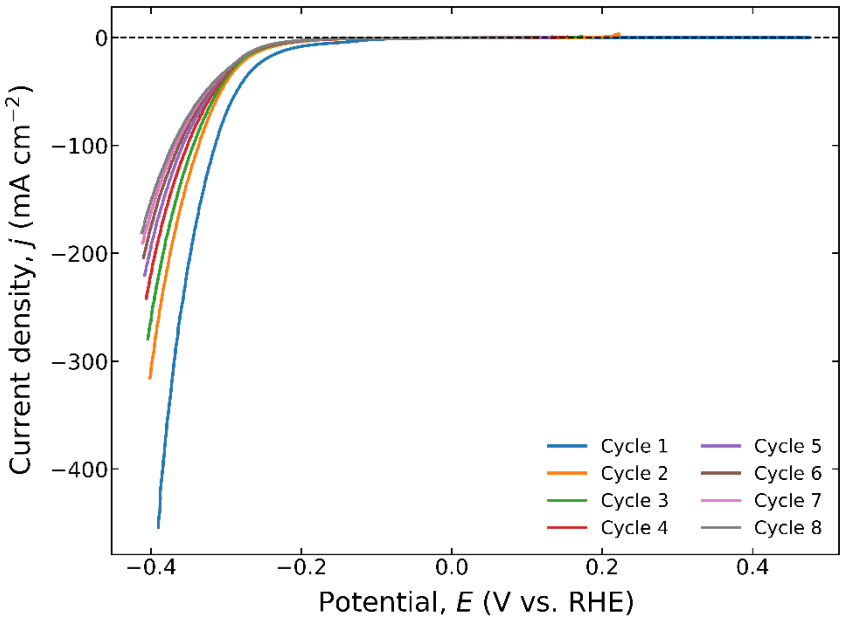


Figure 18. Linear sweep voltammograms of Ni-coated Sample 16_2 recorded during eight consecutive cycles in 1 M NaOH at 25 °C with a scan rate of 2 mV s^{-1}. Potentials are reported versus RHE, and currents are normalized to the geometric electrode area.

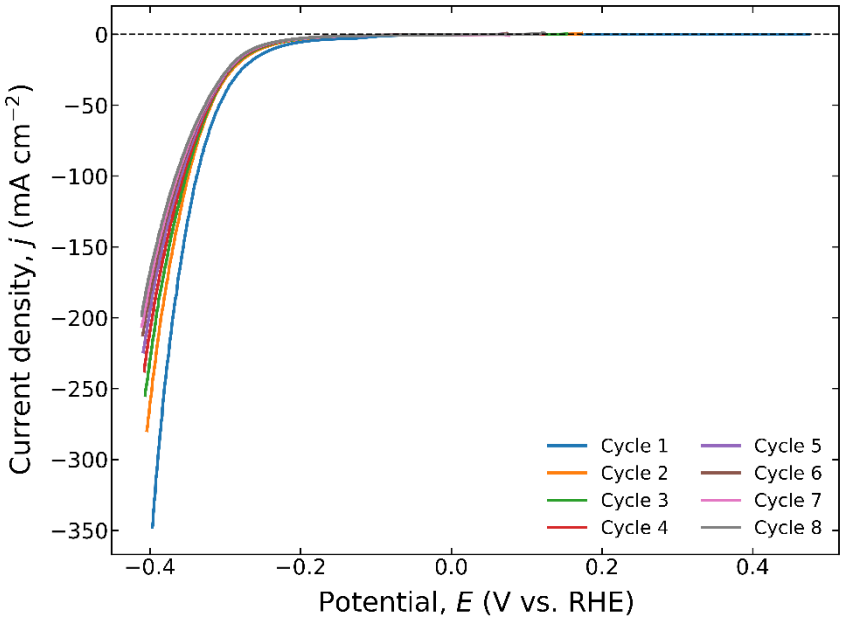


Figure 19. Linear sweep voltammograms of Ni-coated Sample 17_2 recorded during eight consecutive cycles in 1 M NaOH at 25 °C with a scan rate of 2 mV s^{-1}. Potentials are reported versus RHE, and currents are normalized to the geometric electrode area.

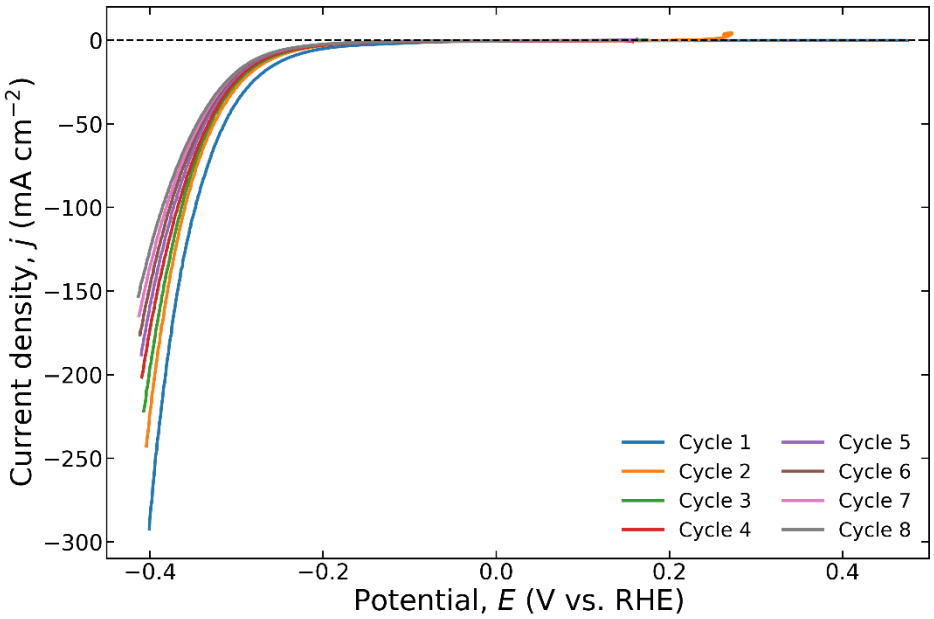


Figure 20. Linear sweep voltammograms of Ni-coated Sample 18_2 recorded during eight consecutive cycles in 1 M NaOH at 25 °C with a scan rate of 2 mV s^{-1}. Potentials are reported versus RHE, and currents are normalized to the geometric electrode area.

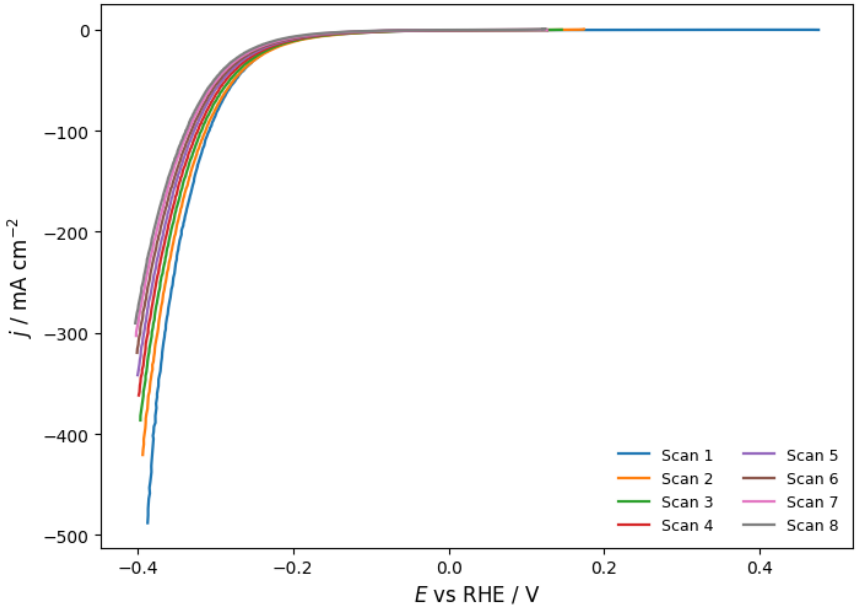


Figure 21. Linear sweep voltammograms of Ni-coated Sample 19_2 recorded during eight consecutive cycles in 1 M NaOH at 25 °C with a scan rate of 2 mV s^{-1}. Potentials are reported versus RHE, and currents are normalized to the geometric electrode area.

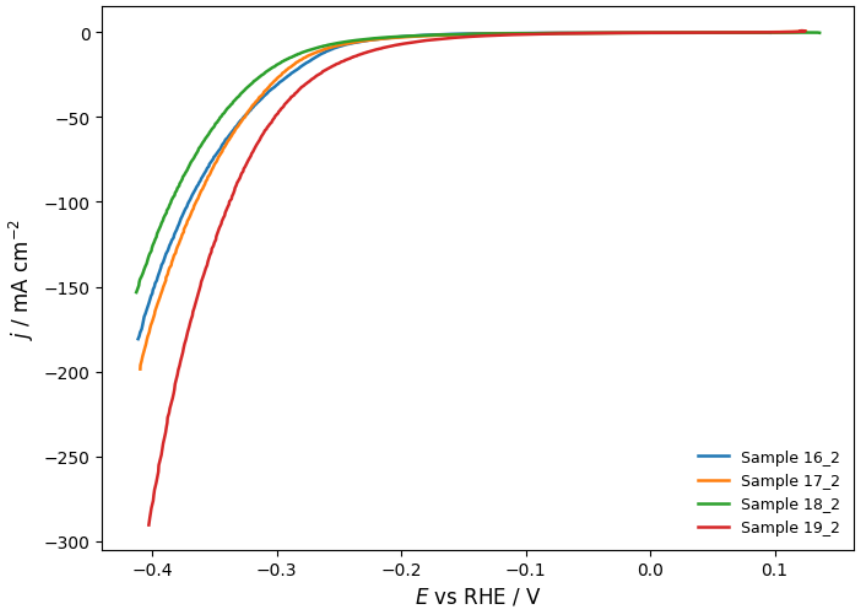


Figure 22. Linear sweep voltammograms corresponding to Cycle 8 for Ni-coated Samples 16_2, 17_2, 18_2 and 19_2 recorded in 1 M NaOH at 25 °C with a scan rate of 2 mV s^{-1}. Potentials are reported versus the reversible hydrogen electrode (RHE), and current densities are normalized to the geometric electrode area. Temperature of electrodeposition of Ni is 30ºC).

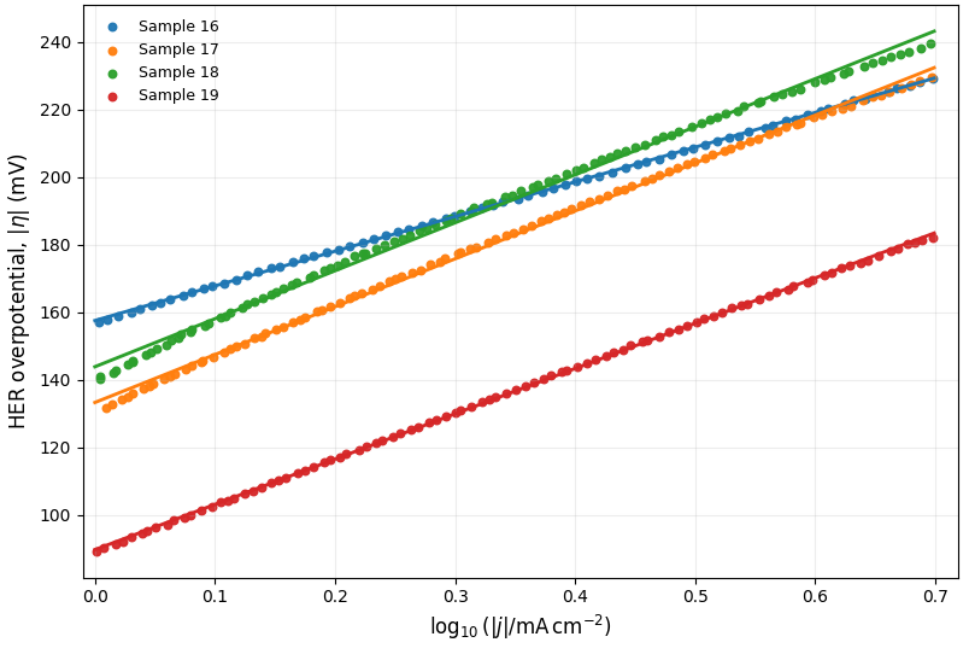


Figure 23. Tafel plots derived from the eighth-cycle polarization curves of Ni-coated Samples 16_2, 17_2, 18_2, and 19_2 recorded in 1 M NaOH at 25 °C. Current densities were normalized to the geometric electrode area of 4 cm^2, and potentials were converted from saturated Ag/AgCl to the RHE scale. Solid lines represent linear regressions over the current-density interval of 1–5 mA cm^{-2}.

All HER parameters calculated from Tafel plots are summarized in Table 8.

Table 8. Tafel kinetic parameters and HER overpotentials derived from the eighth-cycle polarization curves of Ni-coated Samples 16_2, 17_2, 18_2, and 19_2 in 1 M NaOH at 25 °C.

Sample	Tafel intercept, a (V)	Tafel slope, $\lvert b \rvert$ (mV dec^{-1})	R^2	Apparent j_0 (A cm^{-2})	95% CI for j_0 (mA cm^{-2})	η_1 (mV)	η_5 (mV)	η_{10} (mV)	η_{10} determination
16_2	0.1576	102.7	0.99978	2.98×10^{-5}	0.0293–0.0302	156.7	228.5	259.4	Extrapolated
17_2	0.1333	141.8	0.99855	1.16×10^{-4}	0.1138–0.1190	132.5	231.6	274.3	Extrapolated
18_2	0.1439	142.1	0.99653	9.85×10^{-5}	0.0950–0.1022	143.1	242.4	285.2	Extrapolated
19_2	0.0897	134.1	0.99982	2.17×10^{-4}	0.2160–0.2189	88.9	182.6	223.0	Extrapolated

The Tafel slopes obtained for the investigated electrodes ranged from 102.7 to 142.1 mV dec^{-1}, indicating noticeable differences in HER kinetics among the Ni-coated samples. Sample 16_2 exhibited the lowest Tafel slope of 102.7 mV dec^{-1}, whereas higher and relatively similar values were obtained for Samples 17_2 and 18_2, namely 141.8 and 142.1 mV dec^{-1}, respectively. Sample 19_2 showed an intermediate Tafel slope of 134.1 mV dec^{-1}. The lower Tafel slope observed for Sample 16_2 indicates a smaller increase in overpotential required to produce a tenfold increase in current density within the investigated kinetic region. However, the Tafel slope alone does not determine the overall catalytic performance, since the position of the Tafel line, reflected by its intercept and the corresponding apparent exchange current density, must also be considered.

The linear regressions showed a very good agreement with the experimental data. The coefficients of determination R^2 ranged from 0.99653 to 0.99982, confirming a high degree of linearity within the selected 1–5 mA cm^{-2} current-density interval. The highest R^2 value was obtained for Sample 19_2 (0.99982), followed by Sample 16_2 (0.99978), Sample 17_2 (0.99855), and Sample 18_2 (0.99653). These

values support the suitability of the selected current-density interval for comparison of the apparent Tafel parameters of the investigated electrodes.

More pronounced differences between the samples were observed for the apparent exchange current density. Sample 19_2 exhibited the highest apparent j_0, 2.17×10^{-4} A cm^{-2}, followed by Sample 17_2 (1.16×10^{-4} A cm^{-2}) and Sample 18_2 (9.85×10^{-5} A cm^{-2}). The lowest value, 2.98×10^{-5} A cm^{-2}, was obtained for Sample 16_2. Thus, despite Sample 16_2 exhibiting the lowest Tafel slope, Sample 19_2 displayed the highest apparent exchange current density. This result demonstrates that evaluation of HER activity based exclusively on the Tafel slope could lead to an incomplete assessment of electrode performance.

The calculated overpotentials further emphasize the differences in HER activity. At a current density magnitude of 1 mA cm^{-2}, the overpotential magnitudes were approximately 156.7, 132.5, 143.1, and 88.9 mV for Samples 16_2, 17_2, 18_2, and 19_2, respectively. Sample 19_2 therefore required the lowest overpotential to reach this current density, indicating the most favorable HER response in the low-current-density region. At 5 mA cm^{-2}, the corresponding overpotential magnitudes were 228.5, 231.6, 242.4, and 182.6 mV, respectively. Sample 19_2 again exhibited a substantially lower overpotential than the other investigated electrodes.

The values of η_{10}, corresponding to a current density magnitude of 10 mA cm^{-2}, were 259.4, 274.3, 285.2, and 223.0 mV for Samples 16_2, 17_2, 18_2, and 19_2, respectively.

Overall, the Tafel analysis indicates that Sample 19_2 provides the most favorable HER performance among the investigated samples, as evidenced by its lowest overpotentials at 1, 5, and 10 mA cm^{-2} and its highest apparent exchange current density. Sample 16_2, in contrast, exhibits the lowest Tafel slope but requires a higher overpotential at the investigated current densities. Samples 17_2 and 18_2 show broadly comparable Tafel slopes, although Sample 17_2 exhibits a somewhat

higher apparent exchange current density and lower overpotentials than Sample 18_2. These differences indicate that the properties of the electrodeposited Ni layers influence the HER kinetics even though all coatings were deposited at the same temperature of 30 °C.

It should be emphasized that the calculated j_0 values are referred to as apparent exchange current densities, since they are obtained by extrapolation of the experimentally fitted Tafel region toward zero overpotential. Consequently, they should primarily be used for comparative assessment of the investigated Ni-coated electrodes rather than interpreted as independently measured equilibrium exchange current densities.

1.2.5 Influence of Ni Electrodeposition Temperature on HER Kinetics

To evaluate the influence of the Ni electrodeposition temperature on the subsequent hydrogen evolution reaction (HER) performance, the electrochemical results obtained for coatings deposited from the DES-based electrolyte at **30, 40, 50, and 60 °C** were compared. Because the electrodeposition current density also strongly affects the properties of the resulting Ni coating, the effect of temperature should be assessed by comparing samples prepared at the **same deposition current density**, rather than simply comparing the best-performing electrode from each temperature series. The investigated series cover deposition current densities of 5–20 mA cm^{-2}, although the 50 °C series contains samples deposited at 10, 15, and 20 mA cm^{-2} only. All HER measurements were performed under the same electrochemical conditions in 1 M NaOH at 25 °C, allowing direct comparison of the polarization and Tafel parameters.

The comparison demonstrates that the electrodeposition temperature has a pronounced influence on the HER response of the resulting Ni coatings. Importantly, however, the temperature dependence is **not monotonic** and varies with the

electrodeposition current density. This observation indicates that deposition temperature and deposition current density should be regarded as coupled preparation parameters controlling the properties of the catalytically active Ni layer.

Comparison at a deposition current density of 10 mA cm⁻²

The clearest temperature comparison can be made at an electrodeposition current density of **10 mA cm⁻²**, for which samples are available at all four temperatures. At 40 °C, Sample 3 exhibited a Tafel slope of **121.6 mV dec⁻¹**, with overpotentials of **154.7 mV at 1 mA cm⁻²**, **240.6 mV at 5 mA cm⁻²**, and **271.1 mV at 10 mA cm⁻²**.

Increasing the deposition temperature to 50 °C resulted in Sample 9_2, for which the Tafel slope was **123.94 mV dec⁻¹**. Its η_1 and η_5 values were **166.4 and 253.0 mV**, respectively, while η_{10} was estimated as **290.4 mV**. Thus, compared with the corresponding coating deposited at 40 °C, deposition at 50 °C did not improve HER activity at this deposition current density. Instead, the operating overpotentials increased by approximately **11.7 mV at 1 mA cm⁻²** and **12.4 mV at 5 mA cm⁻²**.

A distinctly different behavior was observed for the coating deposited at 60 °C. Sample 13_2 showed a Tafel slope of only **72.0 mV dec⁻¹**, considerably lower than the values obtained at 40 and 50 °C. Its η_1, η_5, and η_{10} values were **203, 254, and 278 mV**, respectively. Although the Tafel slope was strongly reduced, the absolute operating overpotentials did not improve relative to the 40 °C sample. In particular, η_5 increased from 240.6 mV at 40 °C to 254 mV at 60 °C. This illustrates that a reduction in Tafel slope does not necessarily correspond to a lower absolute polarization at a given current density.

At 30 °C, Sample 17_2 exhibited a Tafel slope of **141.8 mV dec⁻¹**, with overpotential magnitudes of **132.5, 231.6, and 274.3 mV** at 1, 5, and 10 mA cm⁻², respectively. The coating deposited at 30 °C therefore exhibited the **lowest η_1 and η_5 values among the samples prepared at 10 mA cm⁻²**, although its Tafel slope

was the largest. At 5 mA cm^{-2}, for example, η_5 increased in the sequence **30 °C (231.6 mV) < 40 °C (240.6 mV) < 50 °C (253.0 mV) ≈ 60 °C (254 mV)**. Thus, based on operating overpotential, increasing the electrodeposition temperature above 30 °C did not improve the HER performance at this deposition current density.

The Tafel slopes, however, show a different temperature dependence: **141.8, 121.6, 123.94, and 72.0 mV dec^{-1}** for deposition at 30, 40, 50, and 60 °C, respectively. Consequently, increasing the deposition temperature to 60 °C produced a substantially smaller Tafel slope but simultaneously shifted the polarization response toward higher absolute overpotential at low and intermediate current density. This distinction confirms that the Tafel slope and operating overpotential characterize different aspects of HER behavior and should be considered together when evaluating the effect of electrodeposition temperature.

Comparison at 15 mA cm^{-2}

A similar comparison can be made for coatings deposited at **15 mA cm^{-2}**. At 40 °C, Sample 4 exhibited a Tafel slope of **124.7 mV dec^{-1}**, η_1 = **168.4 mV**, and η_5 = **256.2 mV**. At 50 °C, Sample 10_2 showed a substantially smaller Tafel slope of **92.25 mV dec^{-1}**, but its operating overpotentials increased to **216.8 mV at 1 mA cm^{-2}** and **281.3 mV at 5 mA cm^{-2}**.

For deposition at 60 °C, Sample 14_2 exhibited a Tafel slope of **81.1 mV dec^{-1}**, η_1 = **204 mV**, η_5 = **261 mV**, and η_{10} = **287 mV**. Thus, increasing the deposition temperature from 40 to 50–60 °C again substantially reduced the Tafel slope but did not produce a corresponding decrease in the overpotential required to sustain a defined geometric current density.

The coating deposited at 30 °C, Sample 18_2, showed a Tafel slope of **142.1 mV dec^{-1}**, η_1 = **143.1 mV**, and η_5 = **242.4 mV**. It therefore exhibited the lowest operating overpotentials in this group despite having the largest Tafel slope. At 5

mA cm^{-2}, the overpotential sequence was approximately **30 °C (242.4 mV) < 40 °C (256.2 mV) < 60 °C (261 mV) < 50 °C (281.3 mV)**. The results at 15 mA cm^{-2} deposition current density therefore reinforce the observation that lower deposition temperatures, particularly 30–40 °C, favor lower absolute HER polarization, whereas higher deposition temperatures can favor smaller Tafel slopes.

Comparison at 20 mA cm^{-2}

The influence of temperature is particularly pronounced for coatings deposited at the highest investigated current density of **20 mA cm^{-2}**. Sample 5, prepared at 40 °C, exhibited a Tafel slope of **115.4 mV dec^{-1}**, with η_1 and η_5 values of **188.0 and 269.5 mV**, respectively. At 50 °C, Sample 11_2 exhibited a somewhat smaller Tafel slope of **104.66 mV dec^{-1}**, but substantially higher operating overpotentials of **238.6 mV at 1 mA cm^{-2}** and **311.7 mV at 5 mA cm^{-2}**.

Increasing the deposition temperature further to 60 °C produced Sample 15_2, characterized by a Tafel slope of **94.6 mV dec^{-1}** and overpotentials of **204, 271, and 300 mV** at 1, 5, and 10 mA cm^{-2}, respectively. The decrease in Tafel slope with increasing deposition temperature is therefore again evident, although the operating overpotential does not follow the same monotonic dependence.

The most favorable behavior at this deposition current density was observed for Sample 19_2, deposited at **30 °C**. It exhibited overpotential magnitudes of only **88.9 mV at 1 mA cm^{-2}** and **182.6 mV at 5 mA cm^{-2}**, substantially lower than those of the corresponding coatings deposited at higher temperatures. Its Tafel slope was **134.1 mV dec^{-1}**, while the apparent exchange current density of **2.17×10^{-4} A cm^{-2}** was the highest within the 30 °C series.

The η_5 value provides a particularly clear illustration of the temperature effect at 20 mA cm^{-2} deposition current density: approximately **182.6 mV at 30 °C, 269.5 mV at 40 °C, 311.7 mV at 50 °C, and 271 mV at 60 °C**. The difference

between the best and least favorable conditions is therefore approximately **129 mV**, demonstrating that electrodeposition temperature can have a very substantial effect on the subsequent HER polarization response.

Overall effect of electrodeposition temperature

Taken together, the results demonstrate that the temperature used for Ni electrodeposition from the DES-based electrolyte significantly influences the subsequent HER kinetics. The effect cannot, however, be described by a simple monotonic relationship in which increasing deposition temperature continuously improves or deteriorates catalytic performance. Instead, the influence depends strongly on the electrodeposition current density and on the particular HER descriptor considered.

A notable general trend is that coatings deposited at **60 °C tend to exhibit comparatively small Tafel slopes**. For example, the Tafel slopes at deposition current densities of 10, 15, and 20 mA cm^{-2} were **72.0, 81.1, and 94.6 mV dec^{-1}**, respectively. These values indicate a favorable increase in HER current with additional cathodic polarization. Nevertheless, the 60 °C coatings do not generally exhibit the lowest absolute overpotentials.

In contrast, the coatings deposited at **30 °C show particularly favorable operating overpotentials**. Within this series, Sample 19_2 displayed η_1 and η_5 magnitudes of only **88.9 and 182.6 mV**, respectively, and was identified as the most favorable HER electrode among the samples deposited at 30 °C. Moreover, comparisons at equivalent deposition current densities show that the 30 °C coatings generally require less cathodic polarization to reach 1 and 5 mA cm^{-2} than the corresponding coatings prepared at 40–60 °C.

The results therefore reveal an important distinction between **Tafel kinetics and practical polarization performance**. Increasing electrodeposition temperature,

particularly toward 60 °C, can decrease the Tafel slope, indicating a more favorable incremental current response to increasing polarization. At the same time, this does not necessarily shift the entire polarization curve toward lower overpotentials. Conversely, coatings deposited at 30 °C can exhibit larger Tafel slopes while requiring considerably less absolute overpotential to sustain a specified HER current density.

This behavior is consistent with the electrodeposition temperature affecting the physicochemical characteristics of the Ni coating rather than simply changing a single kinetic parameter. Changes in deposition conditions may influence Ni nucleation and growth and, consequently, coating morphology, roughness, porosity, grain structure, thickness, surface composition, and electrochemically accessible surface area. The report itself notes that these factors may contribute to differences in HER performance and that electrochemical measurements alone cannot identify which structural characteristic is responsible. Similar considerations are made for the 60 °C series, where correlation with morphological and structural characterization is identified as necessary for establishing the physical origin of the observed catalytic differences.

Overall, the electrochemical results indicate that **lower Ni electrodeposition temperatures, particularly 30 °C, are favorable for minimizing the operating overpotential of the investigated DES-derived Ni coatings**, whereas deposition at **60 °C generally produces lower Tafel slopes**. Therefore, no single electrodeposition temperature can be identified as universally optimal on the basis of the Tafel slope alone. When practical HER activity at defined geometric current densities is taken as the principal criterion, the present dataset indicates a clear advantage for selected coatings deposited at 30 °C, most notably Sample 19_2. Establishing the origin of this temperature dependence requires correlation of the

electrochemical results with the morphological, structural, and compositional characterization of the corresponding Ni coatings.

1.2.6 Comparison of HER Performance with Literature Data and Benefits of DES-Assisted Ni Electrodeposition

To place the electrocatalytic performance of the Ni coatings developed in the present work into a broader context, the experimentally determined HER parameters were compared with representative literature data reported for metallic Ni and electrodeposited Ni-based coatings in alkaline electrolytes. Particular attention was given to studies employing electrodeposition, including deposition from deep eutectic solvent (DES)-based electrolytes, because these systems are most directly relevant to the preparation route investigated here.

The comparison should be treated as semi-quantitative rather than as a strict catalyst ranking. HER parameters reported in different studies depend not only on the intrinsic catalytic properties of the material but also on the electrolyte composition and concentration, electrode substrate, geometric and electrochemically active surface areas, catalyst loading, scan rate, iR compensation, conditioning protocol, temperature, and the method used to determine the Tafel region and overpotential. In the present work, HER measurements were performed in 1 M NaOH at 25 °C, currents were normalized to a geometric area of 4 cm^2, and Tafel regressions were performed over the common current-density interval of 1–5 mA cm^{-2}. In contrast, most literature studies considered below used 1 M KOH and different experimental protocols.

Among the Ni coatings investigated in the present work, Sample 19_2, electrodeposited from the DES-based electrolyte at 30 °C and 20 mA cm^{-2}, showed particularly favorable polarization behavior. Its Tafel slope was 134.1 mV dec^{-1}, the apparent exchange current density was 2.17×10^{-4} A cm^{-2}, and the overpotential

magnitudes at 1 and 5 mA cm^{-2} were 88.9 and 182.6 mV, respectively. The calculated η_{10} value was 223.0 mV. Because the Tafel regression for this series was restricted to 1–5 mA cm^{-2}, η_{10} for Sample 19_2 is an extrapolated value and must therefore be distinguished from η_{10} values measured directly within a published polarization curve.

A representative comparison is given in Table 9. Four representative electrodes from the present work were selected to cover the investigated Ni deposition temperatures of 30, 40, 50, and 60 °C. Their HER properties varied substantially despite their common chemical identity as Ni coatings deposited from a DES-based electrolyte. Sample 19_2, prepared at 30 °C and 20 mA cm^{-2}, exhibited an η_{10} of approximately 223 mV, a Tafel slope of 134.1 mV dec^{-1}, and the highest apparent exchange current density among the selected samples, $2.17 \cdot 10^{-4}$ A cm^{-2}. Sample 3, prepared at 40 °C and 10 mA cm^{-2}, exhibited η_{10} = 271.1 mV and a Tafel slope of 121.6 mV dec^{-1}, whereas Sample 9_2 prepared at 50 °C gave η_{10} = 290.4 mV and 123.94 mV dec^{-1}. Particularly favorable Tafel kinetics were observed for Sample 13_2 deposited at 60 °C and 10 mA cm^{-2}, which exhibited a Tafel slope of only 72.0 mV dec^{-1} and a directly determined η_{10} of 278 mV. These values are already assembled in the current version of Table 9.

An important feature of the present results is therefore that the DES deposition process provides considerable scope for tuning the subsequent HER response through relatively simple changes in the electrodeposition conditions. The influence of temperature was not monotonic, and the report demonstrates that deposition temperature and current density act as coupled preparation variables. This sensitivity is important from a catalyst-design perspective because it indicates that the electrochemical properties of pure Ni can be modified without changing its nominal chemical composition.

Table 9. Comparison of HER performance of Ni coatings electrodeposited from DES-based electrolytes in the present work with bare Ni and pure Ni electrocatalysts prepared by aqueous- and DES-assisted electrodeposition reported in the literature.

Electrocatalyst	Preparation / electrolyte for deposition	HER test electrolyte	η_{10} (mV)	Tafel slope (mV dec^{-1})	j_0 (A cm^{-2})	DOI / source
Sample 19_2, present work	Ni on Cu, DES electrodeposition, 30 °C, 20 mA cm^{-2}	1 M NaOH, 25 °C	**223***	**134.1**	**2.17×10^{-4}**	Present work
Sample 3, present work	Ni on Cu, DES electrodeposition, 40 °C, 10 mA cm^{-2}	1 M NaOH, 25 °C	271.1	121.6	5.051×10^{-5}	Present work
Sample 9_2, present work	Ni on Cu, DES electrodeposition, 50 °C, 10 mA cm^{-2}	1 M NaOH, 25 °C	290.4*	123.94	4.54×10^{-5}	Present work
Sample 13_2, present work	Ni on Cu, DES electrodeposition, 60 °C, 10 mA cm^{-2}	1 M NaOH, 25 °C	278	72.0	1.49×10^{-6}	Present work
Ni@PGE from ethaline DES	Ni nanoparticles, ChCl/ethylene glycol DES	1 M KOH	154	130	8.3×10^{-4}	**10.1007/s10008-022-05177-z**
Pulsed-electrodeposited Ni, citrate bath	Ni on pencil graphite, aqueous citrate bath, 40 °C	1 M KOH	210	208	9.3×10^{-4}	**10.3390/ma18122775**
Uncoated Ni microelectrode, 293 K	Bulk Ni microelectrode	1 M KOH	265	—	—	**10.1002/chem.202403030**

Comparison with conventional and aqueous-electrodeposited Ni

The performance of the present coatings compares favorably with several literature benchmarks. For example, an uncoated Ni microelectrode tested in 1 M KOH required approximately **265 mV to achieve 10 mA cm^{-2}**. This value is higher than the approximately 223 mV obtained for Sample 19_2, although the latter value was derived by Tafel extrapolation and therefore should not be treated as a strictly equivalent directly measured η_{10}. The bare-Ni benchmark is included in the current Table 9.

A particularly informative comparison is provided by the study in which pure Ni nanoparticles were electrodeposited either from a conventional aqueous acetate electrolyte or from an ethaline DES. Ni prepared from the aqueous electrolyte

required **164 mV at 10 mA cm^{-2}** and exhibited a Tafel slope of **147 mV dec^{-1}**, whereas the DES-derived Ni required **154 mV** and showed a lower Tafel slope of **130 mV dec^{-1}**. The corresponding exchange current densities were 7.7×10^{-4} and 8.3×10^{-4} A cm^{-2}, respectively. Thus, changing the deposition medium from aqueous acetate to ethaline simultaneously decreased η_{10}, decreased the Tafel slope, and increased j_0. The article DOI is **10.1007/s10008-022-05177-z**.

These literature values are particularly useful when evaluating the Tafel behavior observed in the present study. Sample 3 exhibited a Tafel slope of **121.6 mV dec^{-1}**, already below the 130 mV dec^{-1} reported for the literature DES-derived Ni and substantially below the 147 mV dec^{-1} obtained for aqueous-electrodeposited Ni. Even more notably, Sample 13_2 exhibited a slope of only **72.0 mV dec^{-1}**. The latter value is approximately **45% lower than the literature DES-Ni value of 130 mV dec^{-1} and approximately 51% lower than the aqueous-Ni value of 147 mV dec^{-1}**. This represents an important indication that optimization of the DES electrodeposition conditions can produce pure Ni coatings with highly favorable HER polarization kinetics.

At the same time, Tafel slope should not be interpreted independently of operating overpotential. This is evident within the present dataset itself: Sample 13_2 provides the smallest Tafel slope, whereas Sample 19_2 displays particularly favorable low-current polarization behavior. Consequently, the results demonstrate that the deposition conditions can influence different HER descriptors to different extents rather than simply shifting all kinetic parameters in parallel.

Evidence from DES-electrodeposited nanostructured Ni

The beneficial influence of DES electrodeposition on pure Ni is independently supported by Wang et al. In their study, nanostructured Ni films were electrodeposited directly onto Cu from $NiCl_2$-containing choline chloride/urea and

choline chloride/ethylene glycol DESs. The morphology of the resulting Ni depended strongly on the DES and electrodeposition conditions, and homogeneous needle-like nanostructures could be obtained. The authors attributed the enhanced HER activity primarily to this needle morphology and the associated increase in electrochemically accessible surface area. The DOI is **10.1016/j.ijhydene.2018.06.188**.

This study is highly relevant to the present work because both approaches involve the direct electrodeposition of **pure Ni onto a Cu substrate from a ChCl-based DES**. Importantly, Wang et al. concluded that DES electrodeposition represents a promising strategy for producing nano-Ni HER catalysts at relatively low temperatures.

Even stronger evidence was subsequently reported by Protsenko et al. for nanocrystalline Ni electrodeposited from **ethaline**, consisting of choline chloride and ethylene glycol in a 1:2 molar ratio. Their DES-based electrolyte contained 1 M $NiCl_2 \cdot 6H_2O$, with additional water used to modify the properties of the plating bath. The resulting deposits were nanocrystalline, with reported crystallite sizes of approximately 6–10 nm.

Most importantly for the present discussion, Protsenko et al. directly compared the HER behavior of Ni deposited from the DES-based electrolyte with Ni obtained from a conventional aqueous plating bath. They reported that the **HER exchange current for Ni deposited from the DES was approximately 100 times higher than that for Ni deposited from the aqueous bath**. The article DOI is **10.1016/j.ijhydene.2019.07.188**.

Protsenko et al. associated the enhanced behavior of the DES-derived Ni with its nanocrystalline structure and explicitly referred to the earlier work of Wang et al., where DES-electrodeposited nano-Ni also exhibited improved HER performance relative to commercial Ni. These two independent studies therefore provide strong

literature support for the central observation underlying the present work: **the deposition medium and electrodeposition conditions can substantially alter the HER activity of Ni even without intentional alloying or formation of a composite catalyst.**

Significance and advantages of DES-assisted Ni electrodeposition

The combined literature and experimental results emphasize several advantages of DES-assisted electrodeposition for preparing Ni HER catalysts. DESs possess a relatively wide electrochemical potential window, high solubility for many metal salts, negligible vapor pressure, and tunable physicochemical properties. These characteristics make them attractive media for electrochemical deposition and allow metal nucleation and growth to occur under conditions substantially different from those in conventional aqueous electrolytes.

For HER catalyst preparation, perhaps the most important consequence is the possibility of controlling the **microstructure and surface morphology of the Ni deposit**. Wang et al. demonstrated the formation of homogeneous needle-like Ni nanostructures and related their enhanced HER activity to increased electrochemical surface area. Protsenko et al. similarly demonstrated the formation of nanocrystalline Ni and observed an approximately two-order-of-magnitude enhancement in HER exchange current relative to aqueous-deposited Ni.

The present results complement these literature observations. Changing the electrodeposition temperature and current density resulted in pronounced variations in Tafel slope, apparent exchange current density, and operating overpotential, despite all of the investigated coatings remaining nominally Ni. For example, within the 60 °C series alone, changing the deposition current density from 5 to 10 mA cm^{-2} decreased the Tafel slope from 93.8 to **72.0 mV dec^{-1}** and decreased η_{10} from 312 to **278 mV**. The report therefore demonstrates experimentally that the DES

electrodeposition process provides a means of **tuning the catalytic response of pure Ni through control of its preparation conditions**.

The origin of these differences cannot be established from polarization measurements alone. As discussed in the preceding sections, changes in deposition conditions may influence Ni nucleation and growth and consequently alter coating morphology, roughness, porosity, grain structure, thickness, surface composition, and electrochemically accessible surface area. Nevertheless, the magnitude of the observed changes, together with the independent literature evidence for nanostructure formation during DES electrodeposition, strongly supports further investigation of these structure–activity relationships.

Overall assessment and prospects of DES-derived Ni catalysts

Overall, the comparison demonstrates that the Ni coatings developed in the present work exhibit **competitive HER performance relative to representative unmodified and electrodeposited pure-Ni catalysts reported in the literature**. Particularly significant is the low Tafel slope of **72.0 mV dec^{-1} for Sample 13_2**, which compares favorably with the 130 and 147 mV dec^{-1} reported for Ni electrodeposited from ethaline and aqueous acetate electrolytes, respectively. Sample 19_2, meanwhile, provides a favorable combination of relatively low polarization and a comparatively high apparent exchange current density. These observations indicate that optimization of DES electrodeposition conditions can produce pure Ni coatings with kinetic characteristics that are not only comparable with conventional Ni electrodes but, for selected HER descriptors, can be superior.

More broadly, the literature comparison emphasizes the **promising potential of DES utilization for the preparation of Ni-based HER catalysts**. The principal advantage of this approach is that improved catalytic properties can be achieved through control of the electrodeposition environment and resulting Ni structure

without necessarily introducing additional catalytic elements. DES-assisted electrodeposition therefore offers a conceptually simple route from electrolyte formulation and deposition parameters to control of Ni nucleation, morphology, nanocrystallinity, accessible surface area, and ultimately HER performance.

The results of Wang et al. demonstrate that DES electrodeposition can generate HER-active nanostructured Ni directly on Cu at relatively low temperature, while Protsenko et al. demonstrate an approximately two-order-of-magnitude increase in HER exchange current for DES-derived Ni compared with aqueous-deposited Ni. The present work extends this concept by demonstrating that **temperature and current density provide additional variables for tuning the HER behavior within a DES-based Ni electrodeposition system**.

Consequently, DES-assisted electrodeposition should be regarded as a **promising platform for the rational preparation and optimization of pure Ni electrocatalysts for alkaline hydrogen evolution**. Further optimization of DES composition, water content, Ni precursor concentration, deposition temperature, current density, and deposition regime could provide additional control over the structure and electrochemically active surface of the resulting Ni layers. Combined with systematic morphological and structural characterization and long-term HER stability testing, this approach offers considerable potential for developing **efficient, compositionally simple, and non-precious-metal Ni cathodes for alkaline hydrogen production**.

This conclusion is stronger than saying simply that DES is a “green alternative” to aqueous electrodeposition: the available evidence indicates that the DES can function as an **active materials-processing tool for engineering the catalytic properties of electrodeposited Ni**.

1.3 Electrocatalytic HER Performance of Ni/MoS_2 Composite Coatings Electrodeposited from a DES-Based Electrolyte

Ni/MoS_2 composite coatings were investigated to determine whether incorporation of MoS_2 into the electrodeposited Ni matrix could improve the electrocatalytic response toward the hydrogen evolution reaction (HER). The coatings were evaluated in 1 M NaOH at 25 °C, and their HER behavior was assessed from polarization curves and the corresponding Tafel analysis. The comparison focused on characteristic overpotentials at 1, 5, and 10 mA cm^{-2}, Tafel slopes, and apparent exchange current densities.

The results demonstrate that the HER performance of the Ni/MoS_2 coatings depends strongly on the electrodeposition conditions. Across the three investigated series, the characteristic overpotentials did not vary in parallel with the Tafel slopes, indicating that these parameters describe different aspects of the electrode response. Consequently, the performance was evaluated primarily from the experimentally determined operating overpotentials, while Tafel slopes and apparent exchange current densities were used as complementary kinetic descriptors.

Comparison at identical electrodeposition current densities of 5, 10, 15, and 20 mA cm^{-2} provides a particularly useful basis for evaluating the reproducibility and influence of the deposition conditions. Across the three series, the coatings deposited at 5–15 mA cm^{-2} generally showed more favorable HER behavior than those deposited at 20 mA cm^{-2}. The 15 mA cm^{-2} condition was especially reproducible, with comparatively small between-series variation in η_1, η_5, and η_{10}. In contrast, the 20 mA cm^{-2} condition produced larger variations and generally higher operating overpotentials.

Thus, the Ni/MoS_2 results show that incorporation of MoS_2 can contribute to improved HER activity, particularly by reducing the polarization required to reach

technologically relevant current densities. However, the magnitude of this improvement is closely linked to the electrodeposition conditions, emphasizing that optimization of both the Ni/MoS_2 composite composition and the deposition parameters is necessary to maximize HER performance.

1.3.1 Series 1, deposition temperature 40 °C

The polarization behavior and corresponding Tafel plots of the Series 1 coatings are shown in Figures 24-29, and the extracted HER kinetic parameters and characteristic overpotentials are compiled in Table 11 (electrodeposition conditions for each sample are indicated in Table 10).

The first Ni/MoS_2 series showed relatively uniform HER behavior among the four investigated coatings. The Tafel slopes ranged from **95.7 to 107.9 mV dec^{-1}**, with an average value of approximately **104 mV dec^{-1}**, indicating comparatively small kinetic variation within the series.

The characteristic overpotentials were also relatively consistent. η_1 ranged from **166.5 to 186.0 mV**, while η_5 and η_{10} varied from **238.6 to 259.9 mV** and **266.9 to 292.7 mV**, respectively. Among the Series 1 coatings, **Sample 2_1**, deposited at 10 mA cm^{-2}, exhibited the most favorable overall response, combining the lowest Tafel slope (**95.7 mV dec^{-1}**) with the lowest η_5 (**238.6 mV**) and η_{10} (**266.9 mV**).

These results indicate that the first series provided a relatively stable HER response over the investigated deposition-current range. Increasing the deposition current density to 20 mA cm^{-2} did not improve the catalytic response, as Sample 4_1 required higher overpotentials than the coatings produced at lower current densities. Thus, within Series 1, moderate electrodeposition current densities were more favorable for HER activity.

Table 10. Electrodeposition conditions for Ni/MoS_2 coatings prepared from the DES-based electrolyte.

Sample	Temperature during coating deposition, t / °C	Deposition current density, j / mA/cm^2
1_1	40	5
2_1		10
3_1		15
4_1		20

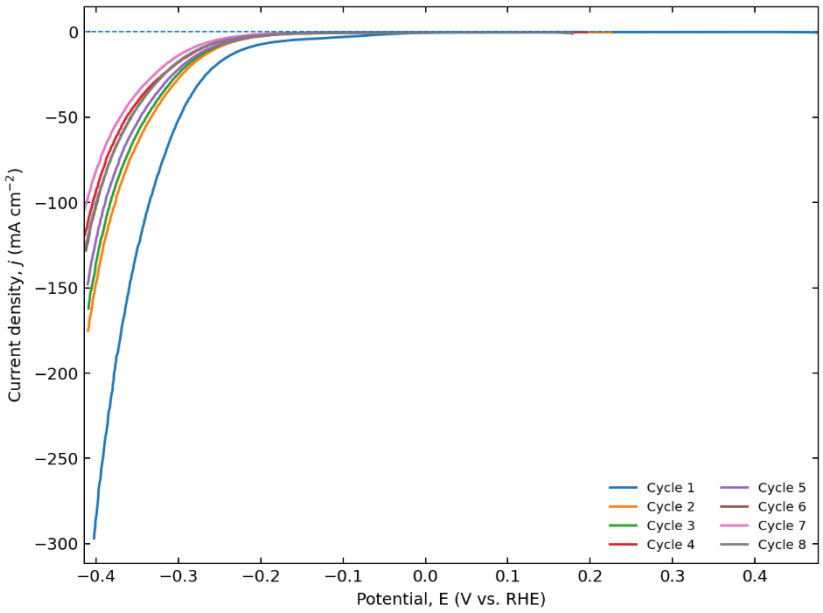


Figure 24. Linear sweep voltammograms of Ni/MoS_2-coated Sample 1_1 recorded during eight consecutive cycles in 1 M NaOH at 25 °C with a scan rate of 2 mV s^{-1}. Potentials are reported versus the reversible hydrogen electrode (RHE), and current densities are normalized to the geometric electrode area of 4 cm^2. A saturated Ag/AgCl electrode was used as the reference electrode.

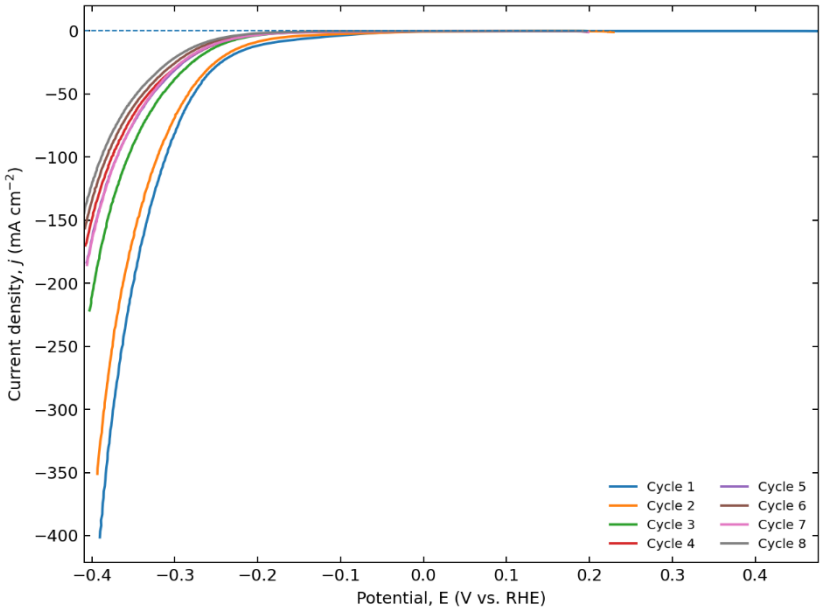


Figure 25. Linear sweep voltammograms of Ni/MoS_2-coated Sample 2_1 recorded during eight consecutive cycles in 1 M NaOH at 25 °C with a scan rate of 2 mV s^{-1}. Potentials are reported versus the reversible hydrogen electrode (RHE), and current densities are normalized to the geometric electrode area of 4 cm^2. A saturated Ag/AgCl electrode was used as the reference electrode.

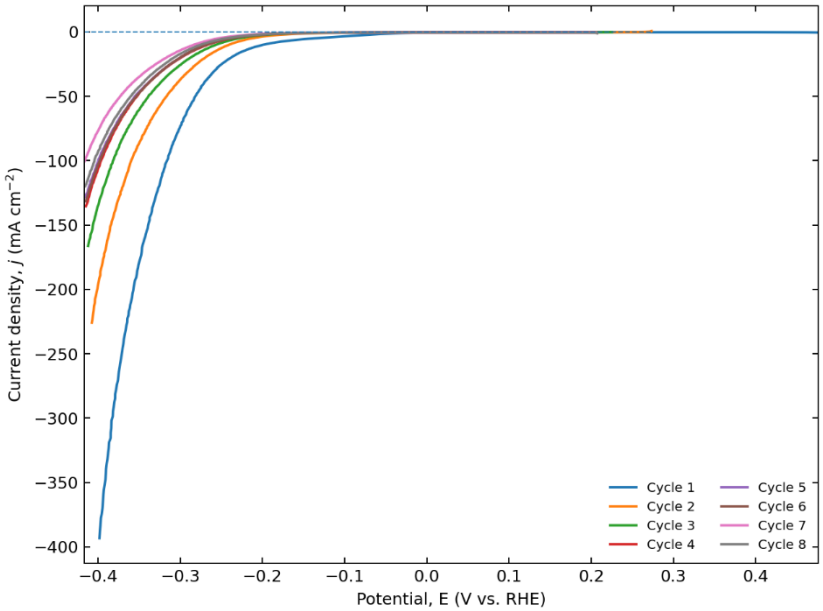


Figure 26. Linear sweep voltammograms of Ni/MoS_2-coated Sample 3_1 recorded during eight consecutive cycles in 1 M NaOH at 25 °C with a scan rate of 2 mV s^{-1}. Potentials are reported versus the reversible hydrogen electrode (RHE), and current densities are normalized to the geometric electrode area of 4 cm^2. A saturated Ag/AgCl electrode was used as the reference electrode.

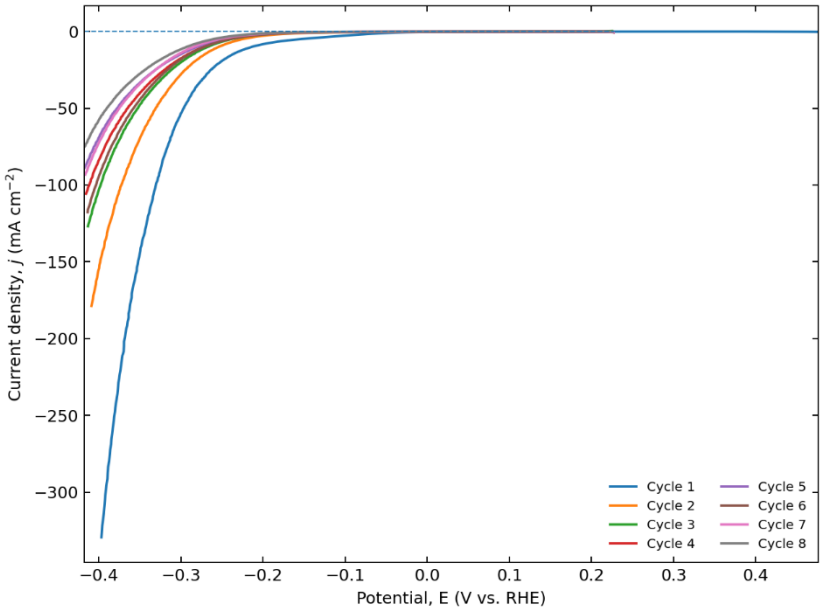


Figure 27. Linear sweep voltammograms of Ni/MoS_2-coated Sample 4_1 recorded during eight consecutive cycles in 1 M NaOH at 25 °C with a scan rate of 2 mV s^{-1}. Potentials are reported versus the reversible hydrogen electrode (RHE).

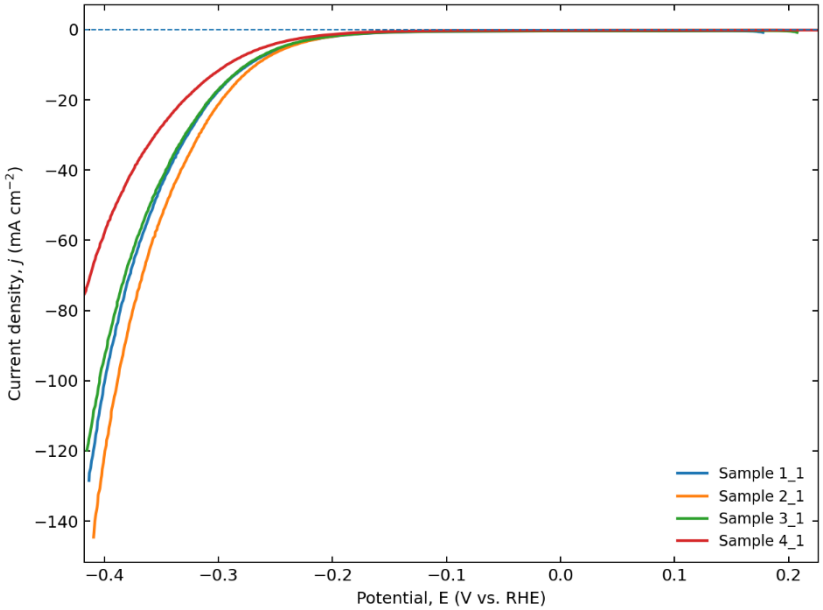


Figure 28. Linear sweep voltammograms corresponding to Cycle 8 for Ni/MoS_2-coated Samples 1_1, 2_1, 3_1, and 4_1 recorded in 1 M NaOH at 25 °C with a scan rate of 2 mV s^{-1}. Potentials are reported versus the reversible hydrogen electrode (RHE), and current densities are normalized to the geometric electrode area of 4 cm^2.

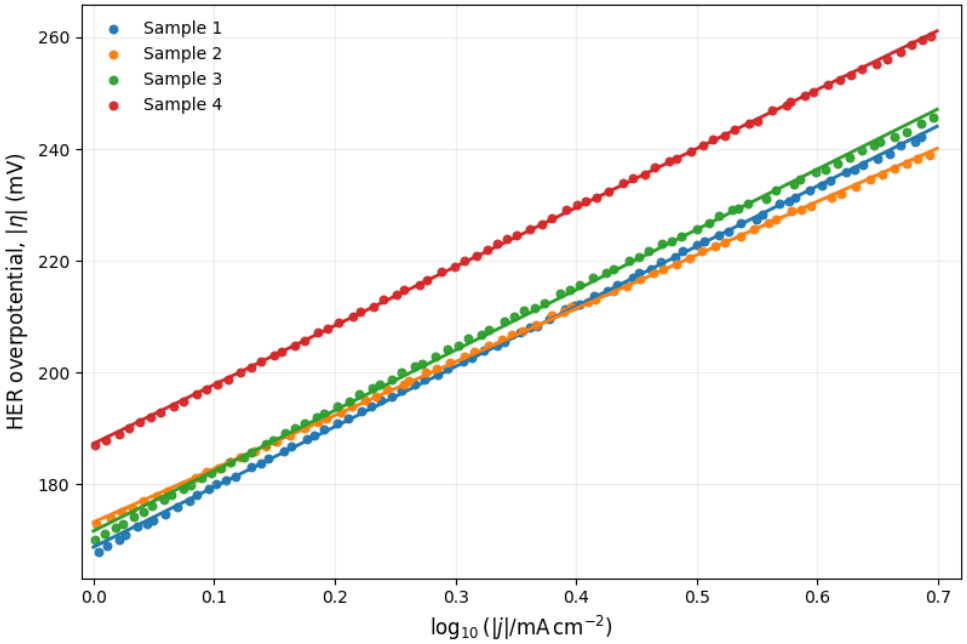


Figure 29. Tafel plots derived from the eighth-cycle polarization curves of Ni/MoS_2-coated Samples 1_1, 2_1, 3_1, and 4_1 recorded in 1 M NaOH at 25 °C. Current densities were normalized to the geometric electrode area of 4 cm^2, and potentials were converted from saturated Ag/AgCl to the reversible hydrogen electrode (RHE) scale. Solid lines represent linear regressions over the current-density interval of 1–5 mA cm^{-2}.

Table 11. HER kinetic parameters and overpotentials of Ni/MoS_2 composite coatings derived from the eighth-cycle polarization curves in 1 M NaOH at 25 °C.

Sample	Tafel intercept, a (V)	Tafel slope, $\|b\|$ (mV dec^{-1})	R^2	Apparent j_0 (A cm^{-2})	95% CI for j_0 (mA cm^{-2})	η_1 (mV)	η_5 (mV)	η_{10} (mV)	η_{10} determination
Sample 1_1	0.1688	107.7	0.99964	2.762 × 10^{-5}	0.02710–0.02816	166.5	242.3	273.8	Direct interpolation
Sample 2_1	0.1732	**95.7**	0.99978	1.579 × 10^{-5}	0.01551–0.01608	171.9	**238.6**	**266.9**	Direct interpolation
Sample 3_1	0.1717	107.9	0.99904	2.616 × 10^{-5}	0.02534–0.02700	169.0	245.1	275.3	Direct interpolation
Sample 4_1	0.1873	105.7	**0.99985**	1.719 × 10^{-5}	0.01696–0.01744	186.0	259.9	292.7	Direct interpolation

1.3.2 Series 2, deposition temperature 40 °C

The eighth-cycle polarization curves and Tafel plots for Series 2 are presented in Figures 30-35, with the derived kinetic parameters and operating overpotentials

summarized in Table 13 (electrodeposition conditions for each sample are summarized in Table 12).

Table 12. Electrodeposition conditions for Ni/MoS_2 coatings prepared from the DES-based electrolyte.

Sample	**Temperature during coating deposition, t / °C**	**Deposition current density, j / mA/cm^2**
1_2	40	5
2_2		10
3_2		15
4_2		20

Series 2 exhibited greater variation in HER performance than Series 1, demonstrating a stronger sensitivity to electrodeposition current density. The Tafel slopes ranged from **95.7 to 130.8 mV dec^{-1}**, while η_1 varied substantially from **162.8 to 213.6 mV**.

The most favorable low-current response was observed for **Sample 3_2**, deposited at 15 mA cm^{-2}, which exhibited η_1 = **162.8 mV**, η_5 = **248.3 mV**, and η_{10} = **278.6 mV**. Sample 2_2 also showed relatively low η_1 (**167.9 mV**) and a comparatively high apparent exchange current density, although its higher Tafel slope indicates a different polarization dependence.

In contrast, Sample 4_2, prepared at 20 mA cm^{-2}, showed the highest characteristic overpotentials of the series, reaching η_1 = **213.6 mV**, η_5 = **281.1 mV**, and η_{10} = **310.1 mV**. Interestingly, this sample simultaneously exhibited the lowest Tafel slope of the series (**95.7 mV dec^{-1}**). This illustrates why Tafel slope alone should not be used to rank HER activity: a favorable slope does not necessarily correspond to the lowest absolute operating overpotential.

Series 2 therefore indicates that deposition at intermediate current densities, particularly around 10–15 mA cm^{-2}, is preferable to the highest investigated current density for achieving favorable Ni/MoS_2 HER performance.

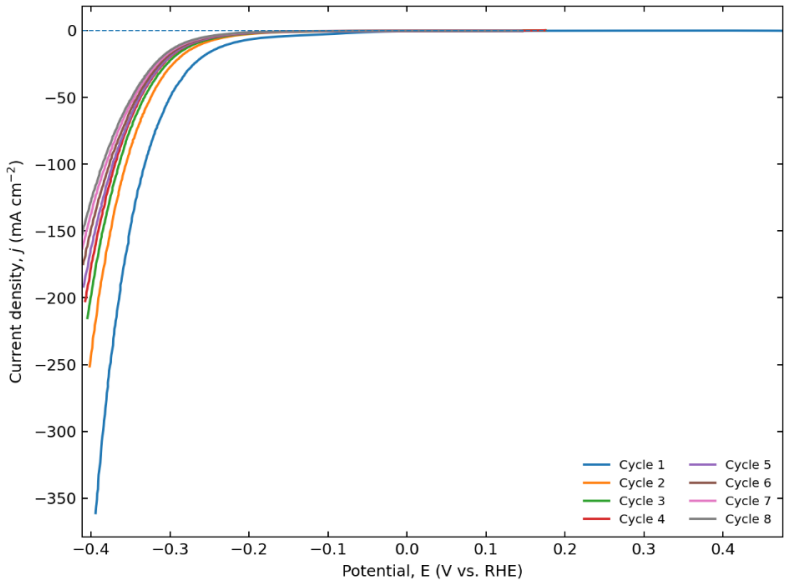


Figure 30. Linear sweep voltammograms of Ni/MoS_2-coated Sample 1_2 recorded during eight consecutive cycles in 1 M NaOH at 25 °C with a scan rate of 2 mV s^{-1}. Potentials are reported versus the reversible hydrogen electrode (RHE), and current densities are normalized to the geometric electrode area of 4 cm^2. A saturated Ag/AgCl electrode was used as the reference electrode.

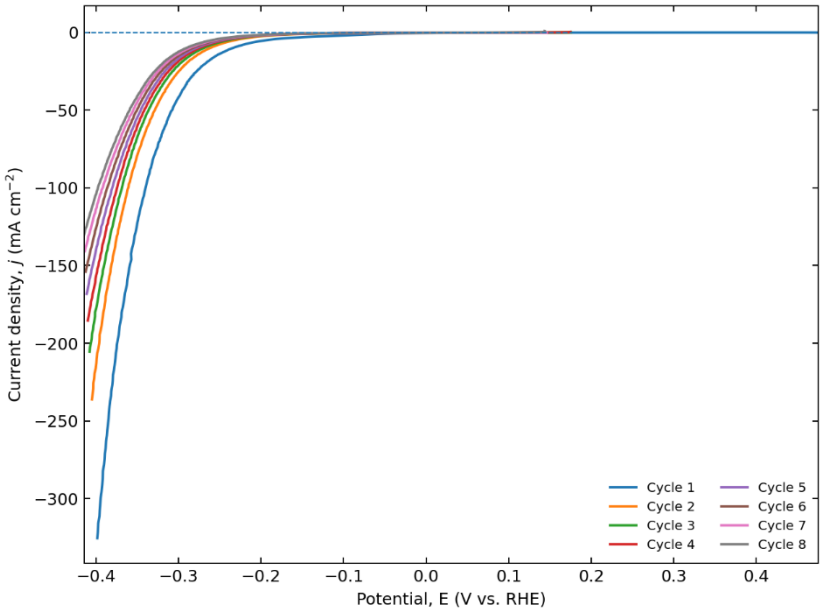


Figure 31. Linear sweep voltammograms of Ni/MoS_2-coated Sample 2_2 recorded during eight consecutive cycles in 1 M NaOH at 25 °C with a scan rate of 2 mV s^{-1}.

Potentials are reported versus the reversible hydrogen electrode (RHE), and current densities are normalized to the geometric electrode area of 4 cm². A saturated Ag/AgCl electrode was used as the reference electrode.

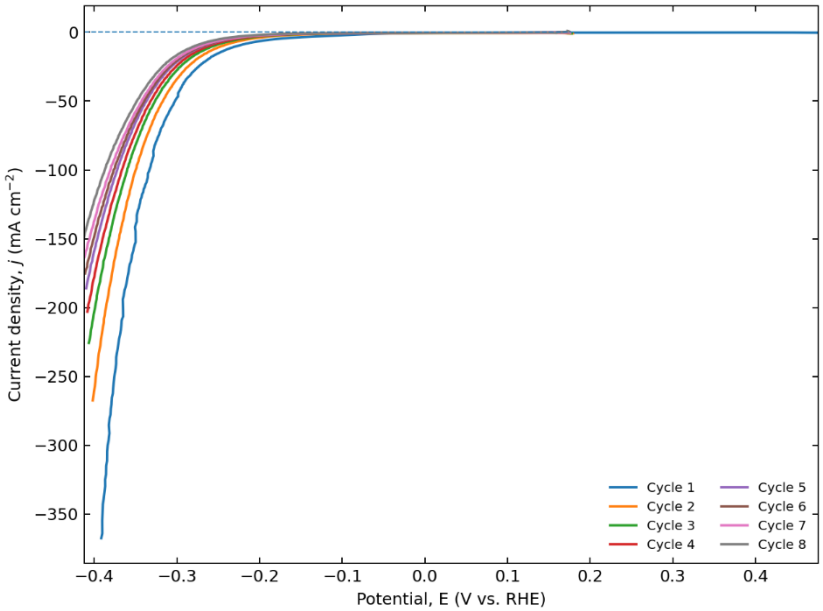


Figure 32. Linear sweep voltammograms of Ni/MoS_2-coated Sample 3_2 recorded during eight consecutive cycles in 1 M NaOH at 25 °C with a scan rate of 2 mV s^{-1}. Potentials are reported versus the reversible hydrogen electrode (RHE), and current densities are normalized to the geometric electrode area of 4 cm². A saturated Ag/AgCl electrode was used as the reference electrode.

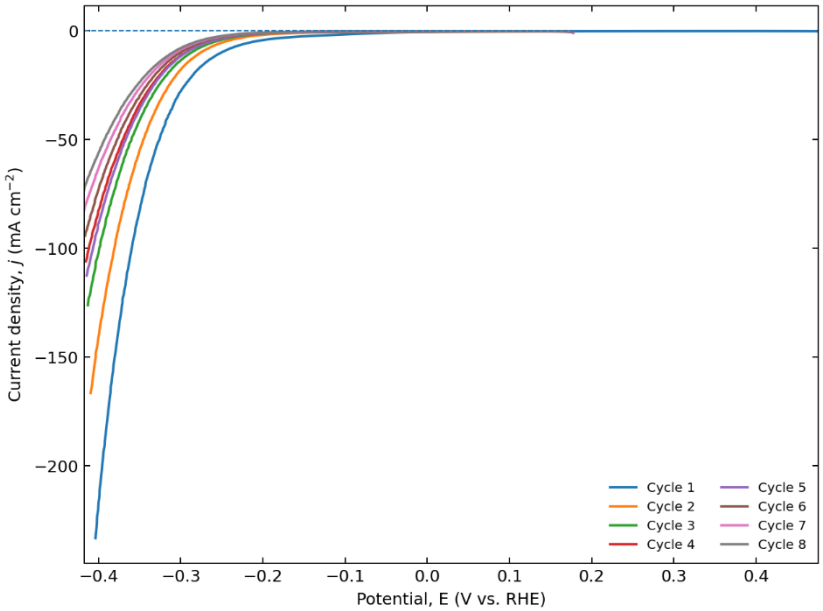


Figure 33. Linear sweep voltammograms of Ni/MoS_2-coated Sample 4_2 recorded during eight consecutive cycles in 1 M NaOH at 25 °C with a scan rate of 2 mV s^{-1}.

Potentials are reported versus the reversible hydrogen electrode (RHE), and current densities are normalized to the geometric electrode area of 4 cm². A saturated Ag/AgCl electrode was used as the reference electrode.

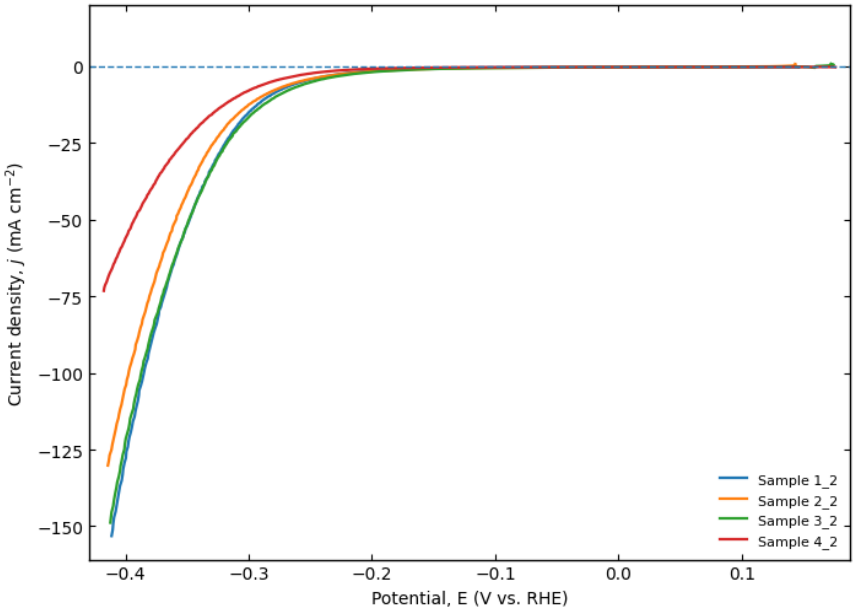


Figure 34. Linear sweep voltammograms corresponding to Cycle 8 for Ni/MoS_2-coated Samples 1_2, 2_2, 3_2, and 4_2 recorded in 1 M NaOH at 25 °C with a scan rate of 2 mV s^{-1}. Potentials are reported versus the reversible hydrogen electrode (RHE), and current densities are normalized to the geometric electrode area of 4 cm². A saturated Ag/AgCl electrode was used as the reference electrode.

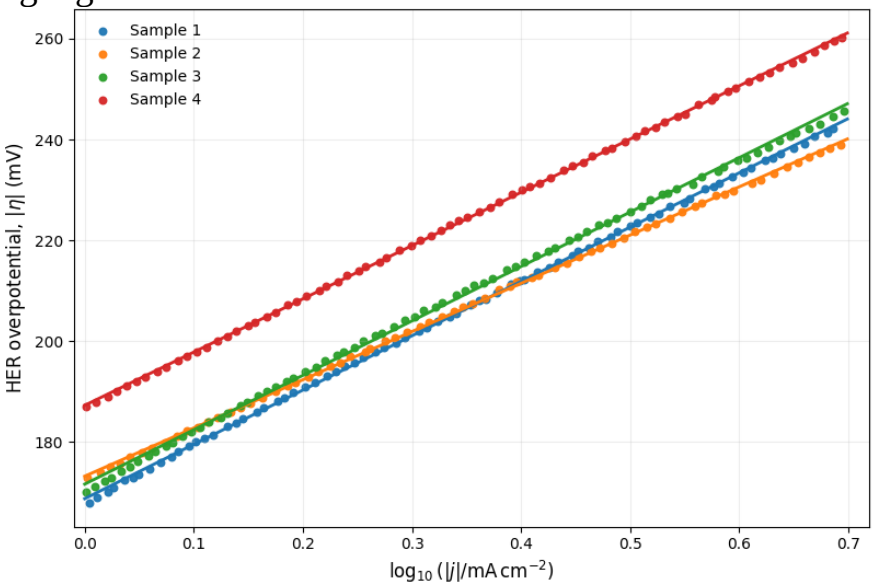


Figure 35. Tafel plots derived from the eighth-cycle polarization curves of Ni/MoS_2-coated Samples 1_2, 2_2, 3_2, and 4_2 recorded in 1 M NaOH at 25 °C. Current densities were normalized to the geometric electrode area of 4 cm², and potentials

were converted from saturated Ag/AgCl to the reversible hydrogen electrode (RHE) scale. Solid lines represent linear regressions over the current-density interval of 1–5 mA cm^{-2}.

Table 13. HER kinetic parameters and characteristic overpotentials derived from the eighth-cycle polarization curves of Ni/MoS_2 composite coatings in 1 M NaOH at 25 °C.

Sample	Tafel intercept, a (V)	Tafel slope, $\|b\|$ (mV dec^{-1})	R^2	Apparent j_0 (A cm^{-2})	95% CI for j_0 (mA cm^{-2})	η_1 (mV)	η_5 (mV)	η_{10} (mV)	η_{10} determination
Sample 1_2	0.1849	105.0	0.99957	1.769×10^{-5}	0.01728–0.01811	183.1	256.3	284.7	Direct interpolation
Sample 2_2	0.1722	130.8	0.99661	**4.896×10^{-5}**	0.04675–0.05128	167.9	259.5	290.3	Direct interpolation
Sample 3_2	0.1669	121.6	0.99701	4.302×10^{-5}	0.04106–0.04507	**162.8**	**248.3**	**278.6**	Direct interpolation
Sample 4_2	0.2157	**95.7**	0.99959	5.706×10^{-6}	0.00554–0.00588	213.6	281.1	310.1	Direct interpolation

1.3.3 Series 3, deposition temperature 40 ºC

The evolution of the polarization response, the Cycle 8 LSV comparison, and the corresponding Tafel analysis for Series 3 are illustrated in Figures 36-42, while the quantitative HER parameters are summarized in Table 15 (electrodeposition conditions for each sample are summarized in Table 14).

Series 3 produced the most favorable low-overpotential Ni/MoS_2 coating among the three investigated series. In particular, **Sample 5_3** exhibited η_1 = **134.4 mV**, η_5 = **225.6 mV**, and η_{10} = **259.1 mV**, representing the lowest characteristic overpotentials observed within the Ni/MoS_2 dataset. It also showed the highest apparent exchange current density, **8.80×10^{-5} A cm^{-2}**.

The other Series 3 coatings displayed η_1 values between **150.8 and 165.8 mV** over the 5–20 mA cm^{-2} deposition-current range, confirming generally favorable low-current HER activity. However, their Tafel slopes were comparatively higher, ranging from **113.5 to 141.3 mV dec^{-1}**. This again demonstrates that improved absolute HER activity in these coatings is expressed predominantly as a shift of the

polarization response toward lower operating overpotentials rather than as a systematic decrease in Tafel slope.

Sample 5_3 is particularly important because its strong performance indicates that the deposition conditions used for this coating generated a Ni/MoS_2 composite with a favorable HER response over the entire evaluated current-density range. The combination of the lowest η_1, η_5, and η_{10} and the largest apparent j_0 identifies this coating as the **best overall Ni/MoS_2 electrode investigated in Section 1.3**.

Taken together, the Series 3 results strengthen the conclusion that MoS_2-containing Ni composites can achieve substantially reduced HER operating overpotentials when suitable electrodeposition conditions are selected. The comparison of the three series therefore suggests that the beneficial contribution of MoS_2 is not independent of processing conditions; rather, the catalytic performance emerges from the combined effects of composite formation and electrodeposition parameters.

Table 14. Electrodeposition conditions for Ni/MoS_2 coatings prepared from the DES-based electrolyte.

Sample	**Temperature during coating deposition, t / ºC**	**Deposition current density, j / mA/cm^2**
1_3	40	5
2_3		10
3_3		15
4_3		20
5_3		25

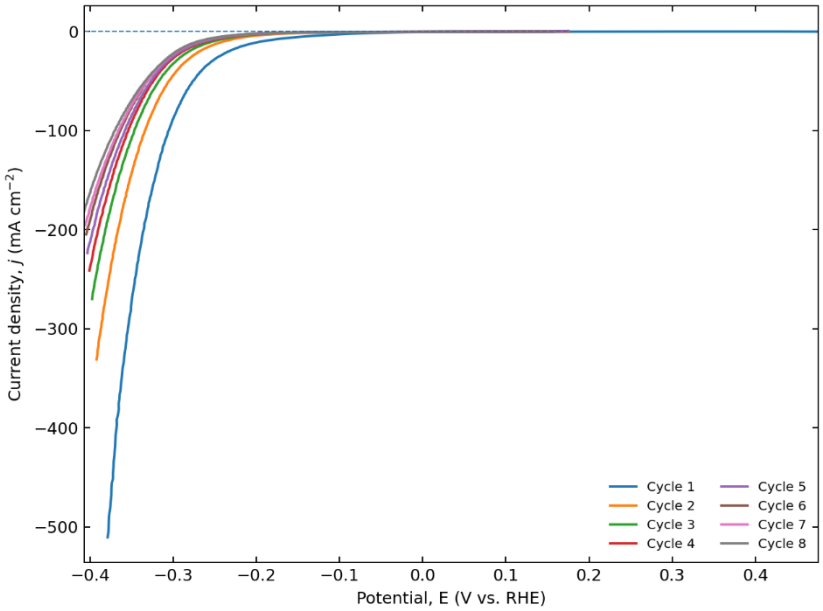


Figure 36. Linear sweep voltammograms of Ni/MoS_2-coated Sample 1_3 recorded during eight consecutive cycles in 1 M NaOH at 25 °C with a scan rate of 2 mV s^{-1}. Potentials are reported versus the reversible hydrogen electrode (RHE), and current densities are normalized to the geometric electrode area of 4 cm^2. A saturated Ag/AgCl electrode was used as the reference electrode.

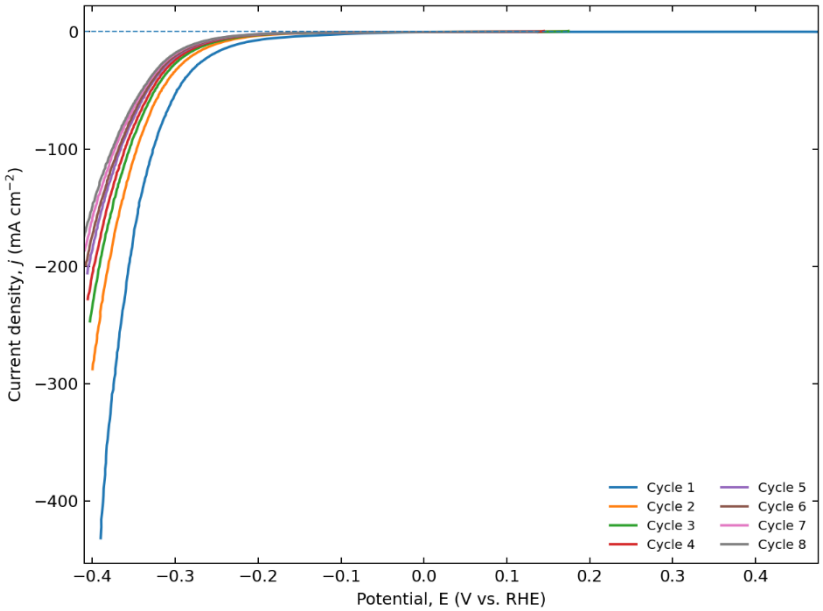


Figure 37. Linear sweep voltammograms of Ni/MoS_2-coated Sample 2_3 recorded during eight consecutive cycles in 1 M NaOH at 25 °C with a scan rate of 2 mV s^{-1}. Potentials are reported versus the reversible hydrogen electrode (RHE), and current densities are normalized to the geometric electrode area of 4 cm^2. A saturated Ag/AgCl electrode was used as the reference electrode.

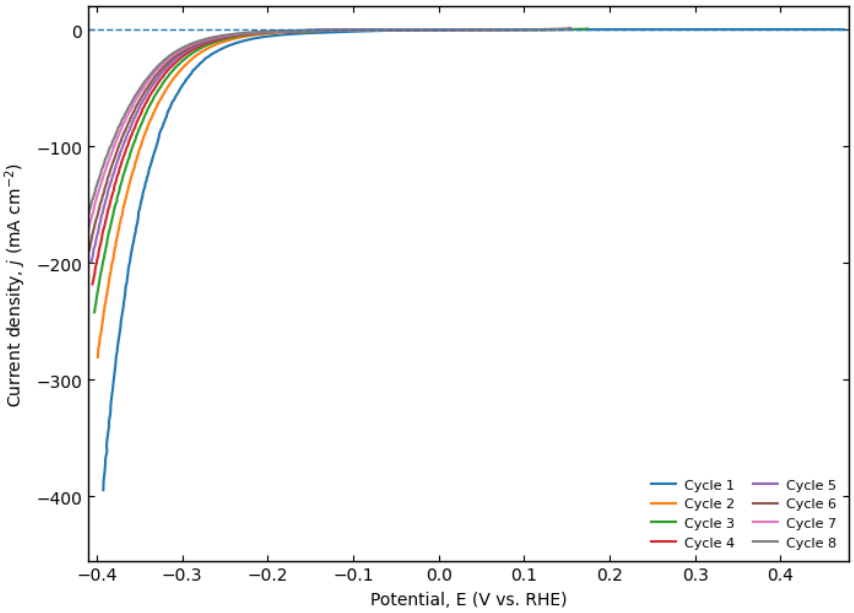


Figure 38. Linear sweep voltammograms of Ni/MoS_2-coated Sample 3_3 recorded during eight consecutive cycles in 1 M NaOH at 25 °C with a scan rate of 2 mV s^{-1}. Potentials are reported versus the reversible hydrogen electrode (RHE), and current densities are normalized to the geometric electrode area of 4 cm^2. A saturated Ag/AgCl electrode was used as the reference electrode.

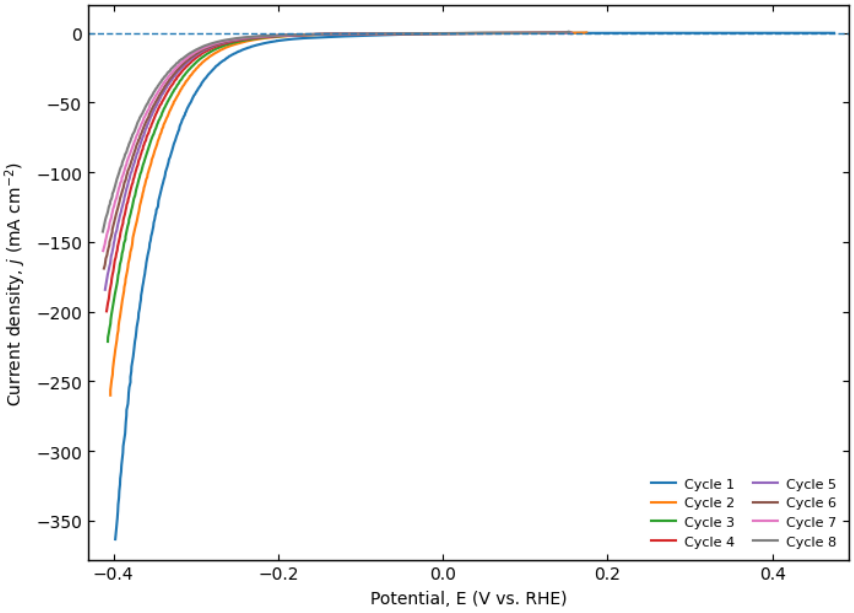


Figure 39. Linear sweep voltammograms of Ni/MoS_2-coated Sample 4_3 recorded during eight consecutive cycles in 1 M NaOH at 25 °C with a scan rate of 2 mV s^{-1}. Potentials are reported versus the reversible hydrogen electrode (RHE), and current densities are normalized to the geometric electrode area of 4 cm^2. A saturated Ag/AgCl electrode was used as the reference electrode.

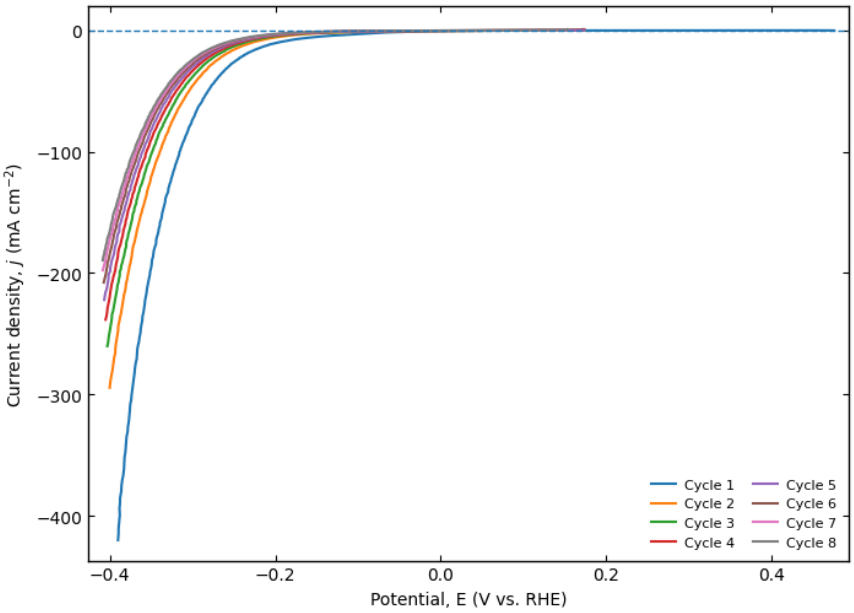


Figure 40. Linear sweep voltammograms of Ni/MoS_2-coated Sample 5_3 recorded during eight consecutive cycles in 1 M NaOH at 25 °C with a scan rate of 2 mV s^{-1}. Potentials are reported versus the reversible hydrogen electrode (RHE), and current densities are normalized to the geometric electrode area of 4 cm^2.

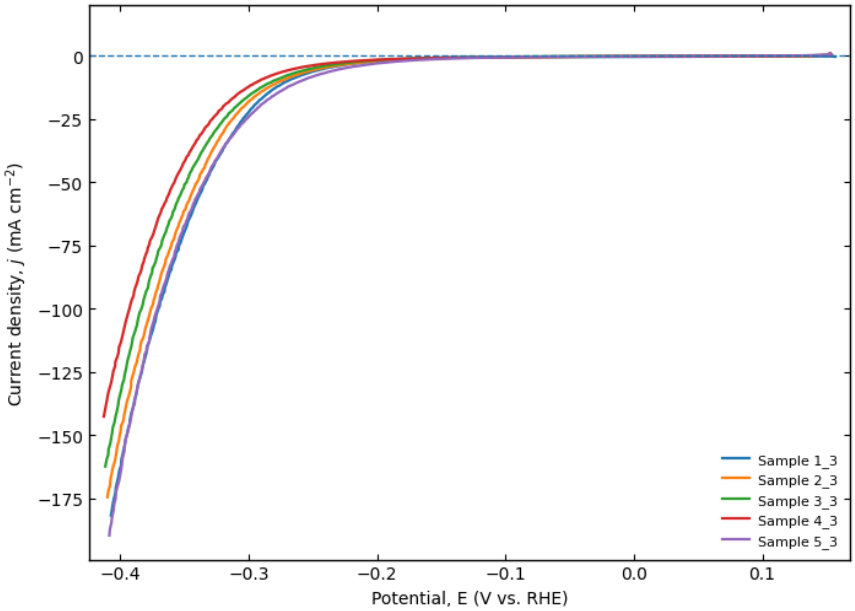


Figure 41. Linear sweep voltammograms corresponding to Cycle 8 for Ni/MoS_2-coated Samples 1_3, 2_3, 3_3, 4_3 and 5_3 recorded in 1 M NaOH at 25 °C with a scan rate of 2 mV s^{-1}. Potentials are reported versus the reversible hydrogen electrode (RHE), and current densities are normalized to the geometric electrode area of 4 cm^2. A saturated Ag/AgCl electrode was used as the reference electrode.

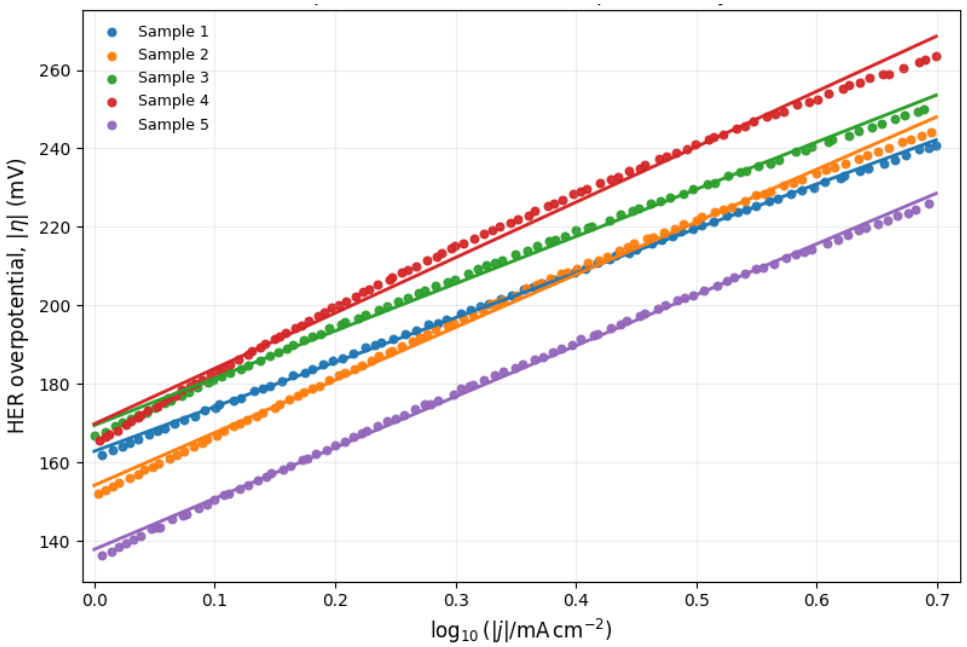


Figure 42. Tafel plots derived from the eighth-cycle polarization curves of Ni/MoS_2-coated Samples 1_3, 2_3, 3_3, 4_3 and 5_3 recorded in 1 M NaOH at 25 °C. Current densities were normalized to the geometric electrode area of 4 cm^2, and potentials were converted from saturated Ag/AgCl to the reversible hydrogen electrode (RHE) scale. Solid lines represent linear regressions over the current-density interval of 1–5 mA cm^{-2}.

Table. 15. HER kinetic parameters and characteristic overpotentials derived from the eighth-cycle polarization curves of Ni/MoS_2 composite coatings in 1 M NaOH at 25 °C.

Sample	**Tafel intercept, *a* (V)**	**Tafel slope, |*b*| (mV dec^{-1})**	**R^2**	**Apparent j_0 (A cm^{-2})**	**95% CI for j_0 (mA cm^{-2})**	**η_1 (mV)**	**η_5 (mV)**	**η_{10} (mV)**	**η_{10} determination**
Sample 1_3	0.1628	113.5	0.9992	3.74×10^{-5}	0.0364–0.0384	160.1	240.1	269.8	Interpolated from polarization curve
Sample 2_3	0.1541	134.2	0.9972	7.21×10^{-5}	0.0695–0.0749	150.8	243.6	274.9	Interpolated from polarization curve
Sample 3_3	0.1694	120.4	0.9974	3.98×10^{-5}	0.0380–0.0416	165.8	250.5	280.8	Interpolated from polarization curve
Sample 4_3	0.1698	141.3	0.9934	6.37×10^{-5}	0.0601–0.0675	163.9	262.8	292.1	Interpolated from polarization curve

Sample 5_3	0.1378	129.8	0.9985	8.80×10^{-5}	0.0857–0.0903	134.4	225.6	259.1	Interpolated from polarization curve

1.3.4 Comparative Analysis of HER Performance of Ni/MoS_2 Composite Coatings

To identify the most favorable electrodeposition conditions and distinguish systematic trends from series-to-series variation, the HER performance of the three Ni/MoS_2 coating series was compared at **identical electrodeposition current densities of 5, 10, 15, and 20 mA cm^{-2}**. This matched-condition approach enables a more meaningful comparison because coatings prepared at the same current density are evaluated directly across the three experimental series. Sample 5_3, prepared at 25 mA cm^{-2}, was not included in the matched statistical comparison because no equivalent deposition condition was investigated in Series 1 or Series 2.

The mean HER kinetic parameters and characteristic overpotentials obtained by grouping coatings prepared at the same electrodeposition current density are summarized in Table 16, providing an overview of the influence of deposition current density on the reproducibility and catalytic performance of the Ni/MoS_2 coatings.

Table 16. Comparison of HER performance of Ni/MoS_2 coatings from Series 1–3 prepared at identical electrodeposition current densities.

Deposition current (mA cm^{-2})	Series / Sample	Tafel slope (mV dec^{-1})	Apparent j_0 (A cm^{-2})	η_1 (mV)	η_5 (mV)	η_{10} (mV)
5	Series 1 — 1_1	107.7	2.762×10^{-5}	166.5	242.3	273.8
	Series 2 — 1_2	**105.0**	1.769×10^{-5}	183.1	256.3	284.7
	Series 3 — 1_3	113.5	**3.740×10^{-5}**	**160.1**	**240.1**	**269.8**

10	**Series 1 — 2_1**	**95.7**	1.579×10^{-5}	171.9	**238.6**	**266.9**
	Series 2 — 2_2	130.8	4.896×10^{-5}	167.9	259.5	290.3
	Series 3 — 2_3	134.2	$\mathbf{7.210 \times 10^{-5}}$	**150.8**	243.6	274.9
15	**Series 1 — 3_1**	**107.9**	2.616×10^{-5}	169.0	**245.1**	**275.3**
	Series 2 — 3_2	121.6	$\mathbf{4.302 \times 10^{-5}}$	**162.8**	248.3	278.6
	Series 3 — 3_3	120.4	3.980×10^{-5}	165.8	250.5	280.8
20	Series 1 — 4_1	105.7	1.719×10^{-5}	186.0	**259.9**	292.7
	Series 2 — 4_2	**95.7**	5.706×10^{-6}	213.6	281.1	310.1
	Series 3 — 4_3	141.3	$\mathbf{6.370 \times 10^{-5}}$	**163.9**	262.8	**292.1**

Table 17. Mean HER parameters at identical electrodeposition current densities.

Electrodeposition current density (mA cm^{-2})	n	Mean Tafel slope (mV dec^{-1})	Mean apparent j_0 (A cm^{-2})	Mean η_1 (mV)	Mean η_5 (mV)	Mean η_{10} (mV)
5	3	108.7 ± 4.3	$(2.76 \pm 1.00) \times 10^{-5}$	169.9 ± 11.9	**246.2 ± 8.8**	**276.1 ± 7.7**
10	3	120.2 ± 21.3	$\mathbf{(4.56 \pm 2.83) \times 10^{-5}}$	**163.5 ± 11.2**	247.2 ± 10.9	277.4 ± 11.9
15	3	116.6 ± 7.6	$(3.63 \pm 0.88) \times 10^{-5}$	165.9 ± 3.1	248.0 ± 2.7	278.2 ± 2.8
20	3	114.2 ± 24.0	$(2.89 \pm 3.07) \times 10^{-5}$	187.8 ± 24.9	267.9 ± 11.5	298.3 ± 10.2

The comparison indicates that the most favorable average HER response was generally obtained for coatings deposited within the **5–15 mA cm^{-2} range**, whereas increasing the electrodeposition current density to 20 mA cm^{-2} did not result in further improvement. At 5 mA cm^{-2}, the mean η_5 and η_{10} values were **246.2 ± 8.8 and 276.1 ± 7.7 mV**, respectively, representing the lowest average values at these operating current densities. At 10 mA cm^{-2}, the coatings exhibited

the lowest mean η_1 (**163.5 ± 11.2 mV**) and the highest mean apparent exchange current density (**4.56×10^{-5} A cm^{-2}**), indicating favorable HER activity at relatively low polarization.

The coatings deposited at **15 mA cm^{-2}** were particularly notable for their consistency across the three series. Although their mean overpotentials were not the lowest in every category, the between-series variation was small, with η_1, η_5, and η_{10} of **165.9 ± 3.1, 248.0 ± 2.7, and 278.2 ± 2.8 mV**, respectively. This suggests that 15 mA cm^{-2} represents a comparatively robust electrodeposition condition for obtaining reproducible Ni/MoS_2 HER performance.

In contrast, deposition at **20 mA cm^{-2}** resulted in the highest mean operating overpotentials and substantially greater between-series variability. The mean η_1, η_5, and η_{10} increased to **187.8 ± 24.9, 267.9 ± 11.5, and 298.3 ± 10.2 mV**, respectively. Therefore, increasing the deposition current density beyond the intermediate range does not appear to provide a systematic improvement in HER activity.

The comparison between individual series further demonstrates that no single kinetic parameter is sufficient to describe the performance of the composite coatings. Series 3 generally exhibited lower low-current overpotentials and higher apparent exchange current densities, whereas Series 1 frequently showed lower Tafel slopes and favorable η_5 and η_{10} values. The lack of a direct correspondence between Tafel slope and operating overpotential indicates that the catalytic behavior should be assessed using several complementary descriptors rather than ranking the coatings solely according to their Tafel slopes.

Among all Ni/MoS_2 coatings investigated, **Sample 5_3 exhibited the strongest overall HER performance**, with η_1, η_5, and η_{10} values of **134.4, 225.6, and 259.1 mV**, respectively, together with an apparent j_0 of **8.80×10^{-5} A cm^{-2}**. Although this sample was prepared at 25 mA cm^{-2} and therefore could not be included in the matched-condition comparison, its performance demonstrates that suitable

electrodeposition conditions can produce a substantial improvement in the catalytic response of the Ni/MoS_2 composite.

The comparative analysis shows that the HER activity of the Ni/MoS_2 coatings is governed by the combined influence of **composite formation and electrodeposition conditions**. The results identify the intermediate deposition-current region as particularly favorable for obtaining reproducible HER activity, while the exceptional performance of Sample 5_3 demonstrates that further optimization of the Ni/MoS_2 deposition process can shift the polarization response toward substantially lower operating overpotentials. These findings support the beneficial contribution of MoS_2 to the Ni-based composite electrode while emphasizing that its catalytic advantage depends strongly on the conditions used to form the coating.

1.3.5 Effect of MoS_2 incorporation on HER performance

The electrochemical results indicate that incorporation of MoS_2 into the electrodeposited Ni matrix can enhance the hydrogen-evolution performance relative to pure Ni coatings prepared under several of the investigated conditions. The most active Ni/MoS_2 composite, Sample 5_3, required overpotentials of only 134.4, 225.6, and 259.1 mV to reach 1, 5, and 10 mA cm^{-2}, respectively. These values are markedly lower than those of a number of pure Ni coatings. For example, compared with Ni Sample 13_2, which required 203, 254, and 278 mV at the same current densities, the Ni/MoS_2 composite reduced η_1, η_5, and η_{10} by 68.6, 28.4, and 18.9 mV, respectively.

The improvement is particularly evident in the absolute polarization required to sustain HER. Although the Tafel slope of Ni/MoS_2 Sample 5_3 is higher than that of some optimized pure Ni coatings, its polarization curve is shifted toward lower overpotential over the experimentally relevant current-density range. This indicates

that the beneficial effect of MoS_2 is expressed primarily through a reduction in the operating overpotential rather than through a universal decrease in Tafel slope. The Section 1.3 data show that Ni/MoS_2 Sample 5_3 exhibits η_1 = 134.4 mV, η_5 = 225.6 mV and η_{10} = 259.1 mV.

A plausible interpretation is that the Ni/MoS_2 composite provides a more favorable catalytic interface than Ni alone, potentially through the presence of additional HER-active sites and cooperative interactions between the Ni matrix and MoS_2 phase. The electrochemical results themselves demonstrate the performance improvement, although identification of the precise physicochemical origin would require correlation with the structural and surface characterization described elsewhere in the project. The report already notes that differences in coating morphology, roughness, porosity, surface composition, and electrochemically accessible surface area can strongly influence HER response.

Overall, the data support the conclusion that MoS_2 incorporation can improve the HER activity of electrodeposited Ni coatings by lowering the overpotential required to achieve a given current density. The magnitude of this benefit depends on the deposition conditions, showing that both composite formulation and electrodeposition parameters must be optimized together. While the best optimized pure Ni coating can still outperform the best Ni/MoS_2 sample for some operating overpotentials, the composite coatings demonstrate that incorporation of MoS_2 is an effective route for enhancing HER performance relative to non-optimized and moderately performing Ni deposits.

1.4 Electrochemical characterization of C-MoFeNiP materials synthesized at different pyrolysis temperatures

The electrocatalytic performance of C-MoFeNiP materials synthesized at different pyrolysis temperatures was systematically studied for HER in both alkaline and acidic media. In alkaline conditions, HER activity increased with higher pyrolysis temperatures, with C-MoFeNiP-1200 showing the best performance (η_{10} = 321 mV). In acidic media, the optimal catalyst was C-MoFeNiP-1000 (η_{10} = 228 mV), highlighting that the ideal pyrolysis temperature depends on the electrolyte, in agreement with previous studies. Kinetic analysis revealed that the most active catalysts also exhibited favorable reaction parameters, including the lowest Tafel slopes, highest charge transfer coefficients, and smallest charge transfer resistances, indicating efficient electron transfer at the catalyst–electrolyte interface. Tafel slopes decreased with increasing pyrolysis temperature from ~120 mV dec^{-1} to 93 mV dec^{-1} for C-MoFeNiP-1200 in alkaline media, and to 98 mV dec^{-1} for C-MoFeNiP-1000 in acidic media, suggesting enhanced Volmer step kinetics and improved overall HER activity. Electrochemical impedance spectroscopy (EIS) provided further insight into charge-transfer behavior. Nyquist plots, fitted with an equivalent circuit consisting of solution resistance (Rs), charge transfer resistance

(Rct), and a constant phase element (CPE), showed similar Rs values (4–5 Ω) for all catalysts in both alkaline and acidic media. All measurements and parameters are summarized in Figures 43, 44 and Tables 18 and 19.

In alkaline media, the reaction mechanism likely involves OH^- generation and the formation of oxide/hydroxide intermediates. Detailed steps of the mechanism are outlined below for clarity.

HER in alkaline electrolyte:

MoFeNiP + H2O + e− → MoFeNiPH* + OH− discharge Volmer reaction

MoFeNiP + OH− → MoFeNi–O(OH)/OH + P {surface or dissolution}

Either

MoFeNiPH* + H2O + e− → MoFeNiP + H2 + OH− desorption Heyrovsky reaction

or

MoFeNiPH* + MoFeNiPH* → 2MoFeNiP +H2 recombination Tafel reaction

HER in acidic:

MoFeNiP + H+ + e− → MoFeNiPH* discharge Volmer reaction

either

MoFeNiPH* + H+ + e− → MoFeNiP + H2 desorption Heyrovsky reaction

or

MoFeNiPH* + MoFeNiPH* → 2MoFeNiP +H2 recombination Tafel reaction

During the Volmer step, the generation of OH^- ions near the electrode surface locally increases the pH, which promotes surface hydroxylation or oxidation. This can lead to the formation of a thin (oxy)hydroxide layer, such as $Ni(OH)_2$, FeOOH, or MoO, while part of the phosphide phase may dissolve into the electrolyte. Such surface reconstruction can contribute to minor activation effects or stabilization during continuous operation. These processes help explain the distinct stability behavior observed in 1 M KOH compared with acidic media, where hydroxide formation does not occur and the catalyst generally requires more time to reach a steady state during HER.

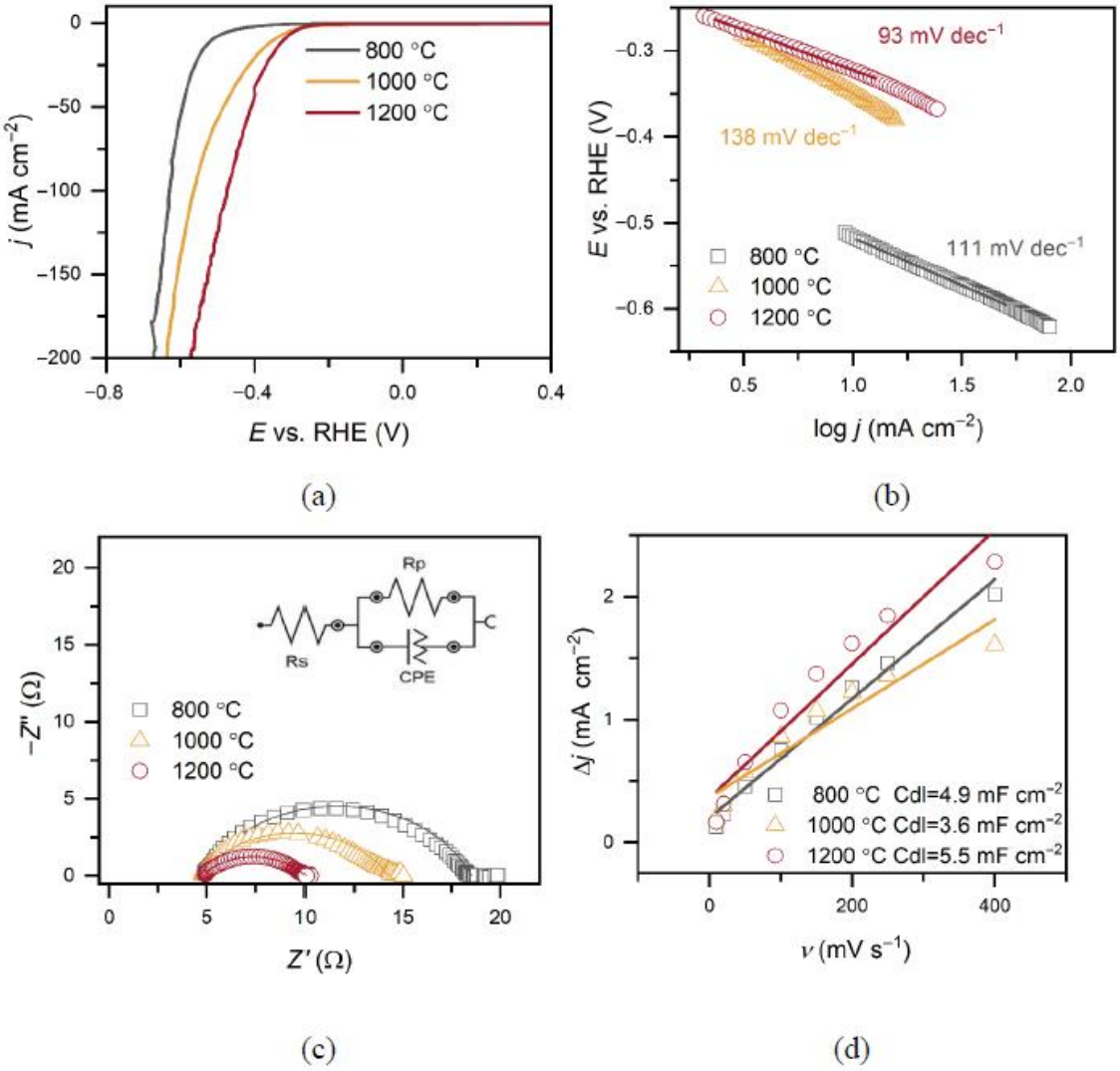


Figure 43. (a) LSV curves of C-MoFeNiP catalysts treated at different temperatures, measured in 1 M KOH (scan rate of 1 mV s^{-1} and rotation speed of 500 rpm); (b) corresponding Tafel plots; (c) Nyquist plots from EIS recorded in 1 M KOH at –485 mV with the inset showing the equivalent circuit; (d) capacitance current density vs. scan rate with C_{dl} values.

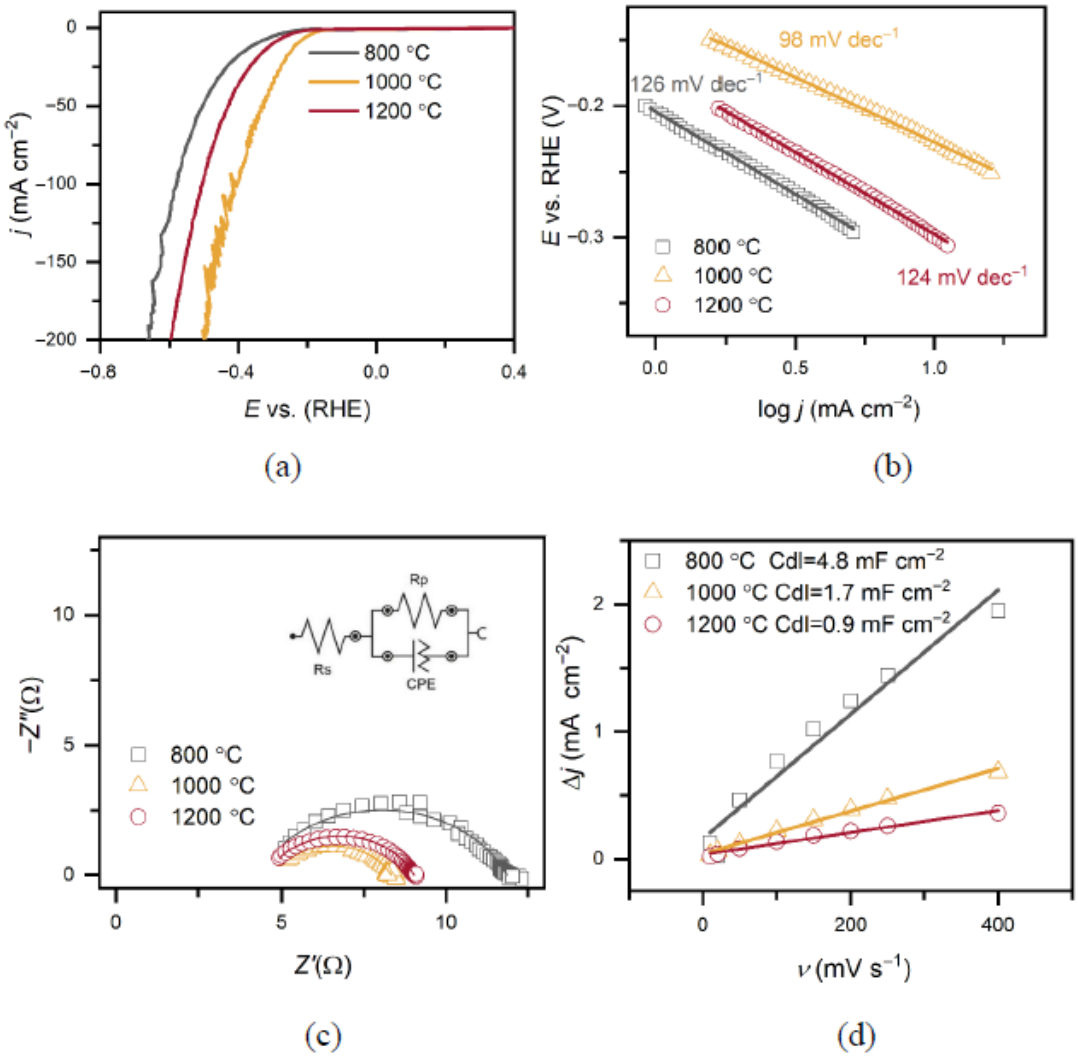


Figure 44. (a) LSV curves of C-MoFeNiP catalysts treated at different temperatures, measured in 0.5 M H_2SO_4 (scan rate of 1 mV s^{-1} and rotation speed of at 1000 rpm); (b) Corresponding Tafel plots; (c) Nyquist plots from EIS recorded in 0.5 M H_2SO_4 at −589 mV; (d) Capacitance current density vs. scan rate with C_{dl} values.

Table 18. Summary of electrochemical parameters measured in 1 M KOH for C-MoFeNiP catalysts treated at different temperatures.

	C-MoFeNiP-800	C-MoFeNiP-1000	C-MoFeNiP-1200
LSV analysis			
η10 (mV)	522	349	321
Tafel slop (mV dec^{-1})		138	93
j_0 (mA cm^{-2})	$2.2 \cdot 10^{-4}$	$2.8 \cdot 10^{-2}$	$3.4 \cdot 10^{-3}$
α	0.53	0.43	0.64
EIS analysis			
Y_0-CPE (mS·s^N)	0.19	0.54	2.2
Rct (Ω)	13.7	9.6	5.3
Rs (Ω)	4.8	4.7	4.7
N-CPE	0.742	0.670	0.562
Ceff (F)	$2.3 \cdot 10^{-5}$	$3.5 \cdot 10^{-5}$	$6.7 \cdot 10^{-5}$
χ^2	0.03	0.03	0.003
CV analysis			
Cdl (mF cm^{-2})	4.9	3.6	5.5

* η10 (mV)—Overpotential at 10 mA cm^{-2}, j_0—Exchange current density, α—Charge transfer coefficient, CPE—constant phase element, Y_0-CPE admittance, N—CPE exponent change, Rct—charge transfer resistance, Rs—Solution resistance, Ceff—Effective capacitance, χ^2—Chi-squared fitting, Cdl—Double-layer capacitance.

Table 19. Summary of electrochemical parameters measurements in 0.5 M H_2SO_4 for C-MoFeNiP catalysts treated at different temperatures.

Parameters	C-MoFeNiP-800	C-MoFeNiP-1000	C-MoFeNiP-1200
LSV analysis			
η10 (mV)	349	228	300
Tafel slop (mV dec^{-1})	126	98	124
j_0 (mA cm^{-2})	$2.4 \cdot 10^{-2}$	$4.8 \cdot 10^{-2}$	$4.0 \cdot 10^{-2}$
α	0.47	0.60	0.48
EIS analysis			
Y_0-CPE (mS·s^N)	0.030	0.080	0.054
Rct (Ω)	7.6	3.6	4.5
Rs (Ω)	4.2	4.8	4.5
N-CPE	0.741	0.715	0.746
Ceff (F)	$1.5 \cdot 10^{-6}$	$3.1 \cdot 10^{-6}$	$3.1 \cdot 10^{-6}$
χ^2	0.03	0.008	0.001
CV analysis			
Cdl (mF cm^{-2})	4.8	1.7	0.9

In alkaline media, Rct decreased with increasing pyrolysis temperature (13.7 Ω → 5.3 Ω for C-MoFeNiP-800 → -1200), indicating more efficient charge transfer for higher-temperature samples. In acidic media, Rct showed a different trend, with the lowest value for C-MoFeNiP-1000 (3.6 Ω), consistent with its superior HER activity. The CPE exponent (N-CPE) was nearly constant in acidic media but decreased in KOH with higher synthesis temperatures, likely due to surface reconstruction and oxy(hydroxide) formation, as commonly observed for TMP catalysts. Capacitance analysis showed that while C_{dl} from non-faradaic CV measurements did not correlate with HER activity, the effective capacitance (C_{eff}) from EIS under faradaic conditions did, reflecting the true active sites. This suggests that the carbon matrix mainly provides conductivity and stability, whereas HER activity originates from the metallic phosphide phases. Differences in HER performance are attributed to structural and compositional changes. XRD and EDX revealed that higher pyrolysis temperatures enhance crystallinity, interdiffusion, and mixing of metal species, while Raman spectra indicated minimal changes in carbon disorder. Morphology analysis showed notable alterations at 1200 °C, highlighting that catalytic activity is primarily governed by the crystalline phase and composition of the phosphides.

Stability tests of the best catalysts in each medium showed that C-MoFeNiP-1200 in alkaline media exhibited an initial current increase over 10 h, then stabilized, while C-MoFeNiP-1000 in acid maintained a stable current throughout (Figure 45). Post-stability EDX analysis revealed a decrease in the M/P ratio and increased oxygen content in alkaline media, indicating partial P dissolution and surface oxidation, whereas the M/P ratio remained almost unchanged in acidic media .

Lower current densities in acid may result from hydrogen bubble accumulation on the electrode, which can block active sites; this can be mitigated under pressurized electrolyzer conditions. SEM imaging showed overall structural

integrity, though high-resolution images revealed surface disruption: carbon matrix leaching in acid exposed phosphide particles, while alkaline conditions caused increased porosity (Figure 46).

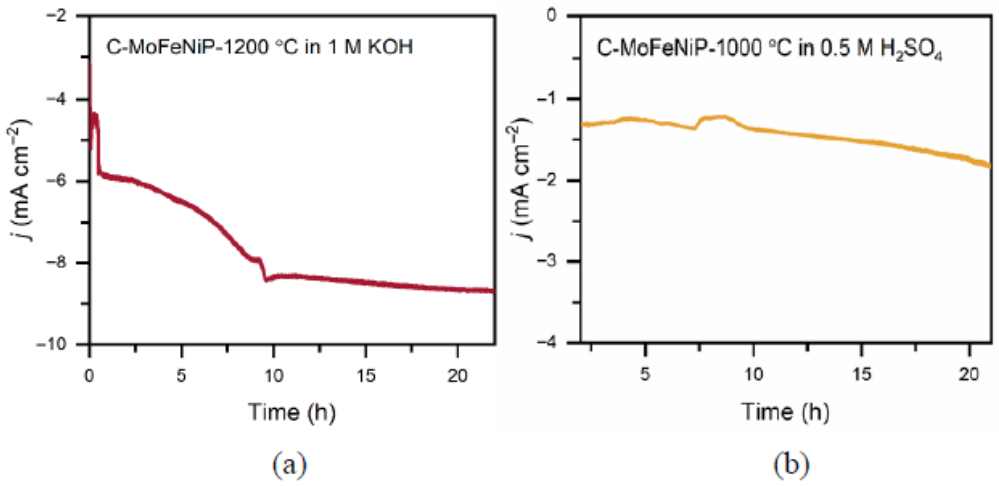


Figure 45. Chronopotentiometric stability measurement for C-MoFeNiP for 22 h (a) at −285 mV vs. RHE in an alkaline environment, and (b) at −229 mV vs. RHE in an acidic environment.

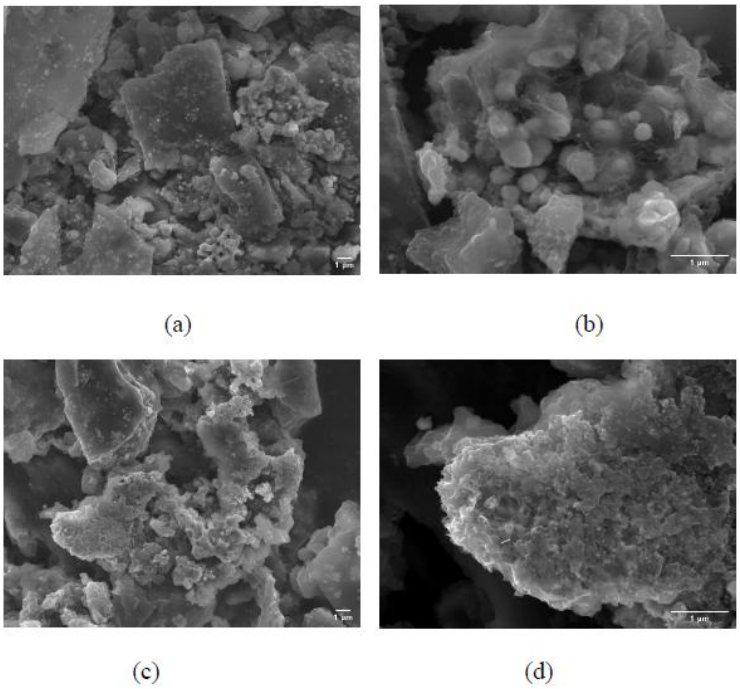


Figure 46. SEM images of C-MoFeNiP after a 22 h chronoamperometry stability test: (a,b) post-test morphology in an acidic environment; (c,d) post-test morphology in an alkaline environment.

Overall overview, the electrochemical analyses show that the HER performance of C-MoFeNiP catalysts is strongly influenced by pyrolysis temperature, which affects the crystalline phase and composition of the metal phosphides, Volmer step kinetics, and charge-transfer properties at the catalyst–electrolyte interface. As a multimetallic phosphide system, C-MoFeNiP exhibits distinct behavior in acidic and alkaline media due to differences in HER mechanisms, adsorption characteristics, and pH-dependent active site functionality.

For TMP-based catalysts, different behaviors in alkaline and acidic environments have been reported. In alkaline media, where HER is generally limited by water dissociation, phosphorus can dissolve, leaving the metal to form hydroxides or oxides. Mo oxides formed on MoFeNiP have been shown to enhance HER activity, although some reports suggest that the apparent activity increase arises from an enlarged ECSA, and per-ECSA activity may actually decrease. Detailed characterization before and after stability tests is needed to clarify these activation processes and optimize performance in alkaline media.

In acidic media, where the Volmer step is fast, both metal and phosphorus dissolve proportionally, maintaining catalytic activity. However, hydrogen bubble accumulation can form a resistive barrier that reduces performance. Optimizing the hydrophilic/hydrophobic balance of C-MoFeNiP could facilitate bubble release and improve activity.

1.5 HER Electrocatalytic Performance of Ni/MXene Composite Coatings

The electrocatalytic performance of Ni/MXene composite coatings toward the hydrogen evolution reaction (HER) was investigated to determine how the electrodeposition conditions influence their activity in alkaline medium. Four series of coatings were prepared at electrodeposition temperatures of 30, 40, 50, and 60 °C. Within each temperature series, the electrodeposition current density was

systematically varied from 5 to 25 mA cm^{-2}, while the deposition time was maintained at 20 min (Table 20). This experimental design enables the effects of deposition temperature and current density on the subsequent HER response of the Ni/MXene coatings to be evaluated systematically.

HER measurements were performed in 1 M NaOH at 25 °C. Consecutive polarization curves were recorded at a scan rate of 2 mV s^{-1}, and the stabilized polarization cycle was used for comparative kinetic analysis. The measured currents were normalized to the geometric electrode area of 4 cm^2, and potentials measured against saturated Ag/AgCl were converted to the reversible hydrogen electrode (RHE) scale. The electrochemical measurements were acquired with automatic iR compensation, minimizing the contribution of uncompensated solution resistance to the polarization response.

Table 20. Electrodeposition conditions for Ni/MXene composite coatings.

Sample	**t°C**	**j, mA/cm²**	**τ, min**
1	40	5	20
2		10	
3		15	
4		20	
5		25	
6	50	5	
7		10	
8		15	
9		20	
10		25	
11	60	5	

12		10	
13		15	
14		20	
15		25	
16	30	5	
17		10	
18		15	
19		20	
20		25	

1.5.1 Electrodeposition temperature 40°C

Samples 1–5 were electrodeposited at 40 °C using current densities of 5, 10, 15, 20, and 25 mA cm^{-2}, respectively. The individual polarization responses and the comparison of the final available polarization cycles are presented in Figures 47–52. For Samples 1, 2, 4, and 5, the eighth polarization cycle was used, whereas the seventh cycle was used for Sample 3 as the latest available measurement.

The characteristic overpotentials demonstrate that the HER performance did not vary monotonically with electrodeposition current density. At 1 mA cm^{-2}, the lowest overpotential was obtained for Sample 4, with η_1=164.2 mV, closely followed by Sample 1 at 166.1 mV and Sample 2 at 171.6 mV. Sample 3 required 176.6 mV, whereas Sample 5 exhibited the highest low-current overpotential of 192.8 mV. Thus, increasing the deposition current density from 5 to 20 mA cm^{-2} did not substantially alter the low-current polarization, but a further increase to 25 mA cm^{-2} shifted the polarization response toward considerably higher overpotential.

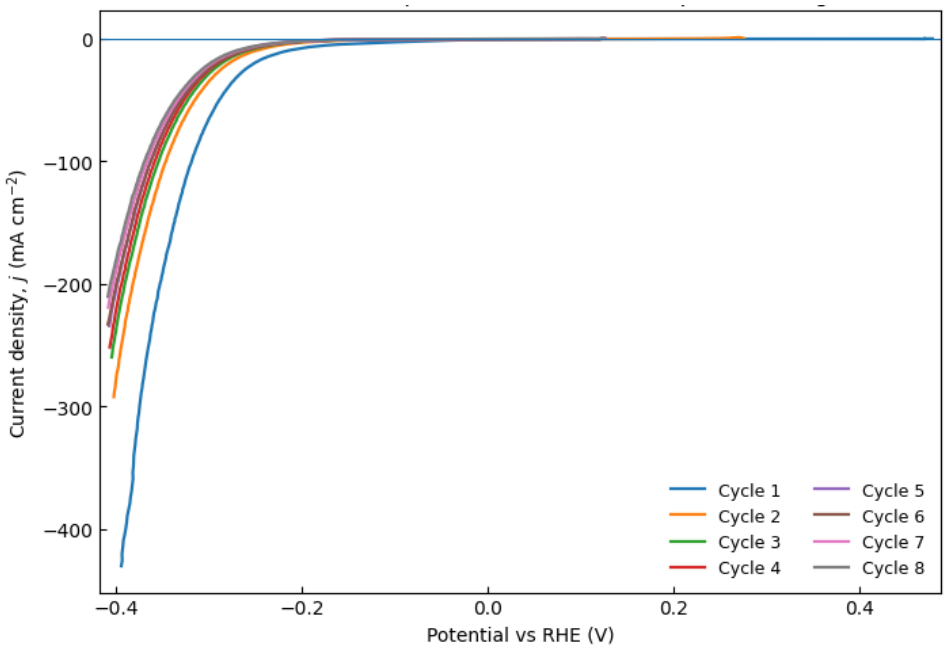


Figure 47. Linear sweep voltammograms of Ni/M-Xene-coated Sample 1 recorded during eight consecutive cycles in 1 M NaOH at 25 °C with a scan rate of 2 mV s^{-1}. Potentials are reported versus the reversible hydrogen electrode (RHE), and current densities are normalized to the geometric electrode area of 4 cm^2.

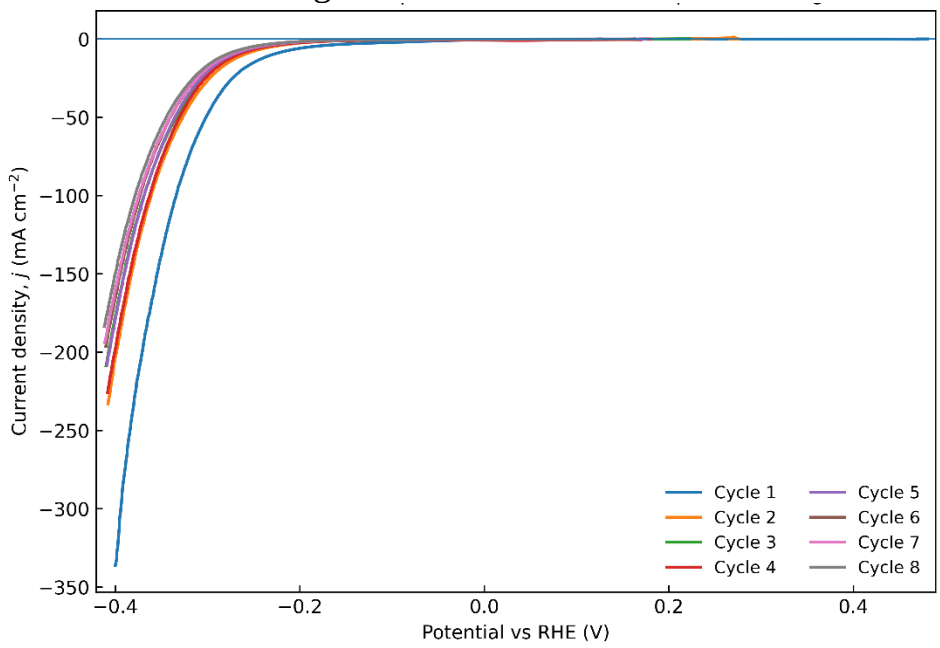


Figure 48. Linear sweep voltammograms of Ni/M-Xene-coated Sample 2 recorded during eight consecutive cycles in 1 M NaOH at 25 °C with a scan rate of 2 mV s^{-1}. Potentials are reported versus the reversible hydrogen electrode (RHE), and current densities are normalized to the geometric electrode area of 4 cm^2.

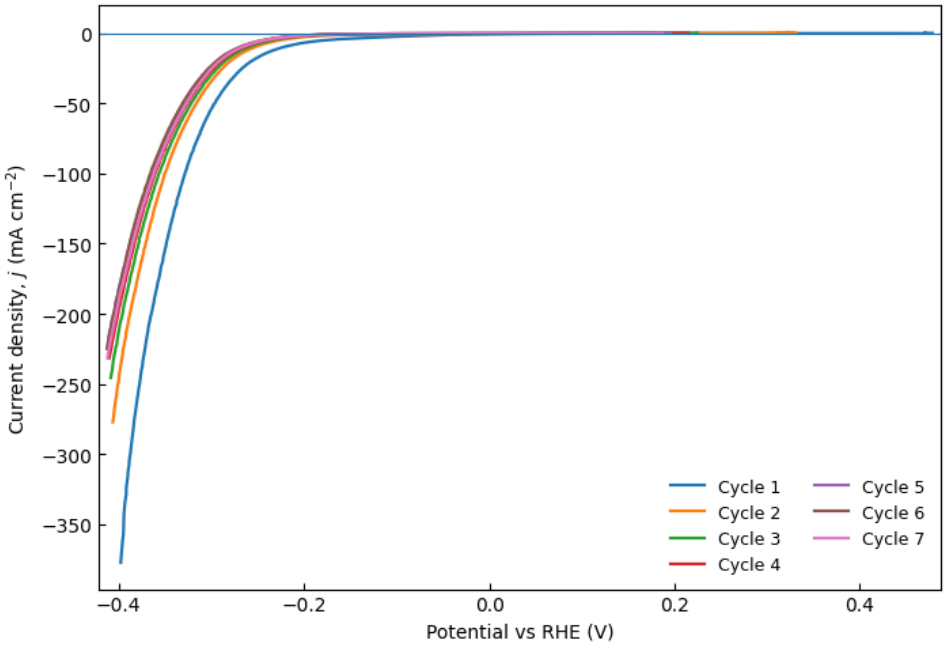


Figure 49. Linear sweep voltammograms of Ni/M-Xene-coated Sample 3 recorded during eight consecutive cycles in 1 M NaOH at 25 °C with a scan rate of 2 mV s^{-1}. Potentials are reported versus the reversible hydrogen electrode (RHE), and current densities are normalized to the geometric electrode area of 4 cm^2.

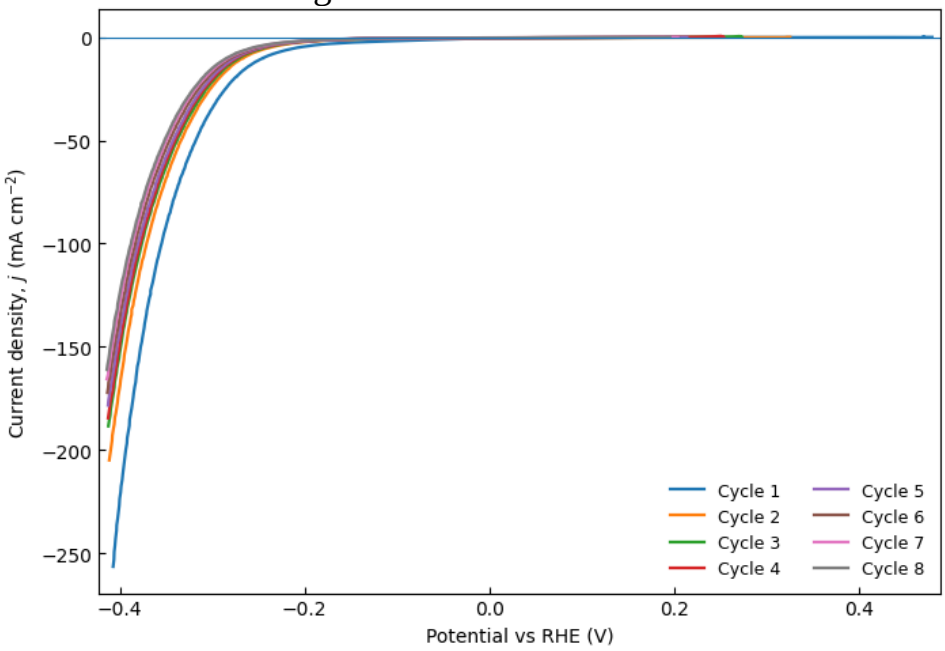


Figure 50. Linear sweep voltammograms of Ni/M-Xene-coated Sample 4 recorded during eight consecutive cycles in 1 M NaOH at 25 °C with a scan rate of 2 mV s^{-1}. Potentials are reported versus the reversible hydrogen electrode (RHE), and current densities are normalized to the geometric electrode area of 4 cm^2.

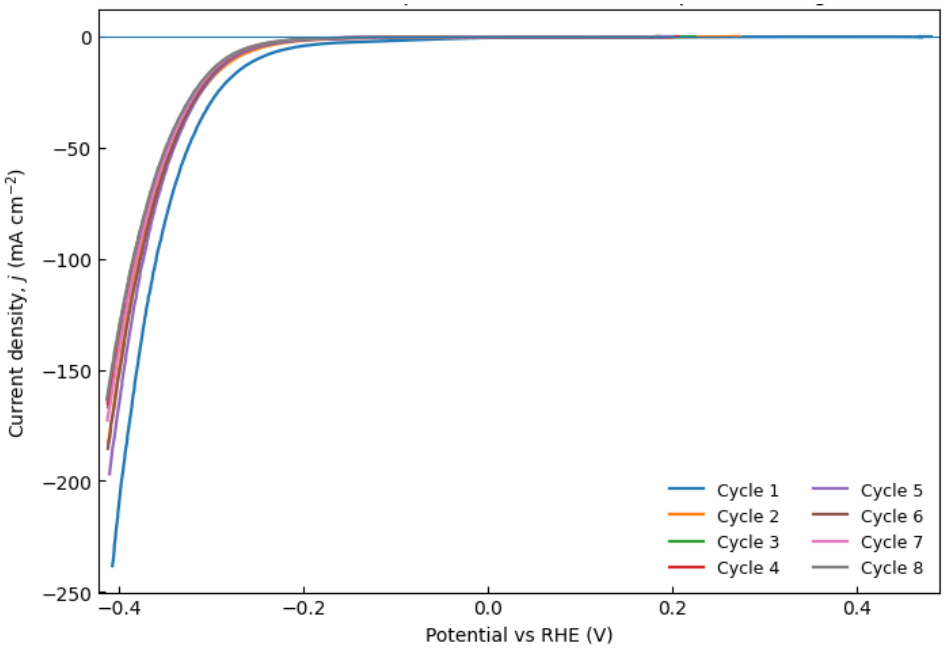


Figure 51. Linear sweep voltammograms of Ni/M-Xene-coated Sample 5 recorded during eight consecutive cycles in 1 M NaOH at 25 °C with a scan rate of 2 mV s^{-1}. Potentials are reported versus the reversible hydrogen electrode (RHE), and current densities are normalized to the geometric electrode area of 4 cm^2.

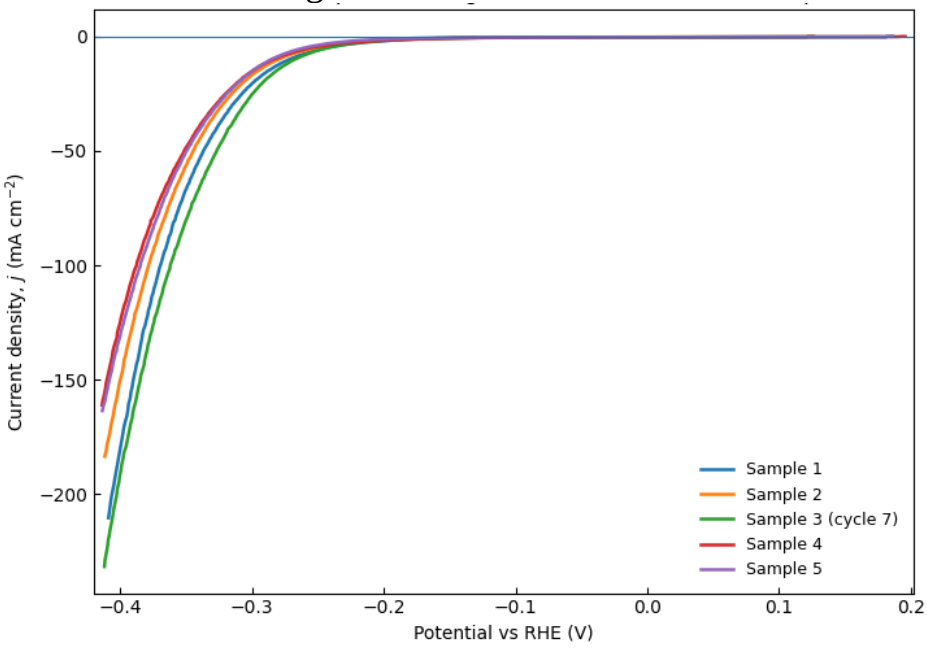


Figure 52. Linear sweep voltammograms of Ni/MXene-coated Samples 1–5 recorded in 1 M NaOH at 25 °C with a scan rate of 2 mV s^{-1}. The eighth polarization cycle is presented for Samples 1, 2, 4, and 5; for Sample 3, the seventh cycle is shown as the latest available measurement. Potentials are reported versus the

reversible hydrogen electrode (RHE), and current densities are normalized to the geometric electrode area of 4 cm². A saturated Ag/AgCl electrode was used as the reference electrode.

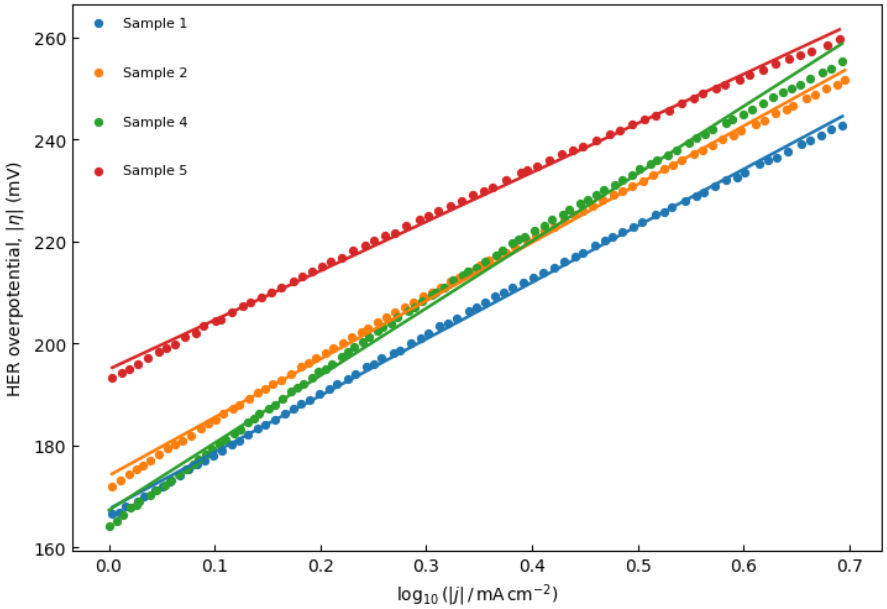


Figure 53. Tafel plots derived from the eighth-cycle polarization curves of Ni/M-Xene coated Samples 1, 2, 4 and 5 recorded in 1 M NaOH at 25 °C. Current densities were normalized to the geometric electrode area of 4 cm², and potentials were converted from saturated Ag/AgCl to the reversible hydrogen electrode (RHE) scale. Solid lines represent linear regressions over the current-density interval of 1–5 mA cm⁻².

Table 21. HER kinetic parameters and characteristic overpotentials derived from the eighth-cycle polarization curves of Ni/M-Xene composite coatings in 1 M NaOH at 25 °C.

Sample	Tafel intercept, a (V)	Tafel slope, $\|b\|$ (mV dec⁻¹)	R^2	Apparent j_0 (A cm⁻²)	95% CI for j_0 (mA cm⁻²)	η_1 (mV)	η_5 (mV)	η_{10} (mV)	η_{10} determination
1	0.1676	111.0	0.9986	3.087×10^{-5}	0.0298–0.0320	166.1	243.3	271.6	Interpolated from LSV
2	0.1741	114.2	0.9981	2.988×10^{-5}	0.0286–0.0312	171.6	251.9	279.9	Interpolated from LSV
3*	0.1780	93.7	0.9992	1.261×10^{-5}	0.0122–0.0131	176.6	242.2	267.8	Interpolated from LSV
4	0.1673	131.9	0.9961	5.391×10^{-5}	0.0514–0.0566	**164.2**	255.4	283.8	Interpolated from LSV
5	0.1950	**96.4**	0.9977	9.478×10^{-6}	0.0089–0.0101	192.8	260.4	285.2	Interpolated from LSV

A somewhat different ranking is obtained at higher HER current density. At 5 mA cm^{-2}, Sample 3 required the lowest overpotential, 242.2 mV, followed very closely by Sample 1 at 243.3 mV. Samples 2 and 4 required 251.9 and 255.4 mV, respectively, while Sample 5 again exhibited the highest value, 260.4 mV. At 10 mA cm^{-2}, Sample 3 maintained the most favorable response, with η_{10}=267.8 mV, followed by Sample 1 at 271.6 mV, Sample 2 at 279.9 mV, Sample 4 at 283.8 mV, and Sample 5 at 285.2 mV. All of these characteristic values were obtained from the measured LSV data.

The Tafel slopes provide additional information concerning the current response to increasing polarization. Sample 3 exhibited the smallest slope, 93.7 mV dec^{-1}, followed by Sample 5 at 96.4 mV dec^{-1}. Samples 1 and 2 showed intermediate values of 111.0 and 114.2 mV dec^{-1}, respectively, whereas Sample 4 exhibited the largest slope of 131.9 mV dec^{-1}. The comparatively small slope of Sample 3 is consistent with its increasingly favorable performance at higher current density: although its η_1 was not the lowest in the series, it exhibited the lowest η_5 and η_{10}.

The Tafel intercepts ranged from 0.1673 to 0.1950 V. Samples 1 and 4 exhibited the lowest intercepts, 0.1676 and 0.1673 V, respectively, consistent with their favorable polarization at approximately 1 mA cm^{-2}. Sample 5 exhibited the largest intercept, 0.1950 V. Its combination of a relatively small Tafel slope and high intercept explains why a favorable incremental current response does not translate into the lowest absolute operating overpotential.

The apparent exchange current densities likewise show that no individual Tafel parameter should be used alone to rank catalytic performance. Sample 4 exhibited the largest apparent j_0, $5.391 \cdot 10^{-5}$ A cm^{-2}, whereas Sample 5 exhibited the lowest value, $9.478 \cdot 10^{-6}$ A cm^{-2}. Sample 3, despite providing the smallest Tafel slope and lowest η_{10}, had an apparent j_0 of only $1.261 \cdot 10^{-5}$ A cm^{-2}.

Taken together, the results indicate that Sample 3 provides the most favorable overall high-current HER response within the 40 °C series, particularly on the basis of its low Tafel slope and the lowest η_5 and η_{10}. Samples 1 and 4 are slightly more favorable at 1 mA cm^{-2}, but this advantage is not maintained as current density increases. Deposition at the highest investigated current density of 25 mA cm^{-2} (Sample 5) appears unfavorable in terms of absolute polarization despite its relatively small Tafel slope.

1.5.2 Electrodeposition temperature 50°C

Samples 6–10 were prepared at 50 °C using electrodeposition current densities of 5, 10, 15, 20, and 25 mA cm^{-2}, respectively. Eight consecutive polarization cycles were recorded, and the eighth-cycle curves were used for comparative analysis. The corresponding LSV and Tafel results are presented in Figures 54–60 and Table 22.

The polarization results reveal a distinct non-monotonic dependence on deposition current density. Sample 10, prepared at the highest deposition current density of 25 mA cm^{-2}, exhibited the lowest η_1, only 153.3 mV. Sample 6 followed at 170.6 mV, while Samples 8, 7, and 9 required 174.0, 185.2, and 197.4 mV, respectively. Thus, Sample 10 shows a pronounced advantage in the low-current HER region.

At 5 mA cm^{-2}, Samples 6 and 10 exhibited almost identical performance, with η_5=250.7 and 250.9 mV, respectively. Samples 8 and 7 required 260.9 and 262.4 mV, while Sample 9 exhibited the highest η_5, 268.4 mV. At 10 mA cm^{-2}, Sample 6 provided the lowest overpotential of 278.8 mV, followed by Sample 10 at 282.2 mV. Samples 7, 8, and 9 exhibited values of 289.8, 291.2, and 294.9 mV, respectively.

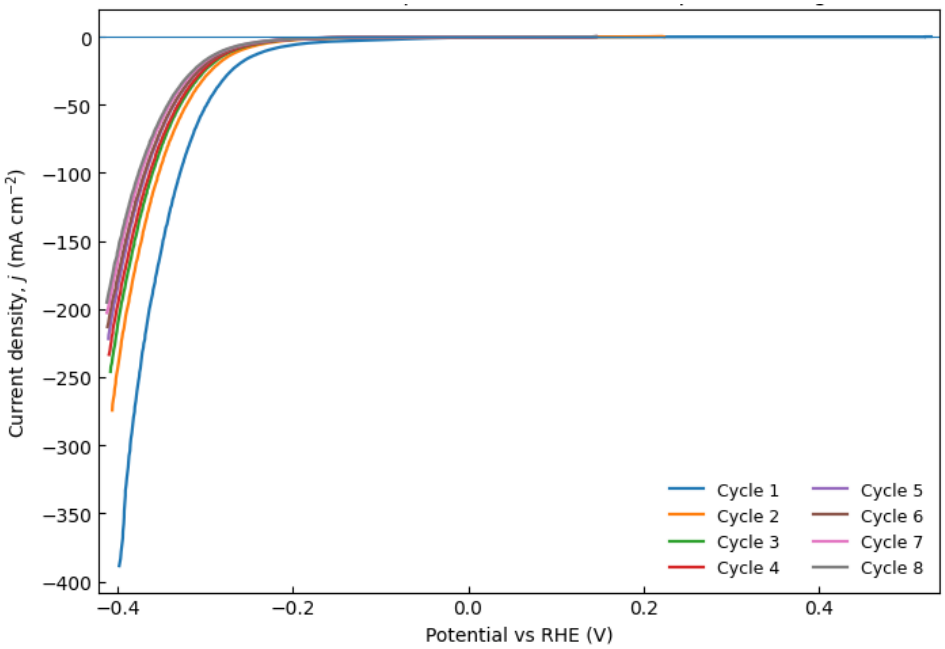


Figure 54. Linear sweep voltammograms of Ni/M-Xene-coated Sample 6 recorded during eight consecutive cycles in 1 M NaOH at 25 °C with a scan rate of 2 mV s^{-1}. Potentials are reported versus the reversible hydrogen electrode (RHE), and current densities are normalized to the geometric electrode area of 4 cm^2.

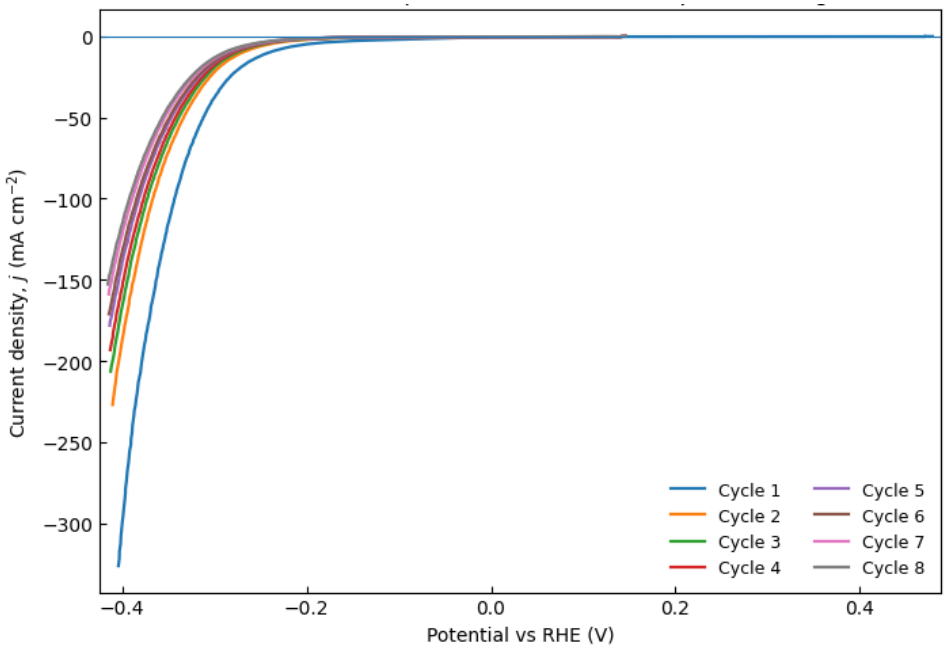


Figure 55. Linear sweep voltammograms of Ni/M-Xene-coated Sample 7 recorded during eight consecutive cycles in 1 M NaOH at 25 °C with a scan rate of 2 mV s^{-1}. Potentials are reported versus the reversible hydrogen electrode (RHE), and current densities are normalized to the geometric electrode area of 4 cm^2.

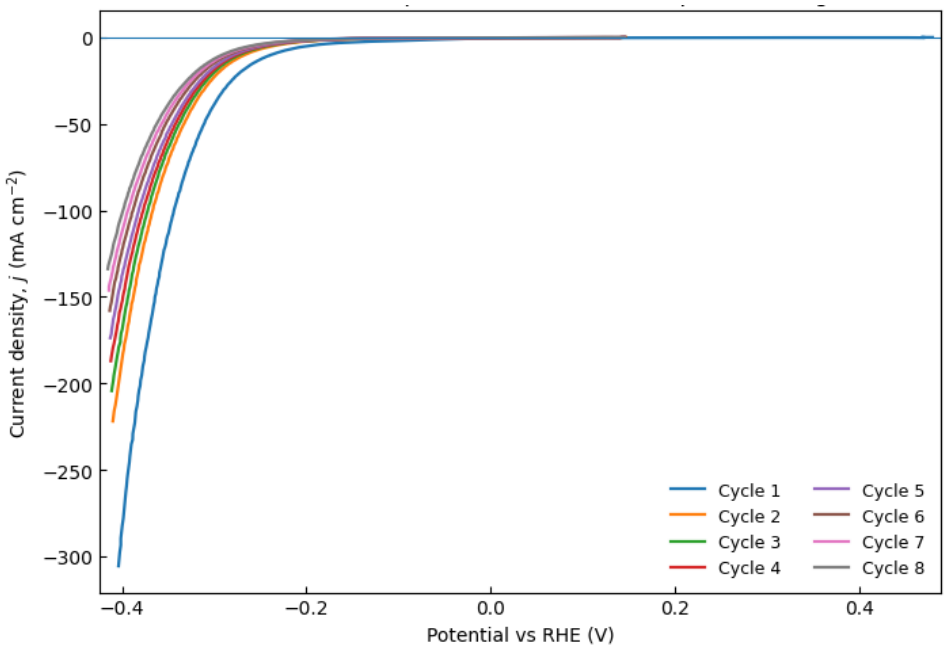


Figure 56. Linear sweep voltammograms of Ni/M-Xene-coated Sample 8 recorded during eight consecutive cycles in 1 M NaOH at 25 °C with a scan rate of 2 mV s^{-1}. Potentials are reported versus the reversible hydrogen electrode (RHE), and current densities are normalized to the geometric electrode area of 4 cm^2.

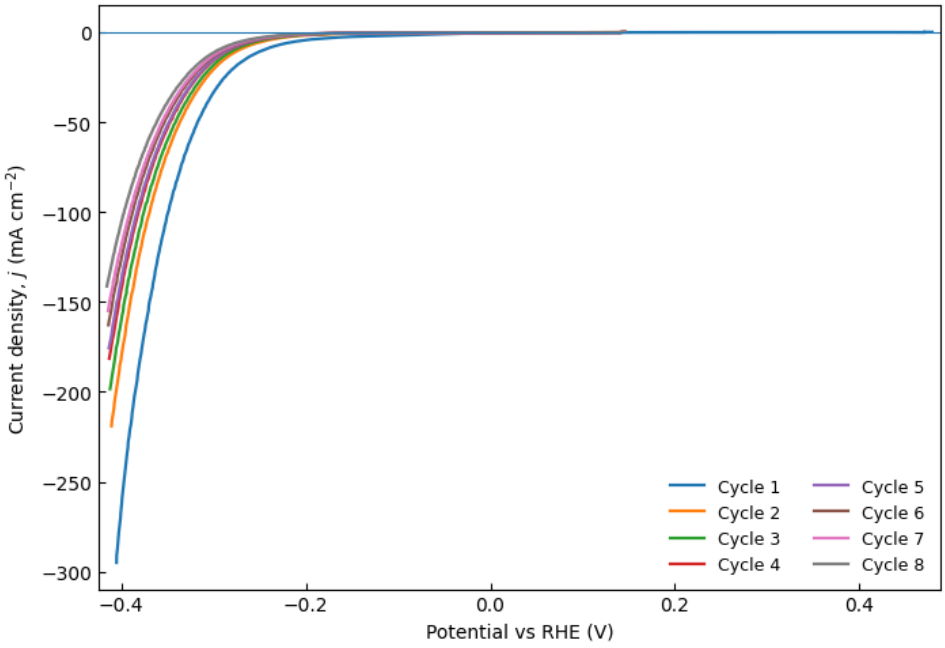


Figure 57. Linear sweep voltammograms of Ni/M-Xene-coated Sample 9 recorded during eight consecutive cycles in 1 M NaOH at 25 °C with a scan rate of 2 mV s^{-1}. Potentials are reported versus the reversible hydrogen electrode (RHE), and current densities are normalized to the geometric electrode area of 4 cm^2.

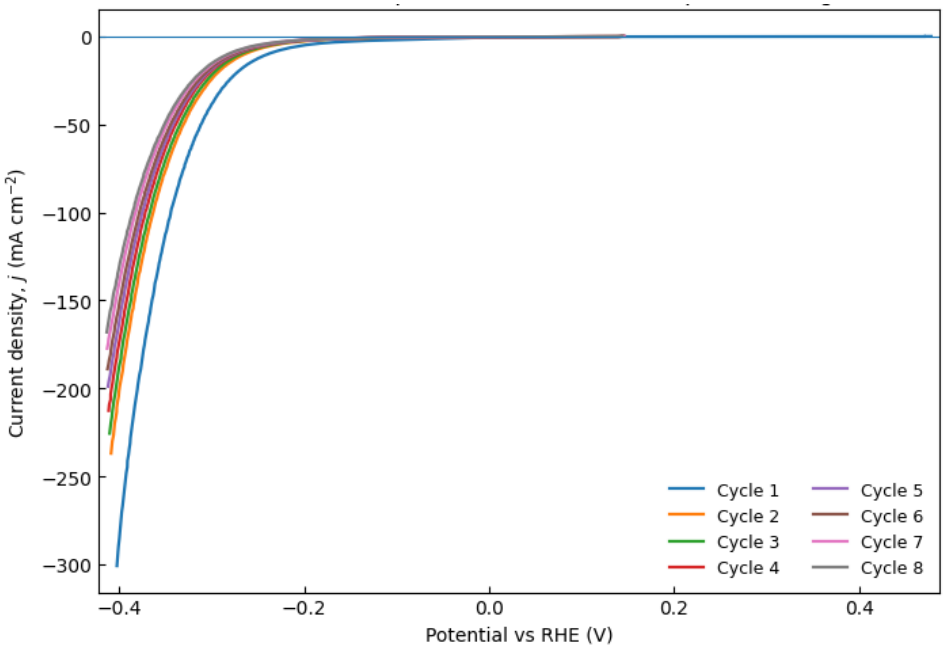


Figure 58. Linear sweep voltammograms of Ni/M-Xene-coated Sample 10 recorded during eight consecutive cycles in 1 M NaOH at 25 °C with a scan rate of 2 mV s^{-1}. Potentials are reported versus the reversible hydrogen electrode (RHE), and current densities are normalized to the geometric electrode area of 4 cm^2.

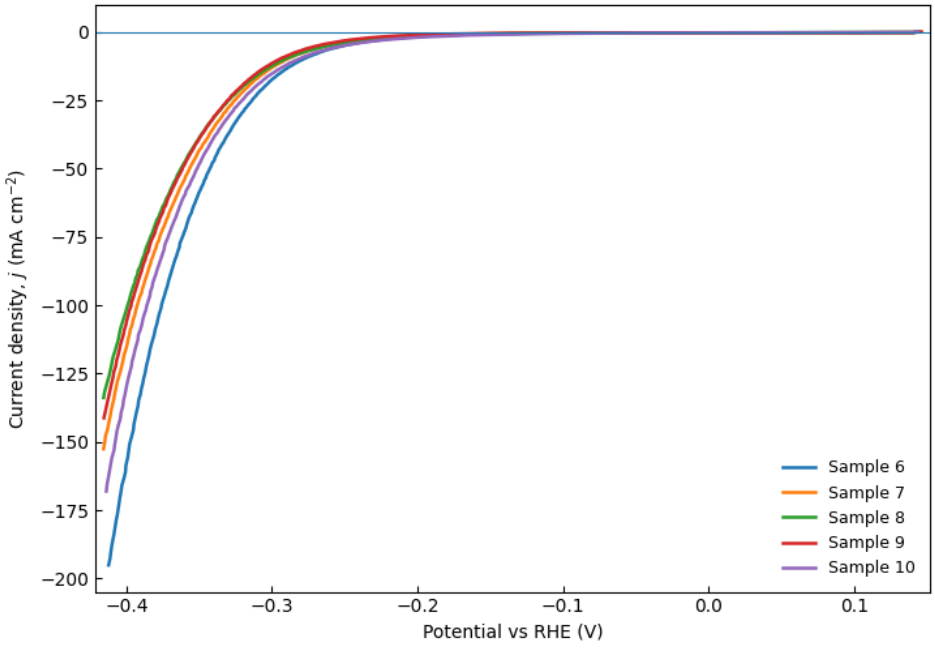


Figure 59. Linear sweep voltammograms of Ni/MXene-coated Samples 6–10 recorded in 1 M NaOH at 25 °C with a scan rate of 2 mV s^{-1}. The eighth polarization cycle is presented for Samples 6–10. Potentials are reported versus the reversible

hydrogen electrode (RHE), and current densities are normalized to the geometric electrode area of 4 cm².

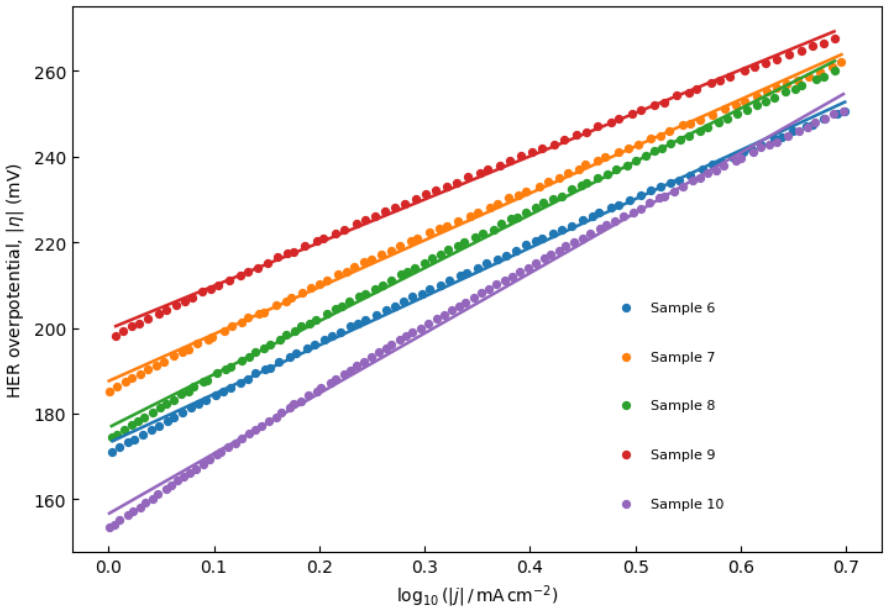


Figure 60. Tafel plots derived from the eighth-cycle polarization curves of Ni/M-Xene coated Samples 6–10 recorded in 1 M NaOH at 25 °C. Current densities were normalized to the geometric electrode area of 4 cm², and potentials were converted from saturated Ag/AgCl to the reversible hydrogen electrode (RHE) scale. Solid lines represent linear regressions over the current-density interval of 1–5 mA cm⁻².

Table 22. HER kinetic parameters and characteristic overpotentials derived from the eighth-cycle polarization curves of Ni/M-Xene composite coatings in 1 M NaOH at 25 °C.

Sample	Tafel intercept, a (V)	Tafel slope, $\|b\|$ (mV dec⁻¹)	R^2	Apparent j_0 (A cm⁻²)	95% CI for j_0 (mA cm⁻²)	η_1 (mV)	η_5 (mV)	η_{10} (mV)	η_{10} determination
6	0.1731	113.9	0.9981	3.025 × 10⁻⁵	0.0290–0.0316	170.6	**250.7**	**278.8**	Interpolated from LSV
7	0.1876	109.7	0.9979	1.950 × 10⁻⁵	0.0186–0.0205	185.2	262.4	289.8	Interpolated from LSV
8	0.1767	124.2	0.9979	3.783 × 10⁻⁵	0.0363–0.0394	174.0	260.9	291.2	Interpolated from LSV
9	0.1997	**101.0**	0.9981	1.052 × 10⁻⁵	0.0100–0.0111	197.4	268.4	294.9	Interpolated from LSV
10	**0.1566**	140.6	0.9966	**7.697 × 10⁻⁵**	0.0740–0.0801	**153.3**	250.9	282.2	Interpolated from LSV

The Tafel slopes ranged from 101.0 to 140.6 mV dec^{-1}. Sample 9 exhibited the smallest slope, 101.0 mV dec^{-1}, followed by Sample 7 at 109.7 mV dec^{-1} and Sample 6 at 113.9 mV dec^{-1}. Sample 8 showed a somewhat larger value of 124.2 mV dec^{-1}, whereas Sample 10 exhibited the largest slope, 140.6 mV dec^{-1}. This produces an instructive contrast: Sample 10 has the lowest low-current operating overpotential but the largest Tafel slope, while Sample 9 has the smallest Tafel slope but the highest absolute overpotentials within much of the investigated range.

The intercept values clarify this behavior. Sample 10 has the lowest intercept of 0.1566 V, whereas Sample 9 has the highest intercept of 0.1997 V. Thus, although the current of Sample 9 increases relatively favorably with additional polarization, its Tafel relationship begins from a substantially less favorable absolute overpotential. Sample 10 displays the opposite combination, a favorable low-current position but a steeper increase in overpotential with logarithmic current density.

The apparent j_0 values follow the position of the fitted Tafel lines rather than simply the slope ranking. Sample 10 exhibited the largest apparent exchange current density, $7.697 \cdot 10^{-5}$ A cm^{-2}, followed by Sample 8 at $3.783 \cdot 10^{-5}$ A cm^{-2} and Sample 6 at $3.025 \cdot 10^{-5}$ A cm^{-2}. Samples 7 and 9 exhibited lower values of $1.950 \cdot 10^{-5}$ and $1.052 \cdot 10^{-5}$ A cm^{-2}, respectively.

Overall, the 50 °C series does not exhibit a single monotonically optimum deposition-current trend. Sample 10 provides the most favorable low-current response and largest apparent j_0, whereas Sample 6 slightly outperforms it at 5–10 mA cm^{-2} and has a substantially smaller Tafel slope. Sample 9 demonstrates particularly clearly why Tafel slope alone cannot be used to define the best HER catalyst: despite exhibiting the smallest slope, its polarization curve is shifted toward higher absolute overpotential.

1.5.3 Electrodeposition temperature 60ºC

Samples 11–15 correspond to electrodeposition at 60 °C and current densities of 5, 10, 15, 20, and 25 mA cm^{-2}, respectively. The eighth polarization cycles were used for comparative analysis, with the corresponding polarization and Tafel results presented in Figures 61–67 and Table 23.

Within this series, Samples 12 and 13 exhibited the most favorable operating overpotentials. At 1 mA cm^{-2}, Sample 12 required 149.40 mV and Sample 13 required 149.53 mV, effectively identical within the resolution relevant to the present comparison. These values were substantially lower than those of Sample 11 (164.33 mV), Sample 15 (178.01 mV), and Sample 14 (187.51 mV).

The advantage of Sample 13 becomes clearer as the HER current increases. At 5 mA cm^{-2}, Sample 13 exhibited the lowest overpotential of 235.91 mV, followed by Sample 12 at 238.69 mV. Samples 11, 15, and 14 required 251.39, 259.85, and 263.91 mV, respectively. At 10 mA cm^{-2}, Sample 13 again showed the lowest overpotential, 266.44 mV, narrowly outperforming Sample 12 at 268.09 mV. The corresponding values for Samples 11, 15, and 14 were 282.20, 288.13, and 290.78 mV. All reported η_{10} values for this series were obtained by interpolation of the eighth-cycle polarization curves.

Interestingly, the Tafel-slope ranking differs substantially from the operating-overpotential ranking. Sample 14 exhibited the smallest Tafel slope, 108.42 mV dec^{-1}, despite having the highest η_1, η_5, and η_{10} within this series. Samples 15, 11, 13, and 12 exhibited slopes of 117.07, 122.30, 123.10, and 127.41 mV dec^{-1}, respectively. Thus, Sample 14 responds favorably to additional polarization in logarithmic terms, but its entire polarization curve is displaced toward higher overpotential.

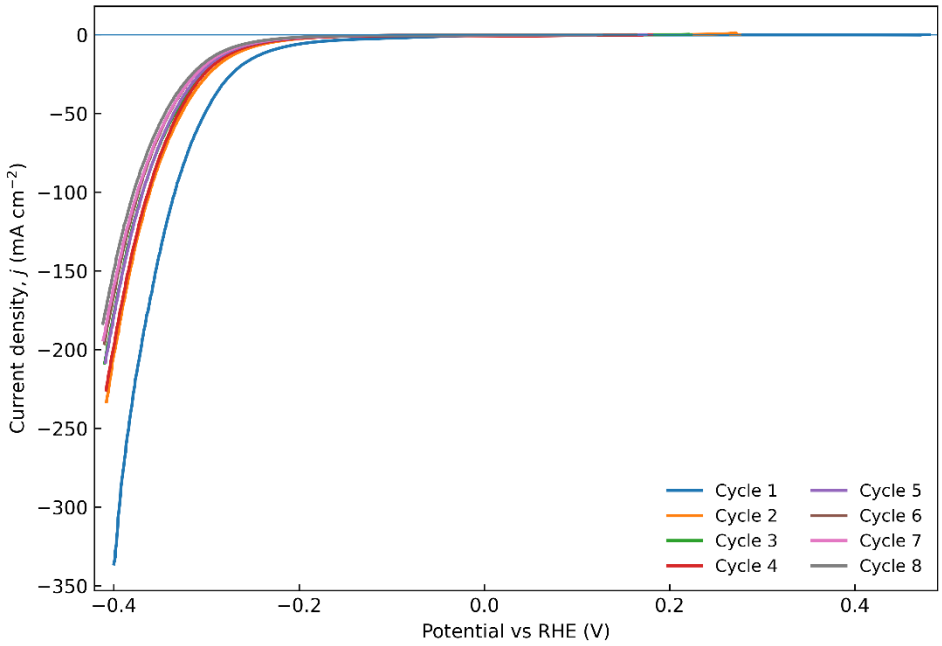


Figure 61. Linear sweep voltammograms of Ni/M-Xene-coated Sample 11 recorded during eight consecutive cycles in 1 M NaOH at 25 °C with a scan rate of 2 mV s^{-1}. Potentials are reported versus the reversible hydrogen electrode (RHE), and current densities are normalized to the geometric electrode area of 4 cm^2.

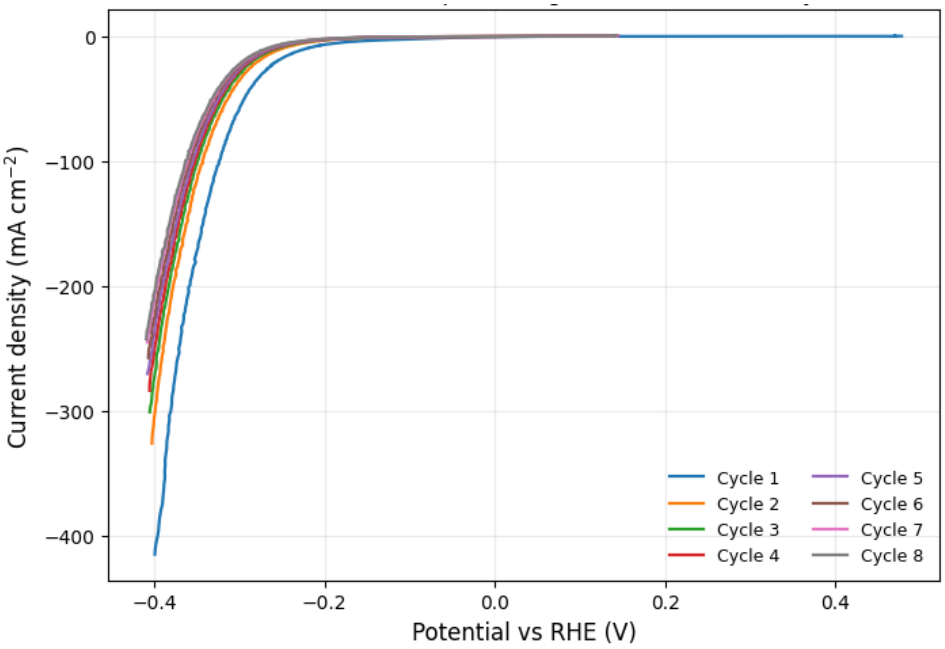


Figure 62. Linear sweep voltammograms of Ni/M-Xene-coated Sample 12 recorded during eight consecutive cycles in 1 M NaOH at 25 °C with a scan rate of 2 mV s^{-1}. Potentials are reported versus the reversible hydrogen electrode (RHE), and current densities are normalized to the geometric electrode area of 4 cm^2.

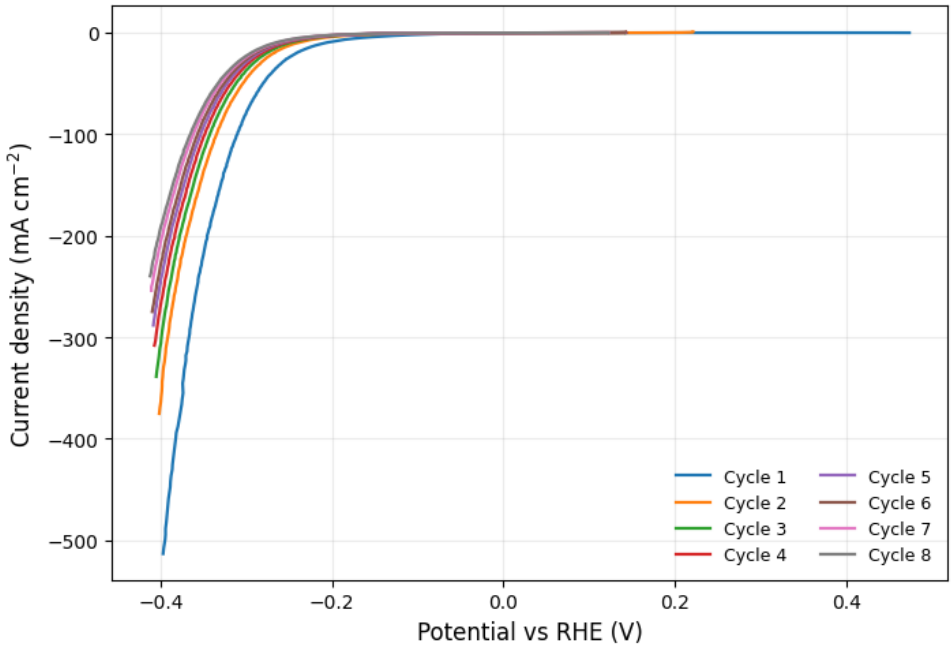


Figure 63. Linear sweep voltammograms of Ni/M-Xene-coated Sample 13 recorded during eight consecutive cycles in 1 M NaOH at 25 °C with a scan rate of 2 mV s^{-1}. Potentials are reported versus the reversible hydrogen electrode (RHE), and current densities are normalized to the geometric electrode area of 4 cm^2.

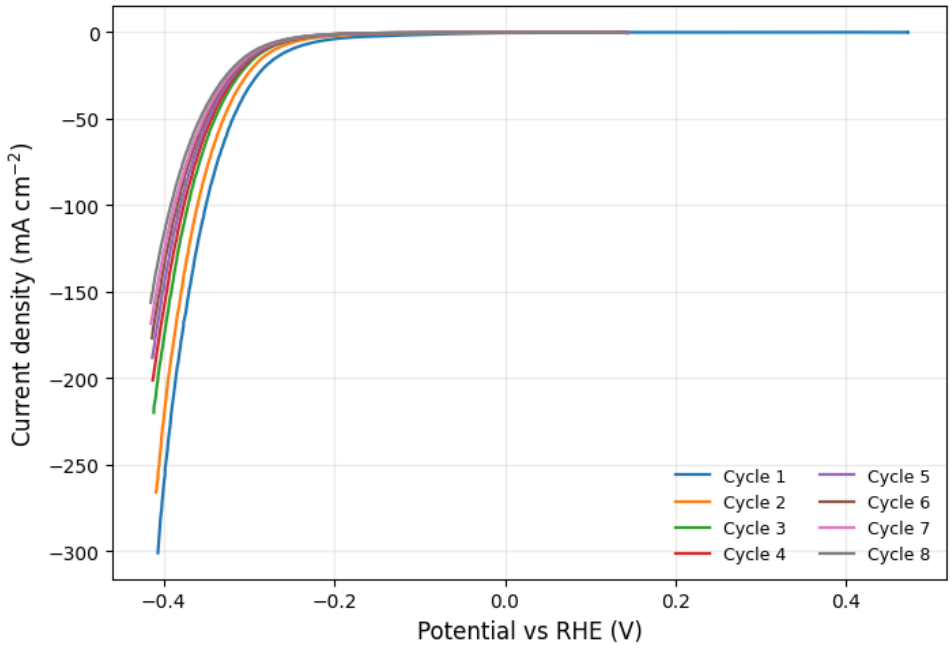


Figure 64. Linear sweep voltammograms of Ni/M-Xene-coated Sample 14 recorded during eight consecutive cycles in 1 M NaOH at 25 °C with a scan rate of 2 mV s^{-1}. Potentials are reported versus the reversible hydrogen electrode (RHE), and current densities are normalized to the geometric electrode area of 4 cm^2.

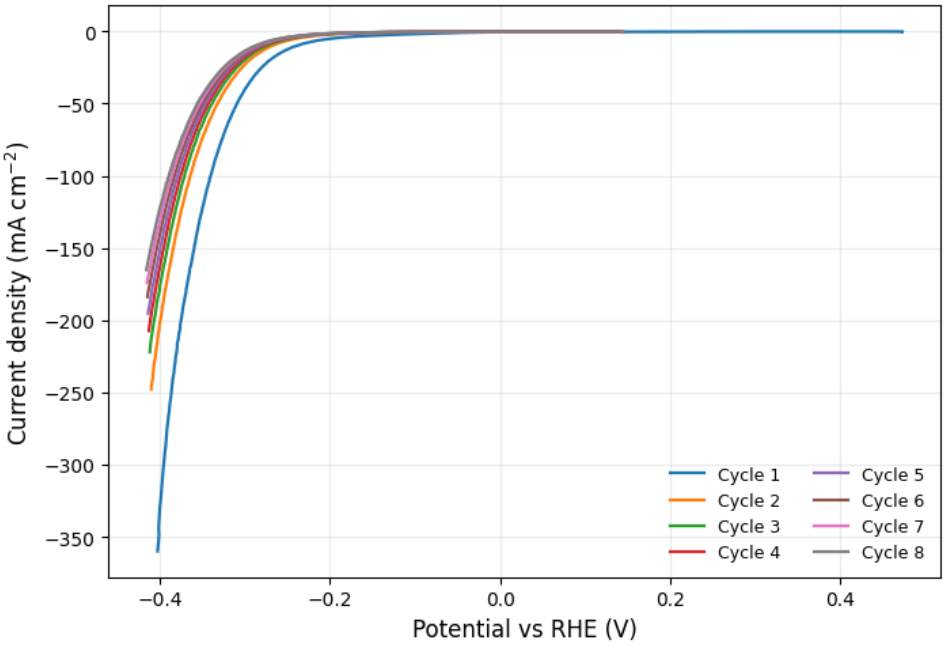


Figure 65. Linear sweep voltammograms of Ni/M-Xene-coated Sample 15 recorded during eight consecutive cycles in 1 M NaOH at 25 °C with a scan rate of 2 mV s^{-1}. Potentials are reported versus the reversible hydrogen electrode (RHE), and current densities are normalized to the geometric electrode area of 4 cm^2.

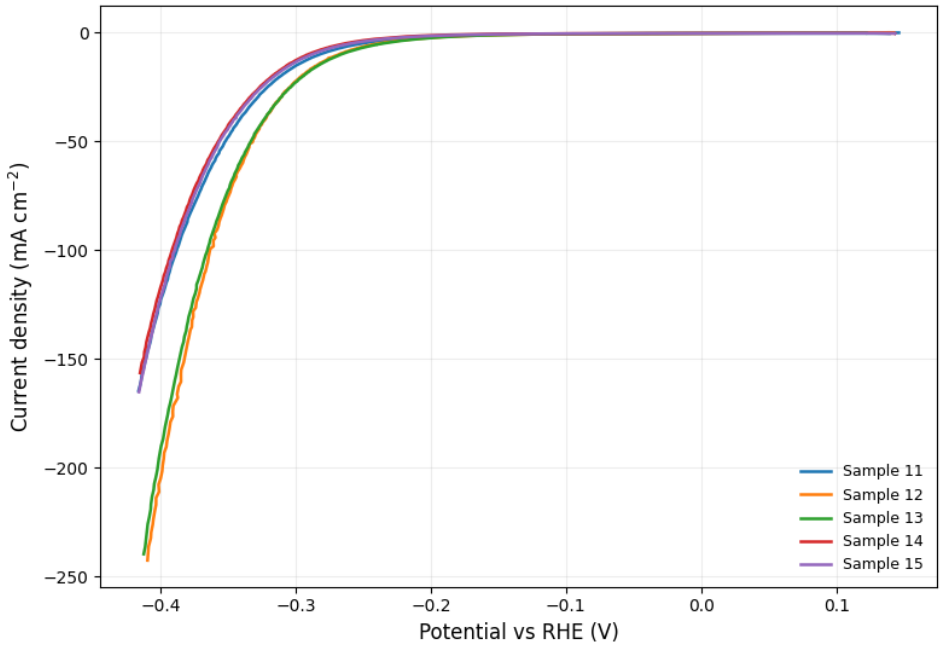


Figure 66. Linear sweep voltammograms of Ni/MXene-coated Samples 11–15 recorded in 1 M NaOH at 25 °C with a scan rate of 2 mV s^{-1}. The eighth polarization

cycle is presented for Samples 11–15. Potentials are reported versus the reversible hydrogen electrode (RHE), and current densities are normalized to the geometric electrode area of 4 cm².

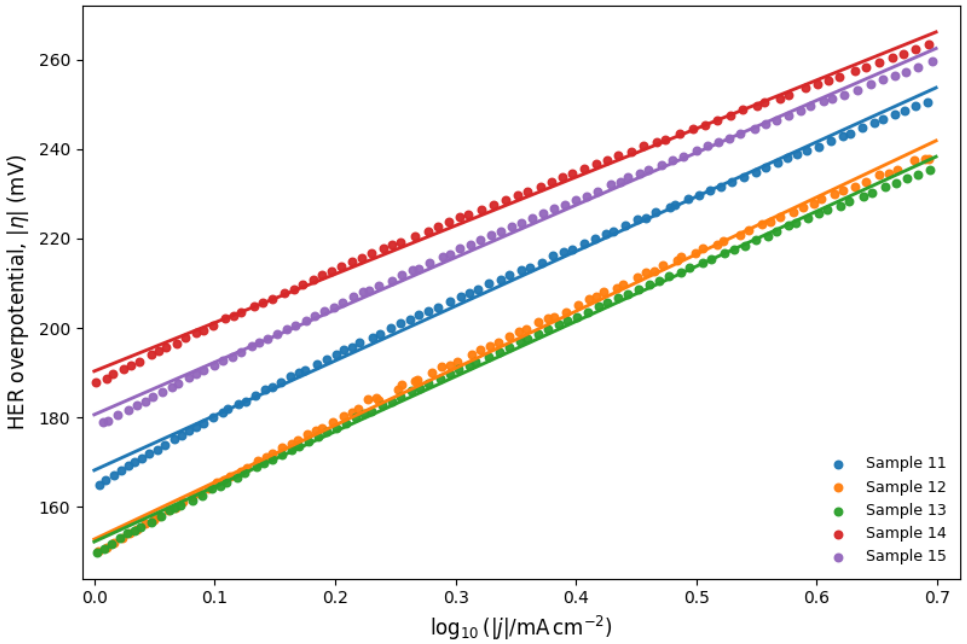


Figure 67. Tafel plots derived from the eighth-cycle polarization curves of Ni/M-Xene coated Samples 11–15 recorded in 1 M NaOH at 25 °C. Current densities were normalized to the geometric electrode area of 4 cm², and potentials were converted from saturated Ag/AgCl to the reversible hydrogen electrode (RHE) scale. Solid lines represent linear regressions over the current-density interval of 1–5 mA cm⁻².

Table 23. HER kinetic parameters and characteristic overpotentials derived from the eighth-cycle polarization curves of Ni/M-Xene composite coatings in 1 M NaOH at 25 °C.

Sample	Tafel intercept, a (V)	Tafel slope, $\|b\|$ (mV dec⁻¹)	R^2	Apparent j_0 (A cm⁻²)	95% CI for j_0 (mA cm⁻²)	η_1 (mV)	η_5 (mV)	η_{10} (mV)	η_{10} determination
11	0.1682	122.30	0.9968	4.213 × 10⁻⁵	0.0401–0.0442	164.33	251.39	282.20	Cycle 8 LSV interpolation
12	0.1528	127.41	0.9969	6.321 × 10⁻⁵	0.0606–0.0659	149.40	238.69	268.09	Cycle 8 LSV interpolation
13	0.1522	123.10	0.9982	5.798 × 10⁻⁵	0.0561–0.0600	149.53	**235.91**	**266.44**	Cycle 8 LSV interpolation
14	0.1904	**108.42**	0.9969	1.755 × 10⁻⁵	0.0165–0.0187	187.51	263.91	290.78	Cycle 8 LSV interpolation
15	0.1806	117.07	0.9972	2.864 × 10⁻⁵	0.0272–0.0301	178.01	259.85	288.13	Cycle 8 LSV interpolation

This indicated behavior is also reflected in the Tafel intercept. Samples 12 and 13 exhibited the lowest intercepts, 0.1528 and 0.1522 V, respectively, whereas Sample 14 exhibited the largest value of 0.1904 V. Consequently, the smaller slope of Sample 14 cannot compensate for its unfavorable initial position within the experimentally relevant current-density range. In contrast, the low intercepts of Samples 12 and 13 are consistent with their lower operating overpotentials.

The apparent j_0 values were highest for Sample 12 – $6.321 \cdot 10^{-5}$ A cm^{-2} and Sample 13 – $5.798 \cdot 10^{-5}$ A cm^{-2}, followed by Sample 11 – $4.213 \cdot 10^{-5}$ A cm^{-2}, Sample 15 – 2.864·10-5 A cm^{-2}, and Sample 14 – $1.755 \cdot 10^{-5}$ A cm^{-2}. The consistency between low operating overpotentials, low intercepts, and relatively high apparent j_0 strengthens the identification of Samples 12 and 13 as the most favorable electrodes within this series.

Overall, electrodeposition at 10–15 mA cm^{-2} appears optimal within the 60 °C series, with Sample 13 showing the best overall performance at intermediate and higher HER current densities. Increasing the deposition current density to 20–25 mA cm^{-2} shifts the polarization response toward higher overpotential. Sample 14 is particularly instructive because its lowest Tafel slope does not translate into superior practical HER activity.

1.5.4 Electrodeposition temperature 30ºC

Samples 16–20 were prepared at 30 °C using deposition current densities of 5, 10, 15, 20, and 25 mA cm^{-2}, respectively. The eighth polarization cycles are compared in Figure 73, while the corresponding Tafel analysis and derived HER parameters are presented in Figure 74 and Table 24.

This series exhibits the clearest systematic dependence of HER performance on deposition current density among the four investigated temperatures. The operating overpotential decreases progressively as the deposition current density increases. At 1 mA cm^{-2}, η_1 decreases from 140.12 mV for Sample 16 to 110.51 mV for

Sample 17, 104.96 mV for Sample 18, 94.86 mV for Sample 19, and only 74.79 mV for Sample 20.

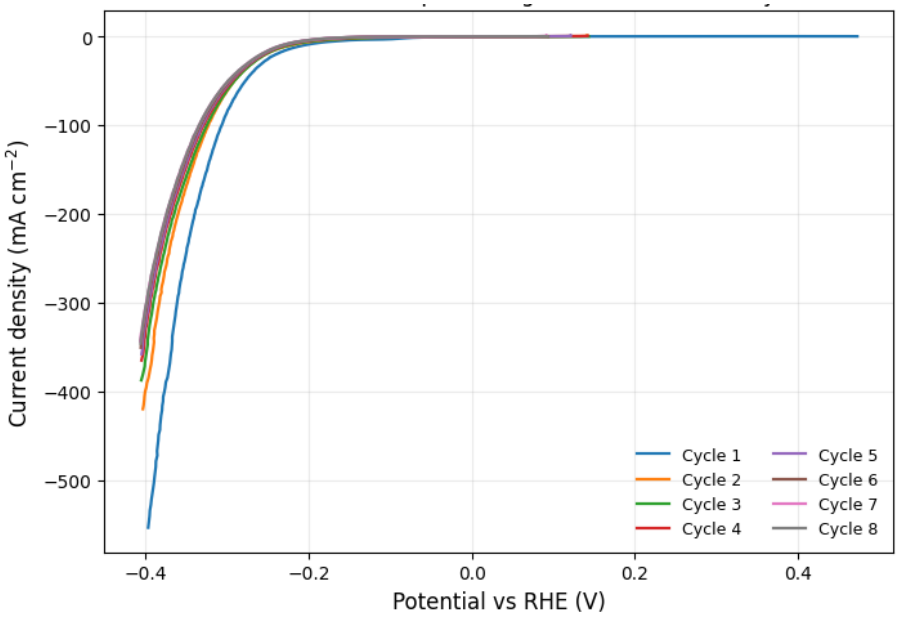


Figure 68. Linear sweep voltammograms of Ni/M-Xene-coated Sample 16 recorded during eight consecutive cycles in 1 M NaOH at 25 °C with a scan rate of 2 mV s^{-1}. Potentials are reported versus the reversible hydrogen electrode (RHE), and current densities are normalized to the geometric electrode area of 4 cm^2.

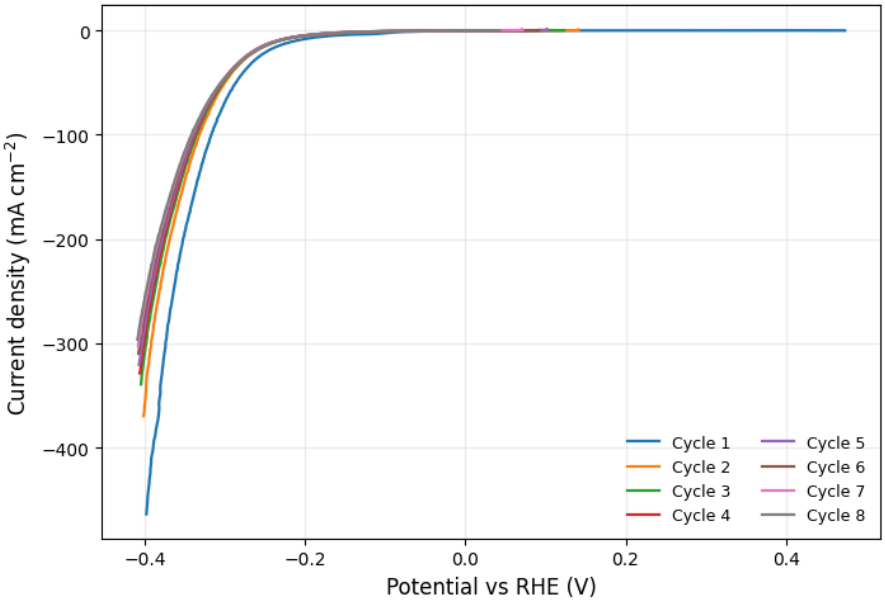


Figure 69. Linear sweep voltammograms of Ni/M-Xene-coated Sample 17 recorded during eight consecutive cycles in 1 M NaOH at 25 °C with a scan rate of 2 mV s^{-1}.

Potentials are reported versus the reversible hydrogen electrode (RHE), and current densities are normalized to the geometric electrode area of 4 cm².

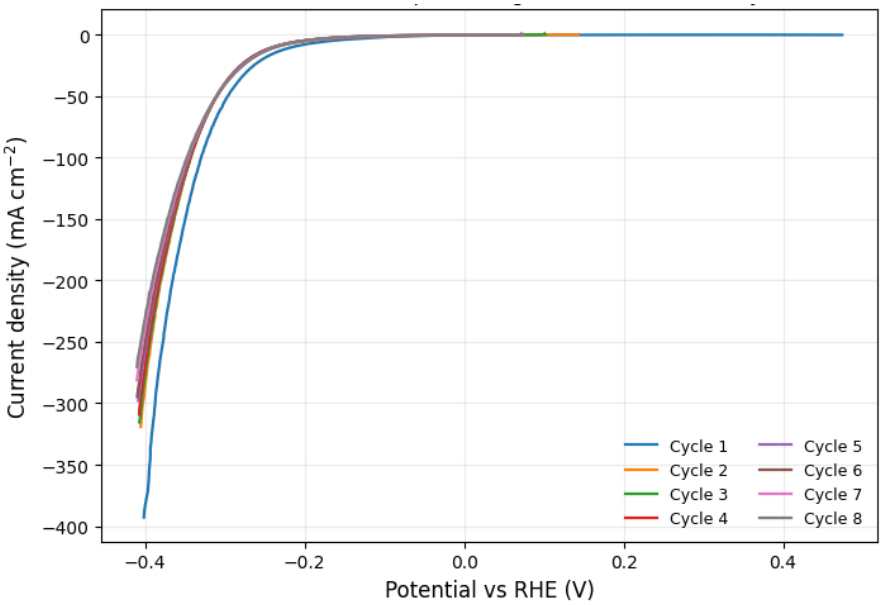


Figure 70. Linear sweep voltammograms of Ni/M-Xene-coated Sample 18 recorded during eight consecutive cycles in 1 M NaOH at 25 °C with a scan rate of 2 mV s^{-1}. Potentials are reported versus the reversible hydrogen electrode (RHE), and current densities are normalized to the geometric electrode area of 4 cm².

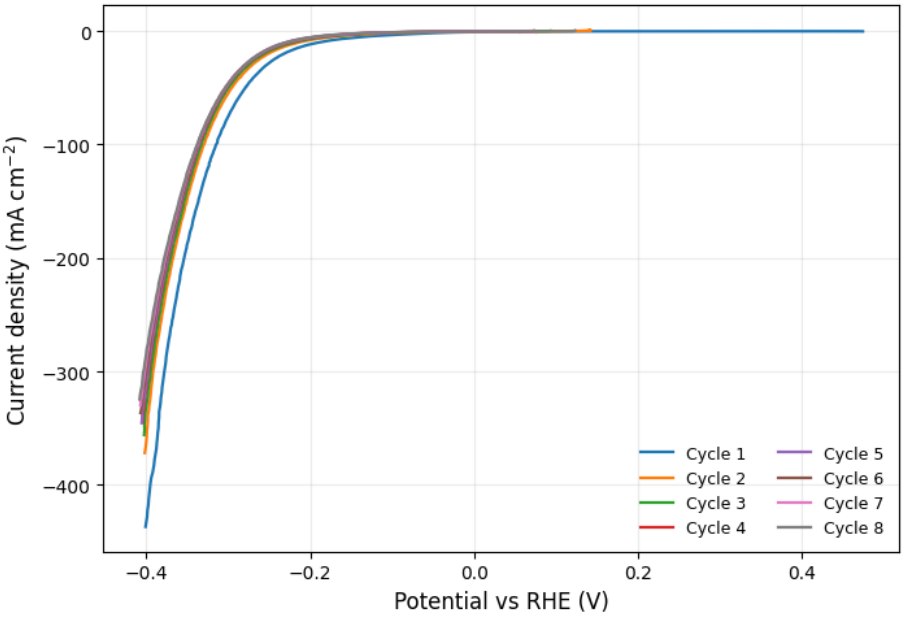


Figure 71. Linear sweep voltammograms of Ni/M-Xene-coated Sample 19 recorded during eight consecutive cycles in 1 M NaOH at 25 °C with a scan rate of 2 mV s^{-1}.

Potentials are reported versus the reversible hydrogen electrode (RHE), and current densities are normalized to the geometric electrode area of 4 cm².

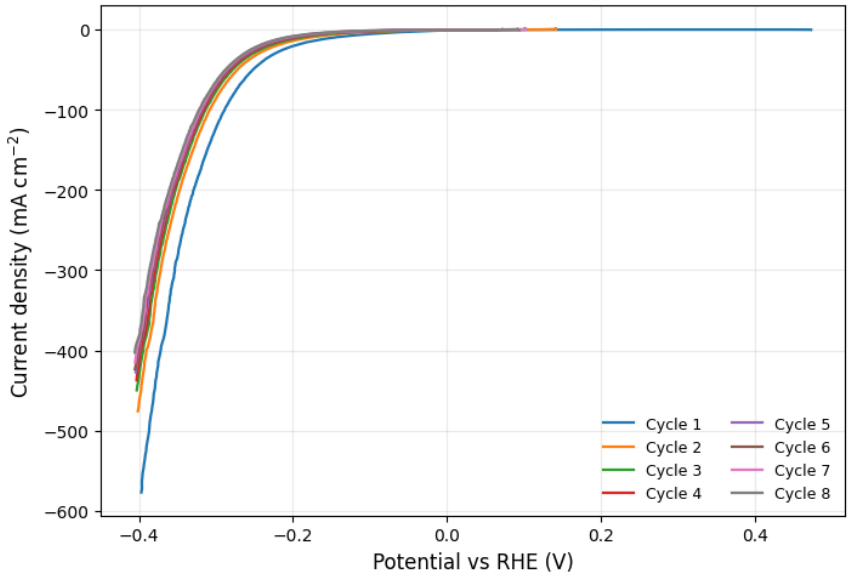


Figure 72. Linear sweep voltammograms of Ni/M-Xene-coated Sample 20 recorded during eight consecutive cycles in 1 M NaOH at 25 °C with a scan rate of 2 mV s^{-1}. Potentials are reported versus the reversible hydrogen electrode (RHE), and current densities are normalized to the geometric electrode area of 4 cm².

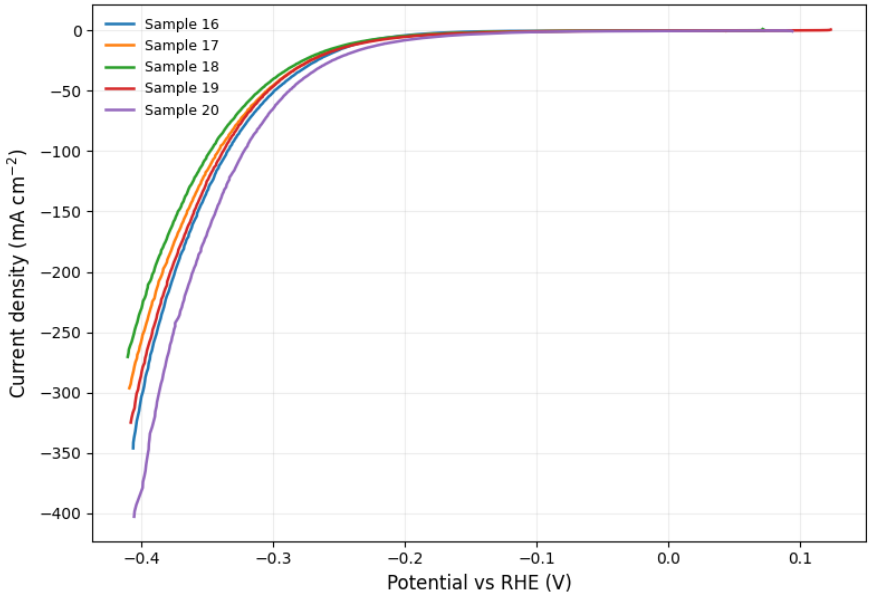


Figure 73. Linear sweep voltammograms of Ni/MXene-coated Samples 16–20 recorded in 1 M NaOH at 25 °C with a scan rate of 2 mV s^{-1}. The eighth polarization cycle is presented for Samples 16–20. Potentials are reported versus the reversible

hydrogen electrode (RHE), and current densities are normalized to the geometric electrode area of 4 cm².

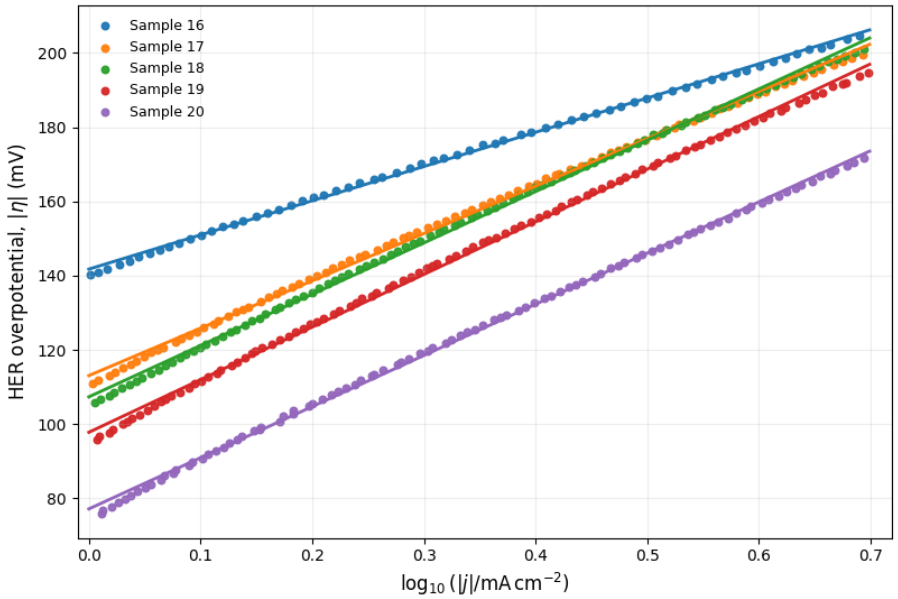


Figure 74. Tafel plots derived from the eighth-cycle polarization curves of Ni/M-Xene coated Samples 16–20 recorded in 1 M NaOH at 25 °C. Current densities were normalized to the geometric electrode area of 4 cm², and potentials were converted from saturated Ag/AgCl to the reversible hydrogen electrode (RHE) scale. Solid lines represent linear regressions over the current-density interval of 1–5 mA cm⁻².

Table 24. HER kinetic parameters and characteristic overpotentials derived from the eighth-cycle polarization curves of Ni/M-Xene composite coatings in 1 M NaOH at 25 °C.

Sample	Tafel intercept, a (V)	Tafel slope, $\|b\|$ (mV dec^{-1})	R^2	Apparent j_0 (A cm^{-2})	95% CI for j_0 (mA cm^{-2})	η_1 (mV)	η_5 (mV)	η_{10} (mV)	η_{10} determination
16	0.1418	**92.21**	0.9988	2.902 × 10^{-5}	0.0279–0.0301	140.12	205.48	231.91	Cycle 8 LSV interpolation
17	0.1131	127.65	0.9985	1.301 × 10^{-4}	0.1271–0.1331	110.51	200.37	232.48	Cycle 8 LSV interpolation
18	0.1074	138.32	0.9987	1.675 × 10^{-4}	0.1643–0.1707	104.96	201.81	235.88	Cycle 8 LSV interpolation
19	0.0978	141.83	0.9985	2.044 × 10^{-4}	0.2006–0.2082	94.86	194.74	229.47	Cycle 8 LSV interpolation
20	**0.0772**	137.88	**0.9990**	**2.757 × 10^{-4}**	**0.2719–0.2794**	**74.79**	**172.22**	**209.52**	Cycle 8 LSV interpolation

The same trend is observed at higher current densities. At 5 mA cm^{-2}, the overpotential decreases from 205.48 mV for Sample 16 to 200.37, 201.81, 194.74, and finally 172.22 mV for Sample 20. At 10 mA cm^{-2}, Sample 20 again provides the lowest overpotential, only 209.52 mV, compared with 229.47 mV for Sample 19, 231.91 mV for Sample 16, 232.48 mV for Sample 17, and 235.88 mV for Sample 18. All η_{10} values were obtained by interpolation of the experimentally measured Cycle 8 LSV curves rather than by Tafel extrapolation.

The Tafel slopes, however, display a different trend. Sample 16 exhibited the smallest slope, 92.21 mV dec^{-1}. The slope increased to 127.65 mV dec^{-1} for Sample 17, 138.32 mV dec^{-1} for Sample 18, and 141.83 mV dec^{-1} for Sample 19, before decreasing slightly to 137.88 mV dec^{-1} for Sample 20. Therefore, the substantial improvement in absolute HER polarization with increasing deposition current density is not caused by a systematic decrease in Tafel slope.

Instead, the Tafel intercept shifts very strongly toward lower overpotential. It decreases from 0.1418 V for Sample 16 to 0.1131, 0.1074, 0.0978, and finally only 0.0772 V for Sample 20. This trend closely parallels the experimental η_1 values and demonstrates that the primary improvement is associated with a pronounced displacement of the polarization curve toward lower absolute overpotential. Sample 20 therefore begins the investigated HER current region from a much more favorable polarization state even though its Tafel slope is larger than that of Sample 16.

The apparent exchange current density increases correspondingly from $2.902 \cdot 10^{-5}$ A cm^{-2} for Sample 16 to $1.301 \cdot 10^{-4}$, $1.675 \cdot 10^{-4}$, $2.044 \cdot 10^{-4}$, and finally $2.757 \cdot 10^{-4}$ A cm^{-2} for Sample 20. Thus, Sample 20 exhibits an apparent j_0 approximately one order of magnitude greater than Sample 16. Because these values originate from Tafel extrapolation, they should be interpreted comparatively, but

their systematic increase is consistent with the pronounced displacement of the polarization curves toward lower overpotential.

The results therefore identify Sample 20 as the best-performing Ni/MXene electrode within the 30 °C series. It exhibits the lowest η_1, η_5, and η_{10}, the lowest Tafel intercept, and the highest apparent exchange current density. Particularly notable is its η_{10} of approximately 210 mV, which is substantially lower than the values obtained for most of the Ni/MXene coatings prepared at higher deposition temperatures.

The contrast between Samples 16 and 20 provides an important illustration of the distinction between Tafel slope and absolute catalytic performance. Sample 16 has the smallest Tafel slope of the series (92.21 mV dec^{-1}), but Sample 20 requires approximately 65 mV less overpotential at 1 mA cm^{-2} and 22 mV less at 10 mA cm^{-2}. Consequently, the smaller slope of Sample 16 should be interpreted as a favorable incremental response to increasing polarization, not as evidence of superior overall HER activity.

Taken together, the 30 °C results indicate that increasing the Ni/MXene electrodeposition current density toward 20–25 mA cm^{-2} strongly improves the absolute HER polarization response, with the most pronounced improvement occurring for Sample 20 deposited at 25 mA cm^{-2}. This behavior differs from the trends observed at 40, 50, and 60 °C and provides evidence that deposition temperature and deposition current density act as coupled processing variables controlling the resulting electrocatalytic properties.

1.5.5 Influence of Electrodeposition Conditions on the HER Performance of Ni/MXene Composite Coatings

The comparison of all Ni/MXene coatings shows that the most favorable HER performance was obtained for samples electrodeposited at the lowest investigated temperature, 30 °C, particularly at the highest deposition current densities. Within

this series, the HER polarization improved progressively from Sample 16 to Sample 20 as the deposition current density increased from 5 to 25 mA cm^{-2}.

The best overall performance was obtained for Sample 20, electrodeposited at 30 °C and 25 mA cm^{-2}. It exhibited the lowest characteristic overpotentials, with η_1 = 74.79 mV, η_5 = 172.22 mV, and η_{10} = 209.52 mV. It also showed the lowest Tafel intercept, 0.0772 V, and the highest apparent exchange current density, $2.757 \cdot 10^{-4}$ A cm^{-2}.

Among the parameters considered, the experimentally determined overpotentials are the most useful indicators of practical HER activity, because they directly describe the polarization required to reach a defined current density. The Tafel slope provides complementary kinetic information but should not be used alone to rank the catalysts. This is illustrated by Sample 16, which exhibited the lowest Tafel slope in the 30 °C series, 92.21 mV dec^{-1}, but substantially higher overpotentials than Sample 20.

Overall, the results indicate that 30 °C is the most favorable electrodeposition temperature investigated, while a deposition current density of 25 mA cm^{-2} produced the best-performing Ni/MXene coating. Thus, the condition 30 °C / 25 mA cm^{-2} can be identified as the optimum among the tested preparation parameters for minimizing HER overpotential in 1 M NaOH.

1.6 Electrochemical evaluation of $Ni_{1-x}Co_xS$ catalysts for HER

The HER performance of $Ni_{1-x}Co_xS$ materials was evaluated in 1 M KOH. The corresponding electrochemical results are presented in Figure 75 and summarized in Table 25.

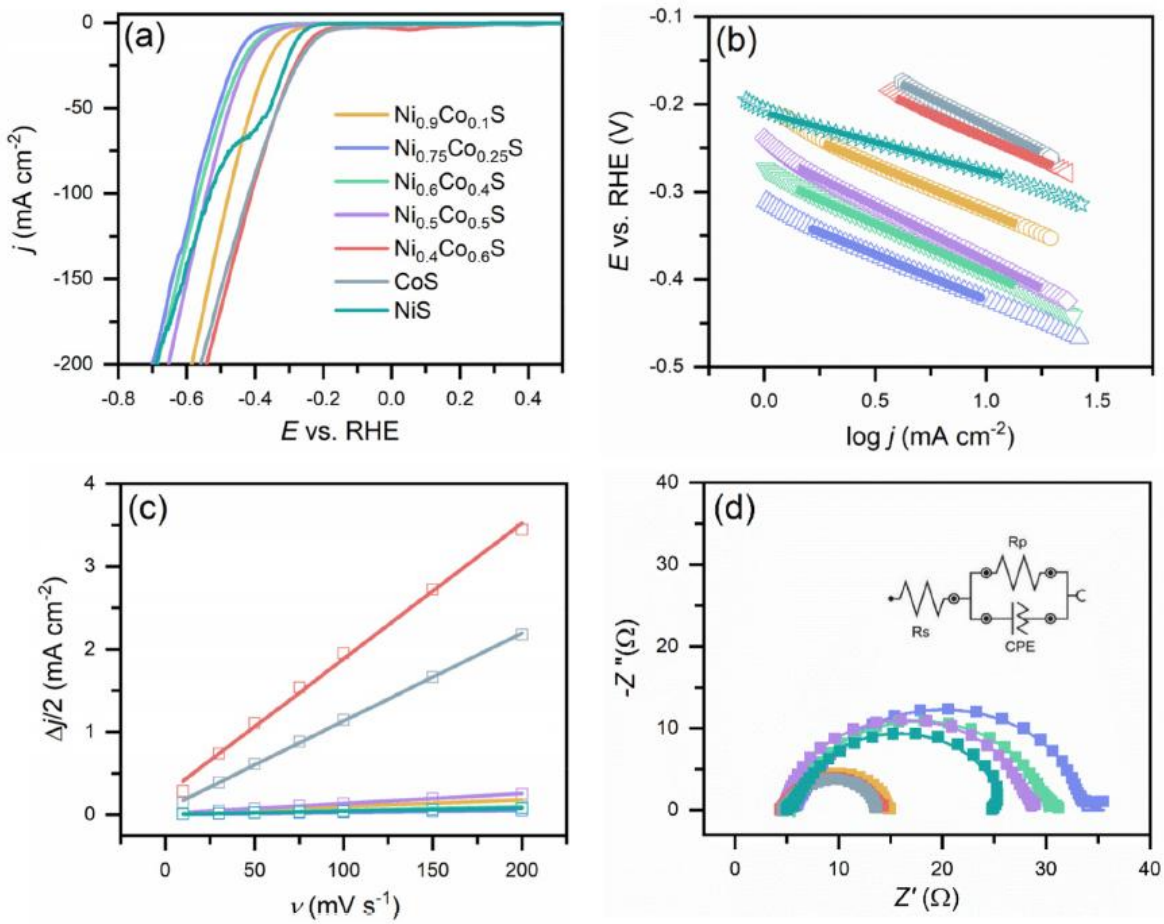


Figure 75. (a) Non-iR-corrected linear sweep voltammetry (LSV) curves of the $Ni_{1-x}Co_xS$, NiS, and CoS and their corresponding, (b) Tafel plots, (c) Linear plots of $\Delta j/2$ as a function of scan rate used for double-layer capacitance (C_{dl}) estimation, and (d) Nyquist plots with inset showing the fitted equivalent circuit. The legend shown in panel (a) applies to all panels.

Table 25. Electrochemical parameters for the hydrogen evolution reaction on $Ni_{1-x}Co_xS$, NiS, and CoS in 1 M KOH.

Sample	LSV				EIS*		CV
	E onset (mV)	-η10 (mV)	b (mV dec^{-1})	j_0 (mA cm^{-2})	R_{ct} (Ω)	N-CPE	C_{dl} (mF cm^{-2})
NiS	174	279	70	$1.1\cdot10^{-3}$	19.5	0.975	0.4
$Ni_{0.9}Co_{0.1}S$	242	320	105	$8.6\cdot10^{-3}$	9.7	0.945	0.8
$Ni_{0.75}Co_{0.25}S$	333	422	103	$7.8\cdot10^{-4}$	27.1	0.939	0.2
$Ni_{0.6}Co_{0.4}S$	231	393	113	$3.4\cdot10^{-3}$	24.2	0.934	0.5
$Ni_{0.5}Co_{0.5}S$	200	377	125	$9.4\cdot10^{-3}$	23.2	0.967	1.2
$Ni_{0.4}Co_{0.6}S$	150	237	108	$6.3\cdot10^{-2}$	9.2	0.886	16.4
CoS	140	222	122	$1.4\cdot10^{-1}$	9.0	0.870	10.6

The LSV curve of NiS exhibits a pronounced “shoulder” at – 380 mV. According to Ding et al., such behavior is commonly associated with irreversible phase transformations of NiS into the more active and stable Ni_3S_2/NiO that occur under cathodic polarization. While this feature provides valuable insight into the pre-catalytic nature of monometallic NiS, it leads to an overestimation of HER performance in the potential region where the transformation occurs. Consequently, the HER kinetic parameters (η_{10}, Tafel slope, and R_{ct}) extracted from LSV of NiS should be considered as apparent values that include both phase transformation and hydrogen evolution. On the other hand, the incorporation of cobalt into the system resulted in a complete disappearance of the observed shoulder on the LSV curves of the NiS. This behavior can be attributed to the formation of mixed Ni–Co sulfide phases and the coexistence of multiple sulfide phases in $Ni_{1-x}Co_xS$. Such systems have been previously reported to be favorable for HER activity.

$Ni_{1-x}Co_xS$ samples exhibit different HER activity in an alkaline medium, with the following trend in η_{10}: $Ni_{0.4}Co_{0.6}S < Ni_{0.9}Co_{0.1}S < Ni_{0.5}Co_{0.5}S \approx Ni_{0.6}Co_{0.4}S \approx Ni_{0.75}Co_{0.25}S$. The observed non-linear trend indicated that the HER activity does not depend monotonically on the nominal composition, but primarily arises from the intrinsic activity of the specific phases formed within the samples. The reliability of these measurements was confirmed by a low relative standard deviation (RSD) of approximately 3.6% for η_{10}.

XRD analysis revealed that $Ni_{1-x}Co_xS$ samples crystallize either as predominantly single-phase samples ($Ni_{0.9}Co_{0.1}S$, $Ni_{0.75}Co_{0.25}S$, $Ni_{0.6}Co_{0.4}S$) or as dual-phase heterostructures ($Ni_{0.5}Co_{0.5}S$, $Ni_{0.4}Co_{0.6}S$). It has been widely reported that nickel sulfide with different stoichiometries and crystal structures exhibit significantly different HER activities. In this context, to evaluate how structural changes in $Ni_{1-x}Co_xS$ affect the intrinsic specific activity of the catalysts, ECSA-normalized polarization curves were analyzed. The curves of the predominantly

single-phase samples revealed subtle differences in specific activity, confirming that the distinct phases constituting these samples indeed exhibit varied intrinsic activities. However, despite these differences, the overall HER performance of single-phase samples remains within a relatively narrow range, suggesting a possible activity limit. A turning point in activity is observed for the dual-phase $Ni_{0.4}Co_{0.6}S$ sample, which exhibited superior HER activity (η_{10} = 237 mV, R_{ct} = 9.2 Ω, and C_{dl} = 16.4 mF cm^{-2}). Interestingly, the ECSA-normalized curve for this sample reveals that its intrinsic specific activity is actually lower than that of the predominantly single-phase samples. This indicates that the superior activity of $Ni_{0.4}Co_{0.6}S$ does not arise from enhanced intrinsic activity of individual site but is more likely the result of significant increase of ECSA and the cooperative interaction between the two phases. This pronounced increase in ECSA (as evidenced by the highest C_{dl} value among $Ni_{1-x}Co_xS$) can be attributed to the synergistic coexistence of two phases, Ni-incorporated Co_9S_8 and CoS phases.

Notably, the significantly higher C_{dl} of $Ni_{0.4}Co_{0.6}S$, despite having a similar morphology to the other samples, suggests that the enhancement in C_{dl} primarily stems from a highly interconnected heterointerface between the phases rather than only geometric roughness. The slightly lower constant phase element exponent (N-CPE) of $Ni_{0.4}Co_{0.6}S$ further supports increased heterogeneity consistent with the formation of the XPS analysis revealed the coexistence of multiple oxidation states of Ni and Co, including Ni^{2+}/Ni^0-like states and Co^{2+}/Co^{3+} species, which facilitates the “electron hopping” mechanism between cations. This improved electronic conductivity is directly corroborated by the lowest R_{ct} observed for $Ni_{0.4}Co_{0.6}S$.

Interestingly, despite a similar dual-phase structure composition, $Ni_{0.4}Co_{0.6}S$ outperforms $Ni_{0.5}Co_{0.5}S$ significantly. Given the significantly lower C_{dl} of $Ni_{0.5}Co_{0.5}S$, coupled with the fact that its ECSA- normalized polarization curve

behaves similarly to the single-phase samples, it is highly likely that a functional, interconnected heterointerface failed to form in this sample.

It should be emphasized that although different cobalt precursor particle sizes were employed for samples with higher cobalt content to enable MSR ignition, electrochemical measurements unambiguously confirm that the precursor particle size does not significantly affect the final HER performance. Therefore, the enhanced activity of $Ni_{0.4}Co_{0.6}S$ can be attributed to compositional and structural effects rather than to differences in synthesis parameters.

While the catalytic performance of $Ni_{0.4}Co_{0.6}S$ is comparable to that of the CoS reference sample, its synthesis is faster and more cost-effective. $Ni_{0.4}Co_{0.6}S$ was synthesized in just 30 s using a cheaper stainless steel chamber in a mixer mill, as opposed to the CoS reference sample, which required 10 min of planetary milling in an expensive tungsten carbide chamber. Moreover, the Tafel analysis revealed that all $Ni_{1-x}Co_xS$ catalysts exhibit a Tafel slope (b) close to 107 mV dec^{-1}, which is slightly lower than that of CoS (122 mV dec^{-1}). These values suggest that the Volmer reaction, which involves splitting a H_2O molecule into a hydroxyl ion (OH^-) and an adsorbed hydrogen atom (H_{ads}) on the catalyst surface, is the rate-determining step. The slightly reduced Tafel slopes observed for $Ni_{1-x}Co_xS$ indicate more favorable water dissociation kinetics, further supporting the beneficial role of the Ni–Co synergy. Moreover, according to the EU's 2023 Critical Raw Materials study, nickel, unlike cobalt, is classified as part of the Strategic but not Critical Raw Material due to its lower supply risk. Thus, the partial substitution of cobalt with nickel in $Ni_{0.4}Co_{0.6}S$ makes the catalyst more sustainable, cheaper, and easier to supply on a large scale than pure CoS.

Recent literature highlights that heterostructured catalysts can mitigate the limitation of the Sabatier principle by spatially decoupling water dissociation and hydrogen desorption. In our dual-phase catalysts ($Ni_{0.4}Co_{0.6}S$ and CoS), this is most

likely achieved by forming heterointerfaces between distinct sulfide phases. Rather than making speculative atomic-level assignments, we rely on both our experimental evidence and fundamental physics of semiconductor heterojunctions, which dictates that the contact between two distinct phases creates a relative work function difference (ΔΦ). This difference in ΔΦ spontaneously drives interfacial electron transfer, establishing a strong built-in electric field. Consequently, this charge redistribution creates rationally distinct, highly polarized active sites: one serving as the optimal water dissociation center and the adjacent one acting as the optimal hydrogen desorption center, thereby establishing a highly efficient cooperative dual-site mechanism.

1.7 Comparative HER Performance of Bare and Modified Ni Foam Electrodes with Ni and Ni/MoS_2 Coatings

To evaluate the effect of surface modification on the hydrogen evolution reaction (HER), the electrochemical behavior of bare Ni foam was compared with Ni-coated and Ni/MoS_2-coated Ni foam electrodes. All measurements were performed in 1 M NaOH at 25 °C using a scan rate of 2 mV s^{-1}. A saturated Ag/AgCl electrode was used as the reference electrode, potentials were converted to the reversible hydrogen electrode (RHE) scale, and current densities were normalized to the geometric electrode area of 4 cm^2, consistent with the electrochemical methodology used throughout this work. Automatic iR compensation was applied during the measurements.

The consecutive LSV measurements show that the polarization response of the Ni-foam-based electrodes changes during the initial cycles before becoming more stable. This behavior is consistent with electrochemical conditioning of the electrode surface during repeated cathodic polarization. Similar changes observed for the Ni coatings investigated in the preceding sections were associated with possible

changes in surface oxide/hydroxide species, removal of weakly adsorbed species, improved wetting, and progressive stabilization of the electrode/electrolyte interface; however, the LSV measurements alone cannot establish the specific origin of these changes.

The LSV curves of the bare Ni foam provide the reference response against which the effect of the deposited coatings can be assessed. The report includes consecutive polarization curves for bare Ni foam and for Ni-coated Ni foam prepared under different electrodeposition conditions. For direct comparison of HER activity after electrochemical conditioning, Cycle 7 was selected for the combined polarization comparison of bare Ni foam, Ni-coated Ni foam, and Ni/MoS_2-coated Ni foam.

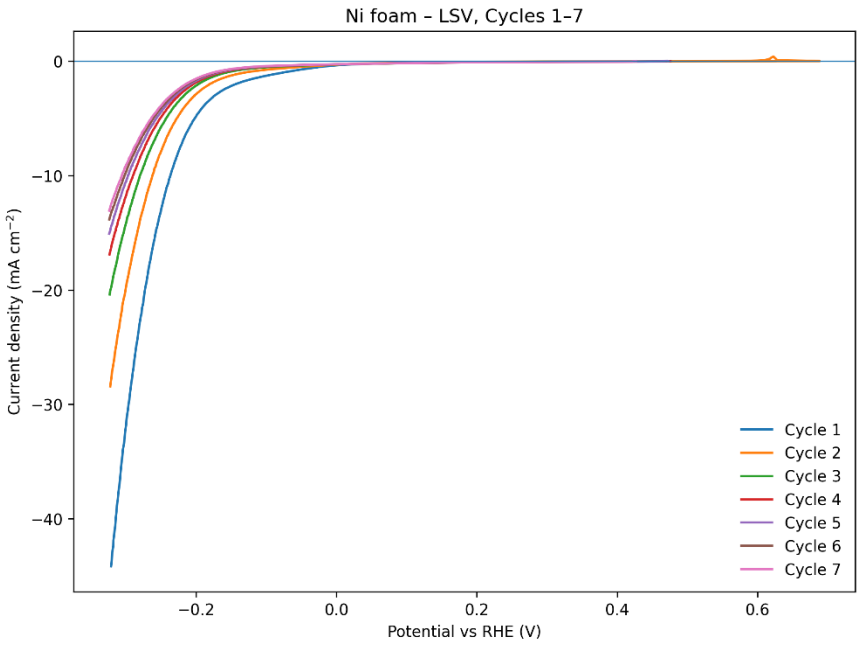


Figure 76. Linear sweep voltammograms of Ni foam electrode recorded during eight consecutive cycles in 1 M NaOH at 25 °C with a scan rate of 2 mV s^{-1}. Potentials are reported versus the reversible hydrogen electrode (RHE), and current densities are normalized to the geometric electrode area of 4 cm^2.

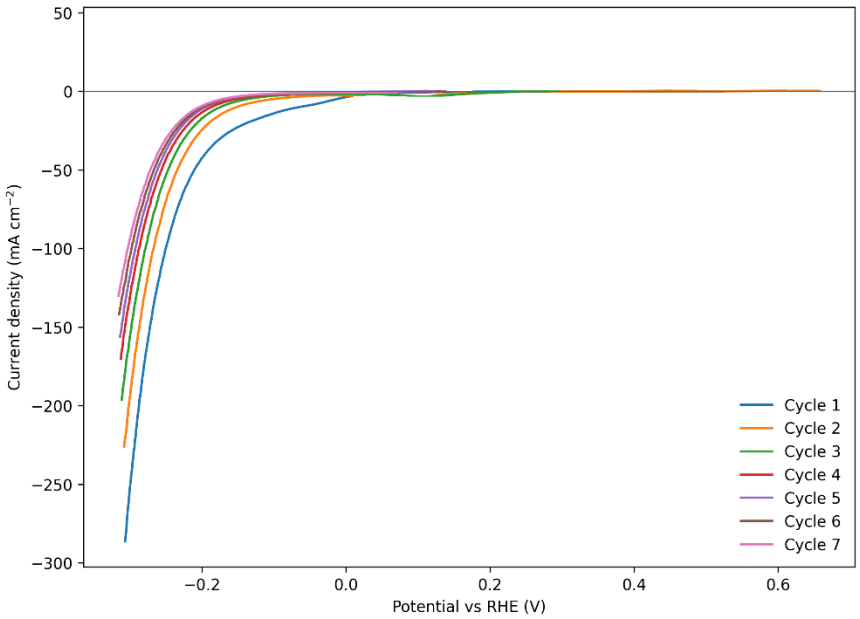


Figure 77. Linear sweep voltammograms of a Ni-coated Ni foam electrode (*electrodeposition conditions: t = 40 ºC; E = -0.75 V*) recorded during eight consecutive cycles in 1 M NaOH at 25 °C with a scan rate of 2 mV s^{-1}. Potentials are reported versus the reversible hydrogen electrode (RHE), and current densities are normalized to the geometric electrode area of 4 cm^2.

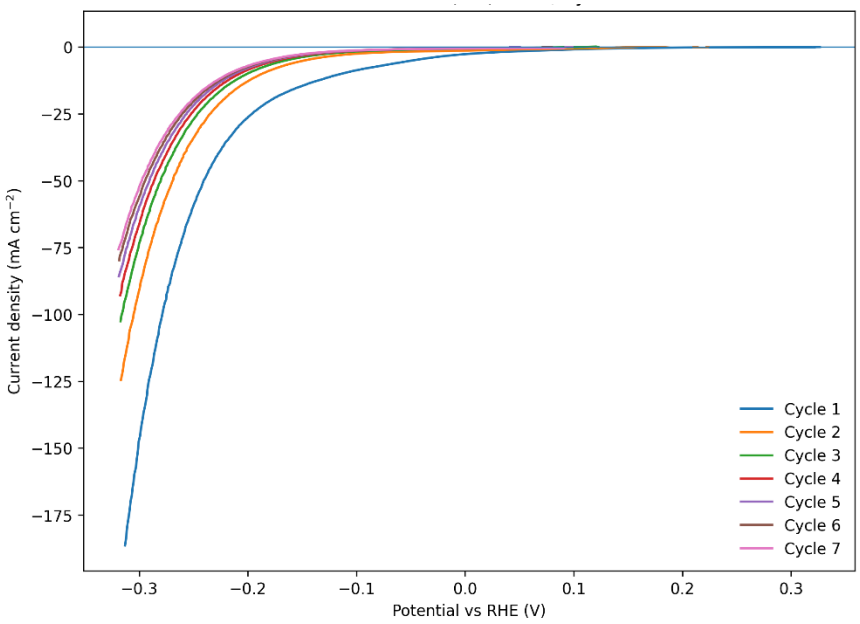


Figure 78. Linear sweep voltammograms of a Ni-coated Ni foam electrode (*electrodeposition conditions: t = 40 ºC; E = -1.00 V*) recorded during eight consecutive cycles in 1 M NaOH at 25 °C with a scan rate of 2 mV s^{-1}. Potentials

are reported versus the reversible hydrogen electrode (RHE), and current densities are normalized to the geometric electrode area of 4 cm².

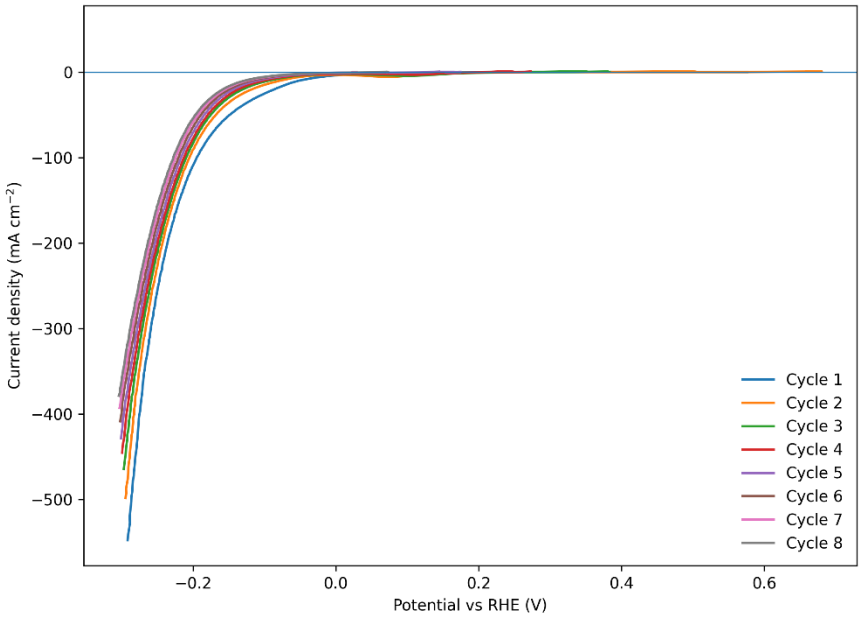


Figure 79. Linear sweep voltammograms of a Ni/MoS_2-coated Ni foam electrode (*electrodeposition conditions: t = 40 ºC; E = -0.75 V*) recorded during eight consecutive cycles in 1 M NaOH at 25 °C with a scan rate of 2 mV s^{-1}. Potentials are reported versus the reversible hydrogen electrode (RHE), and current densities are normalized to the geometric electrode area of 4 cm².

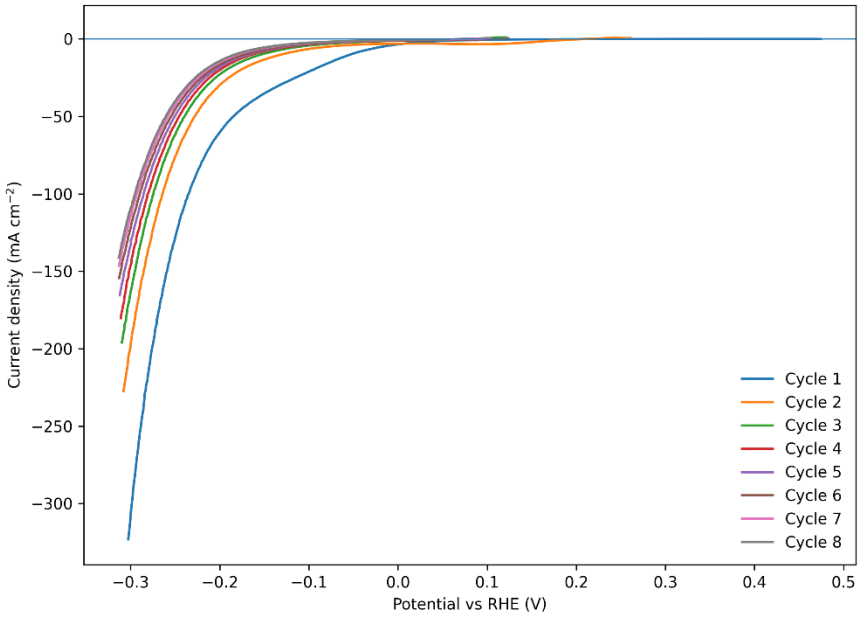


Figure 80. Linear sweep voltammograms of a Ni/MoS_2-coated Ni foam electrode (*electrodeposition conditions: t = 40 ºC; E = -1.00 V*) recorded during eight

consecutive cycles in 1 M NaOH at 25 °C with a scan rate of 2 mV s^{-1}. Potentials are reported versus the reversible hydrogen electrode (RHE), and current densities are normalized to the geometric electrode area of 4 cm^2.

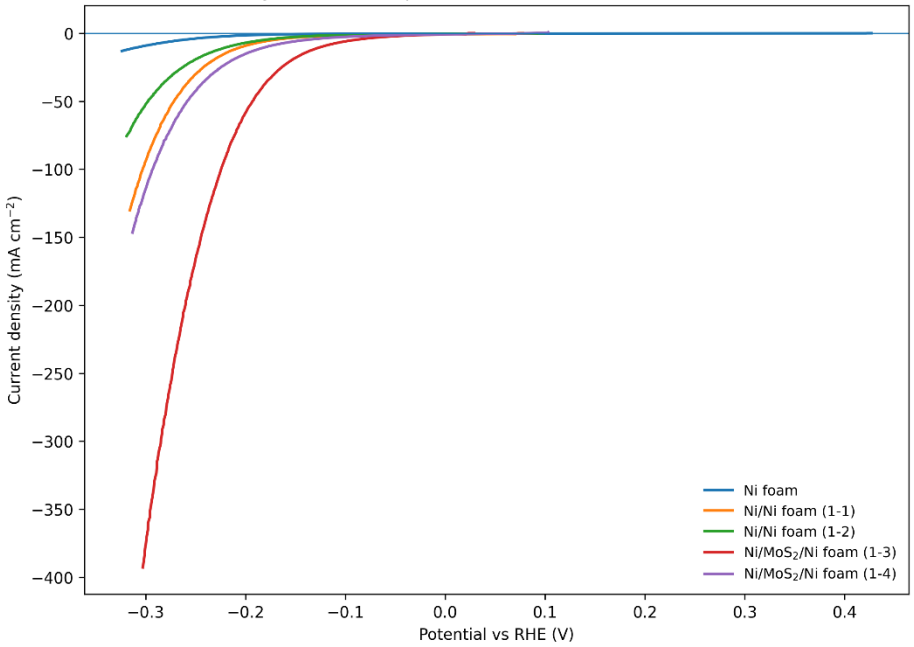


Figure 81. Comparison of Cycle 7 linear sweep voltammograms of bare Ni foam, Ni-coated Ni foam, and Ni/MoS_2-coated Ni foam electrodes recorded in 1 M NaOH at 25 °C with a scan rate of 2 mV s^{-1}. Potentials are reported versus the reversible hydrogen electrode (RHE), and current densities are normalized to the geometric electrode area of 4 cm^2. A saturated Ag/AgCl electrode was used as the reference electrode in all experiments. (*Electrodeposition conditions:(1_1) and (1_3) - t = 40 °C; E = -0.75 V; (1_2) and (1_4) - t = 40 °C; E = -1.00 V*).

Figure 81 compares the Cycle 7 polarization curves of the investigated electrodes. The results demonstrate that modification of the Ni foam surface strongly affects its HER response. Both Ni coating and incorporation of MoS_2 produce substantially higher cathodic current densities than the bare Ni foam over the investigated potential range. The improvement is particularly pronounced for the Ni/MoS_2-coated Ni foam, indicating that the combination of the highly porous and conductive Ni-foam substrate with the Ni/MoS_2 catalytic layer provides the most favorable overall polarization response among the tested Ni-foam-based electrodes.

The two Ni-coated Ni foam electrodes also exhibit enhanced HER activity relative to bare Ni foam, demonstrating that electrodeposition of an additional Ni layer can improve the electrochemically accessible surface and/or catalytic properties of the substrate. The difference between the two Ni-coated electrodes further indicates that the electrochemical performance depends on the conditions used for coating deposition. Therefore, the catalytic response cannot be attributed solely to the Ni-foam substrate but is strongly influenced by the properties of the deposited surface layer.

A further improvement is observed following incorporation of MoS_2 into the Ni coating. The Ni/MoS_2-modified electrodes show the largest cathodic currents in the comparative LSV measurements, with the Ni/MoS_2/Ni foam (1-3) electrode exhibiting the strongest HER polarization response among the investigated samples. This observation is consistent with the broader Ni/MoS_2 results in this report, which demonstrate that the HER performance of the composite coatings depends significantly on their preparation conditions.

Overall, the Cycle 7 comparison establishes the qualitative activity sequence

Ni/MoS_2/Ni foam > Ni/Ni foam > bare Ni foam

under the investigated conditions. Thus, surface modification of Ni foam with an electrodeposited Ni layer improves its HER polarization behavior, while incorporation of MoS_2 into the Ni coating provides the largest enhancement. The results demonstrate the potential of Ni foam as a three-dimensional conductive support for Ni-based composite HER catalysts and identify Ni/MoS_2-modified Ni foam as the most promising configuration among the Ni-foam-based electrodes investigated in this series.